PHASED ARRAY WEATHER RADAR

Weather Targets Doppler Processing in Phased Array Radar with Fast Azimuthal Scanning

Alexandru Gîrdianu

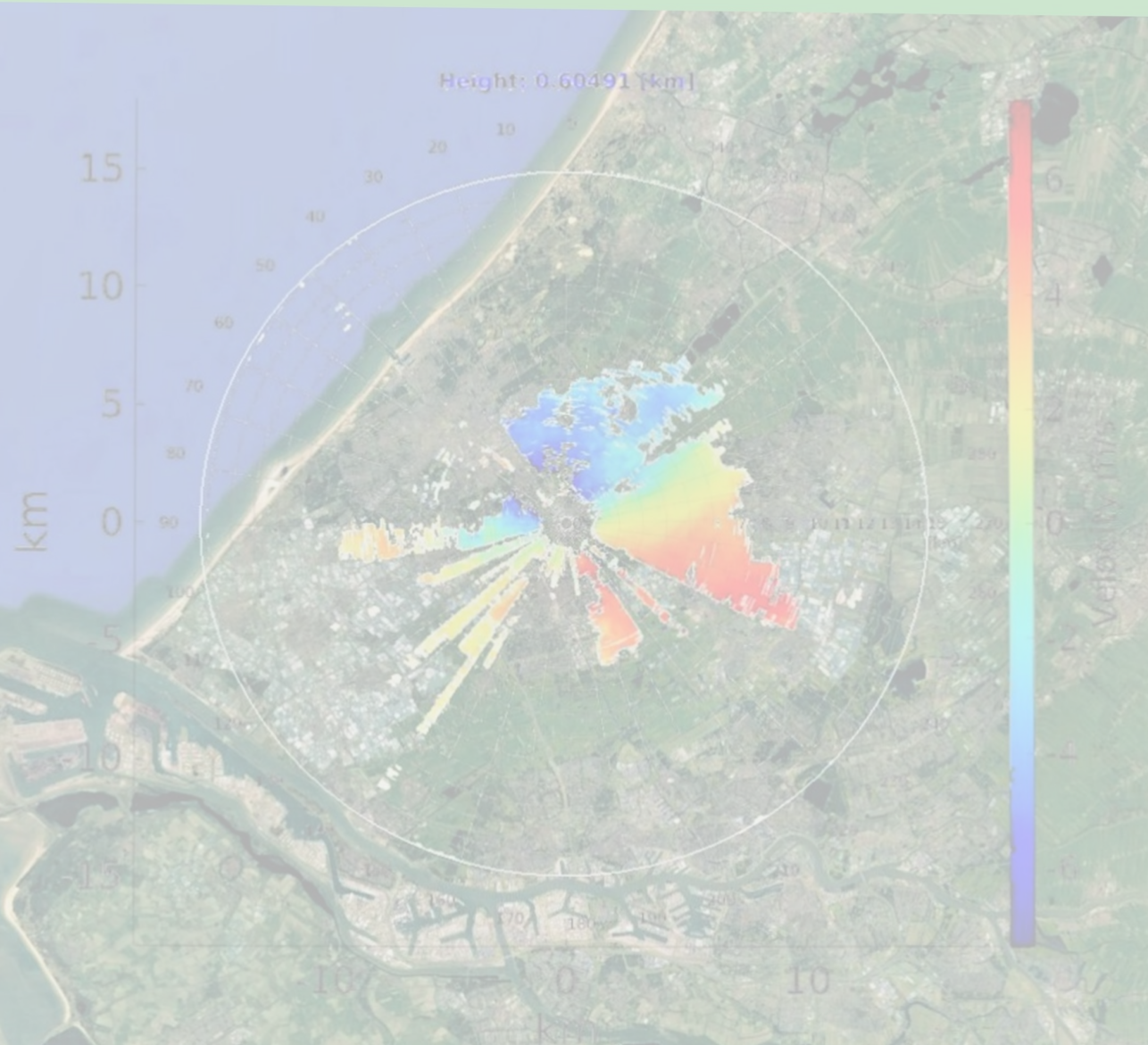

PHASED ARRAY WEATHER RADAR

Weather Targets Doppler Processing in Phased Array Radar with Fast Azimuthal Scanning

by

Alexandru GÎRDIANU

to obtain the degree of Master of Science
at Delft University of Technology,

Student number	5143780	
Project duration	November, 2020 - July, 2021	
Thesis committee	Professor DSc. Alexander Yarovoy	TU Delft, Chair MS3
	Assistant Professor Dr. Oleg A. Krasnov	TU Delft, MS3, supervisor
	Associate Professor Dr. ir. Richard Hendriks	TU Delft, CAS

TU Delft

PREFACE

"Insofar as the propositions of mathematics give an account of reality they are not certain; and insofar they are not certain they do not describe reality." - Albert Einstein

I would like to offer my special thanks to the people that helped me through this entire process of the thesis.

Firstly, I would like to express my very great appreciation to Dr. Oleg Krasnov, my main supervisor, for his valuable and constructive suggestions during the planning and development of this research work. His willingness and patience to help me understand atmospheric physics and weather radar had been very much appreciated.

I am particularly grateful for the assistance given by Ph.D. ir. Tworit Dash, my second supervisor, for his support provided anytime when I was in difficulty and for his enthusiastic encouragement.

I would like to express my deep gratitude to Prof. Alexander Yarovoy, the chair of the MS3 department, for his constant help and useful remarks that helped me every time to get a broader understanding of the problems that this thesis project involved. Also, the support he provided to get through this difficult pandemic period has been very much appreciated.

I would like to thank Robin Radar company for their assistance with the collection of my data. My special thanks are extended to Rob van der Meer and Dennis Hoveling, members of staff of Robin Radar company, for their willingness to give their time so generously. Thank you Rob van der Meer for giving me the chance to see MAX3D radar and for the exciting explanations you gave to me about hardware design. Thank you Dennis Hoveling for giving me the chance to see MAX3D radar working and processing real data and for all the interesting explanations you gave to me about software design.

I would like to thank SkyEcho company for their active participation at the progress meetings and the useful critiques of this research work. My special thanks are extended to Dr. Yann Dufournet that provided me a very concise and useful explanation of the estimation of the true velocity of the wind using radars.

I wish to thank various members of MS3 that offered their support all the time when was needed; Dr. Yanki Aslan for helping me to clarify my problems about beamforming, Ms. Esther de Klark, Mr. Fred van der Zwan for their willingness and enthusiasm to solve my administrative issues, ir. Max Schöpe, Ph.D. ir. Ignacio Roldan Montero, Ph.D. Nicolas Kruse thank you all for the constructive discussion we had and the help you offered to me, and ing. A.P. Frehe for helping with the servers at MS3.

I wish to thank all my friends in MS3, MSc. student Ruman Kazi, MSc. Simin Zhu, MSc. student Anusha Ravish Suvarna, MSc. student Marta Buenaventura Camps, MSc. student Karan Jayachandra

I wish to thank various professors from TUDelft for their courses and willingness to teach me the curriculum included in the profile that I have been chosen.

Special thanks should be given to Prof. Stefan-Adrian Toma, of Military Technical Academy, for the determination to follow signal processing and radar systems profile.

I thank my friends that helped me to choose this university and helped with the process to get through Bogdan Bîrgovan, Ana-Maria Taradaciuc, Paula Coșlugeanu, and Ruben Munteanu.

Thank you to my girlfriend Daniela Tole, for all her love and support, for listening and motivated to me all the time when has been needed.

I would like to acknowledge the support provided by my parents, my mother Floreza Gîrdianu, and my father Mihai Gîrdianu, without who I wouldn't have been here. I thank them for their sacrifice and comprehension and words that have been made me stronger. As a student of science, I believe, I am here because of the combined effort of my family during my education period.

Alexandru Gîrdianu
Delft, June 2021

CONTENTS

LIST OF FIGURES

LIST OF TABLES

1

INTRODUCTION

1.1. BACKGROUND

PHASED array radars that are used at the airport for bird and drone detection are not usually used for Doppler processing of signals received from weather targets. However, the signal processing of these radar systems can be upgraded to accommodate Doppler processing for weather applications. This upgrade can help us determine the wind velocity and direction as well as the turbulence intensity fields. This information can help airport management to reduce the risk of crashing events of airplanes. The radar under test for this thesis project is MAX3D radar from Robin Radar in the Netherlands [1]. With the introduction of Europees Fonds voor Regionale Ontwikkeling (EFRO) project, new ways and means are explored to make use of this radar for extended weather target detection as the original purpose was to detect point targets. Due to its original purpose, this radar works at a very high rotation speed, 60$[RPM]$, for a high refresh rate, the reason why target tracking is performed using range migration [2], instead of Doppler processing. Hence, this project concerns the development of a signal processing toolbox meant to treat each step of the processing chain necessary to provide high accuracy estimation of precipitation profiles and reconstruction of the three-dimensional (3D) Doppler map. For this, radar data is recorded at the rotation speed of 1 [RPM], which means about 285 sweeps per resolution cell. However, the final goal is to find technical solutions to compensate for radar's fast rotation and to apply this toolbox for data with many limited sweeps per resolution cell, e.g. around five. This master project is a part of the EFRO project which is running under the research partnership between TU Delft, Robin Radar, and SkyEcho.

1.2. PROBLEM STATEMENT

Detection of the presence and location of precipitation, the wind speed, and direction vertical profiles, and turbulence intensity estimation, are the important sensing tasks for radar in an airport area. In such a dynamic area as an airfield, a multifunction radar has to have a high update rate and, as a result, fast scan rate and rotation velocity.

For radars with high antenna gain, it results in a very short time on target. As result, coherent Doppler processing can include only short bursts with a few only pulses/sweeps. Finally, the classic Doppler processing can be done but only with very coarse resolution and quite low processing gain. Such low performances of the Doppler processing strongly influence detectability and parameters estimation of atmospheric targets as quite weak radar targets. This is the main reason why Doppler weather channels in Air Traffic Control (ATC) radars are not implemented at all or have quite low operational performances. Within the EFRO project, we would like to study possible approaches to overcome this limitation.

1.3. RESEARCH OBJECTIVES

The preliminary goal of EFRO project, taken over in this thesis, is to understand to what degree the available signal processing tools can help to upgrade MAX3D radar with a second processing channel for wind field estimation, without jeopardizing performances of its main mission, birds and drones tracking. Note that for this purpose radar rotates at 60 [RPM], which on one hand means a high refresh rate for birds tracking, 1 [s], but on the other hand means very low-velocity resolution, $\Delta v = 3.69[m/s]$.

Hence, the first problem to cope with is the trade-off between refresh rate and velocity resolution. Before tackle this, a preliminary problem is posed. Performance study of MAX3D radar for detection of weather (extended) targets. Based on this a list of research objectives is considered for this thesis:

1. *Reading and processing big data file from MAX3D radar.*
   This research is conducted using real radar data recorded with MAX3D radar. In normal scanning mode, this radar rotates with 60 [RPM], however, for analysis of performances in the Doppler domain, data used in this project was recorded at 1 [RPM], which implies a data file of 120 GB. This problem has been solved within *Extra Project* carried out in period *July 2020 - September 2020* under the supervision of Assistant Professor Dr. Oleg A. Krasnov.

2. *Understanding the limitation imposed by the presence of artifacts due to the receiver saturation.*
   The available system is installed on the top of a building located in an industrial area. Because of the big objects close to the radar (up to 10 [m]), high reflected power result in receiver saturation. Because MAX3D is an *Frequency-modulated Continuous-wave* (FMCW) radar system, *phase noise* effect occurs. This effect creates undesired harmonics spread all over the spectra. As consequences noise level increase very much, around 20 dB Signal to Noise Ratio (SNR) loss.

3. *Beamforming algorithm dedicated for high estimation accuracy of precipitation profiles.*
   Beamforming algorithm employed for weather applications has to fulfill a set of requirements such as 1) sidelobes level suppression, 2) accurate estimation of true amplitude and phase information and, 3) robustness to a limited number of Doppler bins, [3] and [4].

4. *Target mask for estimation accuracy gain of precipitation profiles.*
   Assuming particles in the cloud follow wind velocity, after Doppler processing, particle velocities are spread in a Doppler spectrum distribution. Thereby an accurate estimation of precipitation profiles implies noise clipping and clutter suppression present in the Doppler field, [5]. Note that this project does not treat the estimation problem of true wind velocity, but only of the estimation of precipitation profiles using radial Doppler velocity.

5. *Velocity aliasing correction algorithm.*
   Velocity aliasing happens when wind velocity is greater than maximum unambiguous velocity and as an effect Doppler spectrum distribution of the atmospheric particles is folded. This means discontinuities in the measured Doppler field, [6] that imply strong degradation of estimation of spectral width and mean Doppler velocity.

6. *Reconstruction of 3D Doppler map.*
   Representation of precipitation profiles for 3D coordinates is necessary to determine radar's performances for weather applications, and the correctness of the developed signal processing toolbox.

7. *Formulation of a solution for compensation of radar's fast rotation.*
   When radar rotates, there is available only a limited number of pulses within each resolution cell, hence the fewer sweeps are available, the less is velocity resolution. However, if we consider the case of homogeneous precipitation field, and assume that in the area surveyed by radar, wind direction and velocity does not produce much change in the horizontal field, then the radial velocity between successive azimuth direction can be assumed to follow a cosine rule only, that, theoretically, can be compensated.

1.4. LITERATURE REVIEW

Phased array radar used for weather detection becomes more and more popular due to the presented advantages of high spatial and temporal resolution. This increases performances for the detection of fast-forming weather phenomena, which requires early detection and warning. The main topics discussed in the literature, regarding weather radar systems, are beamforming techniques, ground clutter suppression, and filtering of non-weather targets. Thus, the results after the literature review are as follows.

1.4.1. BEAMFORMING METHOD

Besides conventional Fourier (FR) beamforming (BF) method, known for high accuracy estimation of power reflectivity and phase information, but low efficiency of sidelobes suppression, and Capon (CP) method, known to be highly efficient for sidelobes suppression but present low performances in terms of amplitude and phase estimation, there are other adaptive BF methods that have high performances for both these characteristics, like one proposed in [4], called *reiterative Minimum Mean Square Error* (rMMSE). This method was proposed in 2011 for point targets,[7], and reconsidered in 2013 for weather targets, when an upgrade for power constraint was included, [4]. Later

on, more advanced BF techniques were proposed, *nonlinear* BF method and *neural-network-based* BF method, [8] and [9], respectively.
Since the objectives of this thesis are spread over multiple subjects, the goal is not to propose a new BF method, but to test the performances of an already existing method for MAX3D radar data type. Since the conventional methods, FR and CP, do not fulfill all the requirements stated above, our choice for the BF method is the rMMSE method, [4].

1.4.2. TARGET MASK FOR ESTIMATION ACCURACY GAIN OF PRECIPITATION PROFILES

Target Mask term here represents a (two-dimensional) 2D binary image, where pixels of one represent alternative hypothesis, the target is present and pixels of zero, null hypothesis, the target is absent. For the creation of a target mask, a detection algorithm is required. Two of the algorithms, found in the literature, for clutter suppression, [10] and adaptive filtering noise, [11] use morphological methods for weather image processing. The former is mainly based on the Gray-level Co-occurrence Matrix (GLCM) feature, and the latter on pixels density. For both papers, the structural element (SE) involved in the morphological operation has a fixed dimension. However, in other papers, not related to radar weather, SE dimension is incremented until some criteria are reached, [12]. In this paper, but also in others, [13], optimal algorithms are developed using the morphological method.
Thereby, in this thesis, we propose adaptive morphological filtering (AMF) algorithm, that uses pixels density to determine the dimension of SE that provides the highest estimation accuracy of precipitation profiles and a priori range profiles of noise power, estimated using noise data recorded with MAX3D radar.

1.5. RESEARCH LIMITATIONS

This project's main objective is to obtain precipitation profiles with high estimation accuracy. For this, here are treated problems like suppression of the sidelobes of ground clutter, suppression of non-weather targets, and noise filtering. However, suppression of ground clutter is not included in our objectives. Moreover, based on the analysis of final results, a strong presence of ground clutter, that cannot be suppressed by the AMF algorithm are present up to four [km] range only and this range becomes lower for higher elevation angles. Secondly, the computational time is another constrain which we do not take into account in this project.

1.6. CONTRIBUTIONS AND NOVELTY IN THIS PROJECT

To fulfill the research objective of this project, there are some contributions and novelty included in the following list:

- Testing the performances for chosen BF method,rMMSE using real data recorded with MAX3D radar.
- Conducting the whole process from raw data to the reconstruction of 3D map, for high estimation accuracy of precipitation profiles, using a phased array radar designed for point targets detection.

- A novel approach for target mask creation that combines range profiles of noise power and morphological methods to obtain an adaptive filtering algorithm of noise and non-weather targets.

- Development of an iterative algorithm for Doppler aliasing correction, that minimizes the error of the absolute value of the difference between the index of mean Doppler velocity and index of the center of the spectra, this is 0 [m/s].

1.7. THESIS ROADMAP

Chapter 2 introduces MAX3D radar characteristics. It covers radar system parameters where analysis of radar parameters is carried out from the perspective of weather target detection requirements. The analysis carries on for real data, where the problem of artifacts is discussed from the point of view of limitation imposed by the saturation effect. Moreover, a noise data analysis is performed, where noise data is obtained when the radar transmitter is switched off.
Chapter 3 introduces *Weather Radar Signal Simulator*, used for simulation of weather spectra and time series signals used for performances study of beamforming and AMF.
Chapter 4 includes the general mathematical formulation of the beamforming method and shows the results for simulated and real data. In this chapter we test an algorithm proposed in [4].
Chapter 5 shows the performance of the AMF algorithm in terms of estimation error and estimation accuracy of precipitation profiles for simulated and real data. Moreover, this chapter includes read data simulation results for *Doppler Aliasing correction* (DAc) algorithm.
Chapter 6 presents our approach for the transformation of Doppler moment values from polar to Cartesian. A comparison over five different interpolations is carried on to find the one that gives the best threshold between interpolation error, visual inspection, and computational time. Results for constant height Plan Position Indicator (PPI) and constant azimuth Range Height Indicator (RHI) of precipitation profiles are included for real weather data.
Finally, conclusions and recommendations are drawn in **Chapter 7**.

REFERENCES

[1] *Robin Radar Systems full 3D Advanced Bird Detection Radar - MAX3D,* https://www.robinradar.com/max-avian-radar-system, accessed: 2021-06-22.

[2] J. M. Lopez-Sanchez and J. Fortuny-Guasch, *3-d radar imaging using range migration techniques,* IEEE Transactions on antennas and propagation **48**, 728 (2000).

[3] F. Mizutani, M. Wada, H. Marui, and H. Handa, *Development of Active Phased Array Weather Radar,* , 2 (2012).

[4] E. Yoshikawa, T. Ushio, Z. Kawasaki, S. Yoshida, T. Morimoto, F. Mizutani, and M. Wada, *Mmse beam forming on fast-scanning phased array weather radar,* IEEE Transactions on Geoscience and Remote Sensing **51**, 3077 (2013).

[5] R. J. Doviak and D. S. Zrnić, *Doppler Radar and Weather Observations*, second edition ed. (Elsevier Inc., 1993) pp. ch.7.10.1, page 200.

[6] R. J. Doviak and D. S. Zrnić, *Doppler Radar and Weather Observations*, second edition ed. (Elsevier Inc., 1993) pp. ch.7.4.5, page 17.

[7] S. D. Blunt and S. Member, *Robust DOA Estimation : The Reiterative Superresolution (RISR) Algorithm,* IEEE Transactions on Aerospace and Electronic Systems **47**, 332 (2011).

[8] D. Kitahara, H. Kuroda, and A. Hirabayashi, *Nonlinear Beamforming Based on Group-Sparsities of Periodograms for Phased Array Weather Radar,* **XX**, 1 (2021).

[9] T. Sallam, A. B. Abdel-rahman, M. Alghoniemy, and S. Member, *A Neural-Network-Based Beamformer for Phased Array Weather Radar,* **54**, 5095 (2016).

[10] P. Wang, Kao-Jixu, Y. Zhang, and H.-Z. Jia, *Doppler weather radar clutter suppression based on texture feature,* in *2012 International Conference on Machine Learning and Cybernetics*, Vol. 4 (2012) pp. 1339–1344.

[11] S. S. Aung, I. Nagayama, and S. Tamaki, *An adaptive morphological operation for high-performance weather image processing,* IEIE Transactions on Smart Processing and Computing **7**, 424 (2018).

[12] C. Debes, J. Riedler, M. G. Amin, and A. M. Zoubir, *Iterative target detection approach for through-the-wall radar imaging, 2009 IEEE International Conference on Acoustics, Speech and Signal Processing,* , 3061 (2009).

[13] R. Firoz, S. Ali, M. N. U. Khan, and K. Hossain, *Medical image enhancement using morphological transformation,* Journal of Data Analysis and Information Processing **4**, 1 (2016).

2

MAX3D RADAR CHARACTERISTICS

A preliminary analysis of the systems parameters, real data, and noise data concerning the minimum requirements for a radar weather system is the main topic discussed in this chapter. Hence, the advantages and disadvantages of this system parameters are discussed concerning the ones required for weather target detection. The system of antennas is described and the related antenna pattern footprint is shown at different elevation angles. Next, real-time data simulation results are introduced, for both weather real-time data and noise data. For real-time data are shown two constant elevation Plan Position Indicator (PPI) plots. The first one is close to the ground, $\theta = 2.5°$, and the second one is shown for the maximum elevation angle in the scanning range, $\theta = 30°$. Power artifacts due to the receiver saturation are introduced and shown and explained together with its side effects. Moreover, two-dimensional (2D) and one-dimensional (1D) plots of data after beamforming processing, are shown for a comprehensive overview of the receiver's saturation effect. For noise data, estimation of range profiles of noise power shows the noise-range dependency, due to the amplitude gain control attenuation of the amplifier located before Analog to Digital Converter (ADC). A comparison performed between profiles of noise power and real data ranges profiles shows that noise power profile is a good candidate for the estimation of noise floor for real data range profiles. However, this approach does not work when saturation of the receiver occurs.

2.1. MAX3D RADAR PARAMETERS

MAX3D radar developed and produced by Robin Radar company, has been developed for the purpose of bird detection with regard to flight safety and bird collision avoidance. MAX is a rotating search radar with a phased array receive and transmit antenna, that works with horizontal polarization. MAX is an FMCW radar that in normal scanning mode rotates with 60 [RPM] while on elevation is electronically scanning in interval range of $[0°, 60°]$. Radar used for data acquisition is installed on the top of a building located in Den Haag, The Netherlands. Figure 2.1 shows radar surveying area represented by a white color circle.

Figure 2.1: MAX3D radar scanning area for the radar that provides data for this research.

2.1.1. ANTENNA PARAMETERS

Systems of antennas for MAX3D radar present two antennas for receiving, RX_1 and RX_2 and one for transmission, *TX*. Figure 2.2 shows a sketch of MAX outside design and the location of these antennas. First receive antenna, RX_1, called *Main-Array*, has 40 slotted waveguides lines, with a tilt angle of 15° and an electronic scanning interval $[0.5°, 30°]$, on elevation. RX_2 is called *Blindspot Array* and has 8 elements, with a tilt angle of 45° and elevation interval $[30°, 60°]$. *TX* array forms a cosecant square pattern. Radar parameters are shown in Table 2.1.

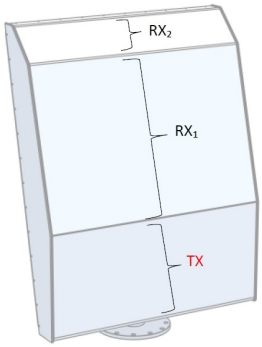

Figure 2.2: MAX3D radar configuration

Note that ratio between elements distance and lambda, $\frac{d}{\lambda} = 0.66 > 0.5$ which means

Parameter	Value	Obs.
Range resolution (Δr)	2.27 m	-
Azimuth resolution ($\Delta\phi$)	1.8 deg	-
RX1 elevation resolution ($\Delta\theta_1$)	1.97 deg	for 0.5 deg
RX2 elevation resolution ($\Delta\theta_2$)	9.85 deg	for 30 deg
Instrumented range	15 km	-
Hits per scan	5	for 60 RPM
Maximum unambiguous velocity	7.39 m/s	-
Number of beams for RX_1	15 beams	-
Number of beams for RX_2	4 beams	-

Table 2.1: MAX 3D radar parameters

that maximum steering angle to prevent grating lobes is

$$\theta_{max} = \frac{1}{sin(\lambda/d - 1)} = 33.64^{\circ} \tag{2.1}$$

The reason for 15 beams for RX_1 is that this is the minimum number of beams which respects the elevation resolution of $\approx 2^{\circ}$.

2.1.2. ADVANTAGES AND DISADVANTAGES FOR WEATHER APPLICATIONS

The parameters of interest for weather applications are:

- Space resolutions;
  - elevation resolution ($\Delta\theta^{\circ}$);
  - azimuth resolution ($\Delta\phi^{\circ}$);
  - range resolution ($\Delta r[m]$).
- Time resolution ($\Delta T[s] = M \cdot PRT$) , where M is the total number of sweeps and PRT is *Pulse repetition interval*. PRT for MAX3D is $PRT \approx 1[ms]$;
- Velocity resolution ($\Delta v[m/s]$);
- Maximum unambiguous Doppler velocity ($v_{max}[m/s]$).

MAX3D radar advantages with respect to weather application requirements are included in the next list.

1. High range resolution Δr = 2.27 [m]. For weather radar purposes, MAX3D has a very high range resolution, compared with those already existing in The Netherlands, like Parsax, IDRA, TARA, KNM's radar, and Rijnmond Radar, which have the range resolutions: 3[m], 30[m], 30[m], 1000[m] and 20[m], respectively.
2. Figure 2.3 shows antenna pattern footprint, computed at constant (maximum) range, 15[km]. This gives an overview of the area that surrounds the space within the radar volume resolution filled with atmospheric particles when the radar is

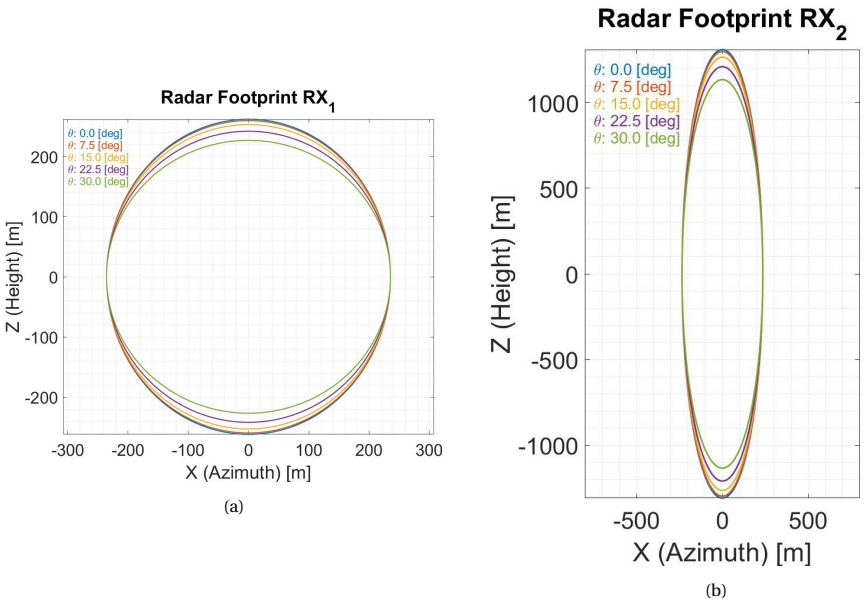

Figure 2.3: MAX3D radar footprint for different elevations at constant (maximum) range: 15 [km], for both RX_1 - Panel(a) and RX_2 - Panel(b)

surveying the sky. For weather radar systems that with scanning area described by a radius of a few hundred kilometers, wind field over the horizontal range does not change much, [1]. In the MAX radar case, the maximum range is 15 [km]. Based on this statement and RX_1 small footprint area of about $500^2[m^2]$ we consider that vertical wind profiles within this space do not change much. However, for RX_2, is difficult to make such an assumption, since the footprint area is about $200 \times 1000[m^2]$.

MAX3D radar disadvantages with respect to weather applications are the following:

1. MAX3D radar height scanning interval range is $[0, 7.5][km]$ for RX_1 and $[7.5, 13][km]$ for RX_2. Because RX_2 has only 8 antenna elements, while RX_1, 40 antenna elements, elevation resolution is much lower for RX_1 (by five times). This difference is also visible in case of antenna pattern footprint, shown in Figure 2.3. In other words this means, that above $7.5[km]$ height, resolution is much lower than below this height, which can be critical for types of clouds that are forming above this height, like is the case for cumulonimbus, that start forming around $10[km]$ height, [2].

2. For $PRF = 952[Hz]$, maximum unambiguous Doppler velocity is $v_{max} = 7.39[m/s]$, i.e. $v_{max} = 26.6[km/h]$. Transformed in *Beaufort* scale, which is a well known scale for wind velocity, this is $v_{max} = 4$ *Beaufort*. Any velocity that exceeds this threshold, it is folded to the opposite side of Doppler velocity spectra.

3. For rotation velocity of MAX in normal scanning mode, $1[rot/s]$, velocity resolution is $\Delta v = 3.69[m/s]$, which means that there are about five sweeps available per resolution cell.

2.2. REAL DATA ANALYSIS

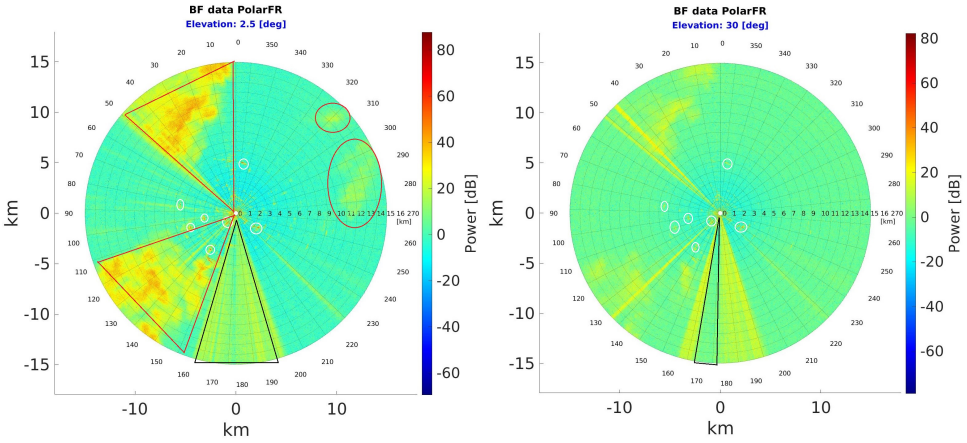

(a) (b)

Figure 2.4: Examples of two constant elevation PPI plots are shown for $\theta = \{2.5°, \theta = 30°\}$, Panel(a) and Panel(b), respectively. Panel(a) shows a strong reflection of ground target clutter, white color circles, whereas in Panel(b) sidelobes' power level decreases. Panel(a) shows the presence of weather target, red color triangle, and circle, whereas, in Panel(b), radial direction corresponds to height values above the center of the weather object. Panel(a) and Panel(b) shows both, fixed azimuth position of power range profiles as the effect of receiver saturation, black color triangle.

This section introduces the analysis of the data artifacts due to the receiver saturation and sidelobes level effect due to the presence of ground clutter targets, in this case, tall strong reflective buildings.

Figure 2.4 shows constant PPI plot for two, different, constant elevations,$\theta = \{2.5°, \theta = 30°\}$. These results are shown for power reflectivity profiles after beamforming (BF), where Fourier (FR) method is used for BF processing and simulation of this results.

The aim for PPI plot at 2.5° constant elevation, Figure 2.4 Panel(a), is to show the effect of sidelobes level due to ground clutter targets, white color circles, and the strong power reflectivity profiles of saturation effect, black color triangle. Additionally, we can remark the presence of weather targets, red color triangles, and circles.

The scope for PPI plot at 30° constant elevation, Figure 2.4 Panel(b) is to show that the sidelobe power level due to ground point target, becomes much lower, about $30[dB]$ less. Moreover, artifacts are present at the range profiles with the same azimuth direction and about the same power level. However, power reflectivity for azimuth direction interval marked by a black color triangle, power reflectivity decreases by about $10[dB]$. Note that the range profiles of power reflectivity as the effect of receiver saturation are fixed in the same azimuth interval for all elevation angles.

The reason for saturation is due to the presence of close objects (up to $10[m]$) to the radar position. Strong reflected power exceeds the $1[dB]$ *compression* point of the amplifier, located on the hardware board before ADC. Due to this, nonlinearities are included in the sinusoidal signal used for the FMCW receiver, which after Fourier Discrete Transformation, performed by the Field-Programmable Gate Array (FPGA) boards, results in harmonics in all spectra. As effect Signal to Noise Ratio (SNR) decreases. For our system, SNR decreases by about $20[dB]$. Later on in this project is shown that this saturation effect presents a broad spectral width, around $4[m/s]$, this is the second moment of Doppler spectrum distribution. Hence, the presence of this saturation from precipitation profiles can be filtered out based on a fixed threshold value for spectral width below $4[m/s]$.

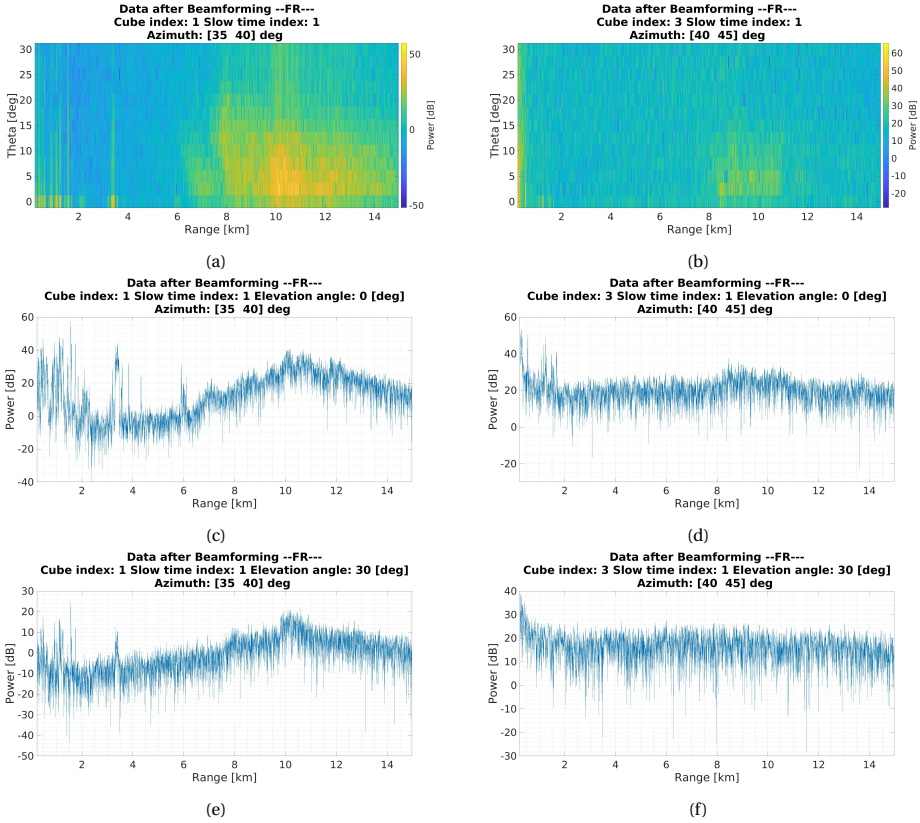

Figure 2.5: Examples of real data results for two constant azimuth: $\phi = 35°$ LHS column and $\phi = 45°$ RHS column. Related with PPI plots, for $\phi = 35°$ there is not saturation visible, but for $\phi = 45°$ saturation is visible while weather targets are present as well. Panel(c) and (e) are extracted from Panel(a) at fixed elevation, $\theta = \{0°, 30°\}$, while Panel(d) and (d), are extracted from Panel(b), at the same elevation angles.

Following discussion introduces results depicted in Figure 2.4. Here, range profiles for each elevation angle, obtained after beamforming processing, using the Fourier method, is depicted for two different constant azimuth directions, $\{\phi = 35°, \theta = 45°\}$, first column,

and second column, respectively.

These simulations provide a qualitative result of the values stated above. Figure rows are organized as follows. The first row shows a 2D image plot of range power profiles versus elevation (vertical axis), the second row show one range power profile at a constant elevation, in this case, close to the ground, $\theta = 0°$, and last row shows one range power profile for the last elevation angle in the scanning interval, that is $\theta = 30°$. Note that for each column 1D plots are extracted from the correspondent 2D image.

On the first column, an example when saturation effect does not occur is depicted, whereas on the second column it occurs. Results from the first column show sidelobes levels spread all over the elevation interval, where for lowest elevation angle power level of sidelobes is about 40$[dB]$, and for the highest is about 10$[dB]$. Second column results show that the power level for the noise level introduced by the saturation effect is constant for both elevation angles, and is about 20$[dB]$. Moreover, in the range power profile for the lowest elevation angle, Panel(d) weather object is drawn under the noise floor.

2.3. NOISE DATA ANALYSIS

This section introduces noise data analysis. Since precipitation profiles are determined in the Doppler domain, the analysis carried out in the following lines is performed for range profiles at particular constant Doppler velocity. Noise data is recorded with MAX3D radar when transmitted is switched off. For this operation, it was necessary only data recorded for a rotation speed of the radar of 60 RPM. Resulted data has the dimension: [40] × [6592] × [952], number of receiving channels, number of range bins, and number of sweeps, respectively. Since azimuth elevation is 1.8°, 200 radar cubes derive per resolution cell, with about 5 sweeps per cube.

The goal of data analysis is to determine to what degree is this information useful for future algorithms. The signal processing toolbox under development in this project includes two algorithms that rely on noise power information. First is the beamforming method that we opted for, rMMSE. This method uses noise covariance matrix, $\boldsymbol{R_n}$, computed for each t^{th} time sample, after all, pulses that correspond to a resolution cell are received. Hence this requires *range profile noise power* per channel, i.e. antenna element. The second algorithm that requires noise power information is the algorithm for target mask creation, the Adaptive Morphological Filtering (AMF) algorithm. For this algorithm is necessary the knowledge of noise power spectrum per elevation.

Thereby, this section shows the methodology and results for averaging range profiles of noise power for Doppler velocity. First, a spatial transformation of whole noise data is applied using the Fourier beamforming method, followed by a Fourier transformation applied for the sweeps within each resolution cell, which results in Doppler spectra. The same operation is applied at each elevation angle. At this point, radar cube is characterized by [elevation] × [range] × [Doppler spectra]. In the final step, the noise power is averaged over Doppler frequencies for all 952 sweeps for each elevation angle. If N is the number of elevation angles, N different range profiles noise power are derivated.

Figure 2.6 Panel(d) shows noise power profiles for $\theta = 0°$, $\theta = 30°$ and averaged one overall elevation angles, blue color line, yellow color line and black color line, respectively. We notice that noise power is range-dependent since for each range bin there is a different value of noise power. This is because noise respects the law imposed to the

amplifier gain control, which has the role to attenuate power reflected from targets close to the radar position.

Figure 2.6 Panel(a) shows the comparison between estimated noise power profile and precipitation profiles. The latter is obtained for $\theta = 10°$, $\phi = 36°$ and Doppler velocity $-1.2[m/s]$. The former is estimated for the elevation angle with the same value. We indeed notice that the noise power profile level is comparable with the floor noise power level. Panel(c) shows the same precipitation profile, in SNR scale, and thresholded for $SNR = 0[dB]$. This last result is a promising one for using this approach for the AMF algorithm since we notice that this method provides a good sensitivity. Finally, Panel(b) shows the same comparison as in Panel(a), but for precipitation profile for a different azimuth angle, $\phi = 45°$. Here we noticed, that the noise power profile is underestimated.

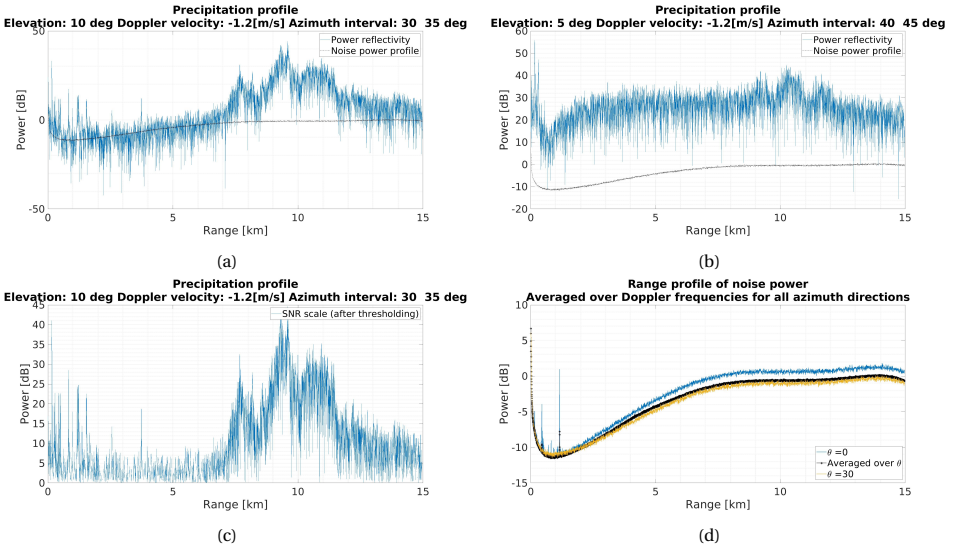

Figure 2.6: Example of noise power profiles and precipitation profiles at constant Doppler velocity $-1.2[m/s]$. Panel(d) shows noise power profiles for two elevation angles, $\theta = \{0°;30°\}$, and black color line the averaged one overall elevations. Panel(a) shows both precipitation profile, blue color line, and noise power profile, black color line. Based on that, Panel(b) shows the same result but in SNR scale, and thresholded at $SNR = 0[dB]$. Panel(b) shows a precipitation profile when the receiver is saturated. The noise power profile is much lower, around 20 dB.

2.4. CONCLUSIONS

In this chapter MAX3D radar parameters, weather data, and noise data have been studied, for the possibility to update the signal processing for this radar for weather applications. The disadvantages, but also advantages of this radar system parameters have been analyzed. The footprint area for both receive antennas was calculated. The conclusion drawn for this is that for the *Main Array* receiver vertical direction of the wind can be considered to not change much for the radar volume resolution filled with atmospheric particles and surveyed by radar. In this case, we can approximate that radial

Doppler velocity for constant height provides true wind velocity up to a scalar, which is dependent on the terminal velocity value of the wind. This is an important conclusion for the success of this project, which final goal is to determine the capability for MAX to perform weather targets detection and 3D wind field estimation.

Real radar data was analyzed for constant elevation PPI of radar power reflectivity after beamforming processing and constant azimuth 2D range profiles for all elevation angles: [elevation] × [range]. Results after beamforming show that it was applied correctly and this can be verified by the visual inspection of sidelobes level for ground target, which is expected to become lower to the high elevation values, which is true for our results. In another train of thoughts, weather targets are visible as clouds shape in range profiles of the PPI plot. Additionally, the behavior of receiver saturation is studied. PPI plots show that high power range profiles due to the saturation effect are present at the same azimuth interval for different elevation angles. 2D image plot of range profiles that correspond with azimuth direction where saturation occurs, shows that this effect occurs for all elevations. Moreover, we observe that the saturation effect implies a decrease of SNR by 20$[dB]$.

Noise data has been studied and range profiles at each elevation angle were estimated for noise power, averaged over Doppler frequencies and all azimuth directions. This result shows to be a good candidate to estimate noise-floor level for data at any position in the processing chain. Here was shown only for precipitation profiles.

REFERENCES

[1] R. J. Doviak and D. S. Zrnić, *Doppler Radar and Weather Observations*, second edition ed. (Elsevier Inc., 1993) pp. ch.9.3, page 300.

[2] F. Mizutani, M. Wada, H. Marui, and H. Handa, *Development of Active Phased Array Weather Radar,* , 2 (2012).

3

WEATHER RADAR SIGNAL SIMULATOR

This chapter includes a simulator technique developed under the objective of simulating the performances of the beamforming technique for weather targets. Due to the goal of estimating Doppler spectra moments, that is total power reflectivity, mean Doppler velocity, and spectral width, beamforming performances are studied concerning the estimation accuracy of spectral moments. Thereby, a simulator for Doppler weather spectra is required. This is developed based on the technique proposed by Dusan S. Zrnic, called Weatherlike Doppler spectra and time signals. Since beamforming operation applies to signal received by a phased array antenna system, this simulation techniques consider the simulation of this signal as well, performed here using instantaneous data model for a phased antenna array. In this chapter, Doppler weather spectra and their moments are introduced. For the latter, physics of atmospheric particles are explained in a radar resolution volume and mathematical derivations have been performed in relation to the radar forward model to support the physics behind. Both components of the simulator are mathematically derived and explained. An extensive explanation about the usage of noise when these two parts of the simulator are combined is provided, followed by the results. Finally, the whole simulator workflow based on the objective of beamforming performance analysis is presented and explained.

3.1. WEATHER DOPPLER SPECTRUM DISTRIBUTION

DOPPLER spectra are used in radar weather applications for estimation of wind and precipitation field. This can be used for the estimation of wind velocity and rain falling intensity. For this, estimation of Doppler weather spectra has to be performed first. This spectra is characterized by three moments, zero moment:*total power reflectivity*, first moment: *mean Doppler velocity* and second moment: *spectral width*(first standard deviation). The first moment can be formulated as a result of the movement of the atmospheric particles concerning the wind velocity in three-dimensional (3D) space,

[1]:

$$\vec{v}_r = \vec{w}sin(\theta) + \vec{u}cos(\theta)cos(\phi) + \vec{v}cos(\theta)sin(\phi) \tag{3.1}$$

, where $\vec{u}$ and $\vec{v}$ represent the components of the horizontal wind velocity, and $\vec{w}$ represents the vertical motion of the particles, known as *vertical draft*. θ and ϕ represent elevation and azimuth angles, respectively, relative to the position of the radar. Estimation of wind velocity based on atmospheric particle movement is possible based on the echo signal reflected by the particle present in the radar resolution volume, [1]:

$$\Delta Vol = R^2\theta\phi\Delta r \tag{3.2}$$

, where $R[m]$ is range, and $\Delta r[m]$ is range resolution. Since these particles have a different dimension that moves with different velocities, hence Doppler weather spectra are characterized by a distribution, which can be approximated with a Gaussian shape distribution, [1]. Finally, the first moment, mean Doppler velocity, $\vec{v}_r$, characterizes the mean velocity of all the particles at each range position and height. The following lines introduce the mathematical derivation of each spectra moment and their relation with the atmospheric particles present in the radar resolution volume.

3.1.1. TOTAL POWER

Total power is the result of power integration along the Doppler spectrum for each range profile, where each frequency (or Doppler velocity) is characterized by a complex value, that here is denoted as $A(k) \in \mathbb{C}$. The number of Doppler pulses/bins: N_D, which represents the number of hits per scan. Doppler spectrum is characterised by velocity resolution: dv, and maximum unambiguous velocity, $|v_{max}|$.

$$dv = \frac{2|v_{max}|}{N_D} \tag{3.3}$$

$$|v_{max}| = \frac{\lambda \cdot PRF}{4} \tag{3.4}$$

$$\boldsymbol{v}_D = -v_{max} : dv : v_{max} - dv \tag{3.5}$$

Formula for total power for one single range bin in terms of Doppler velocity:

$$P_T = \int_{-v_{max}}^{v_{max}} |\hat{A}(v)|^2 dv \tag{3.6}$$

The physical meaning of total power is strictly related to the formulation of radar equation for volume scattering.

$$P_r = \frac{P_t G_t G_r \lambda^2 \sigma_{vol}}{(4\pi)^3 r^4} = \frac{C \cdot \sigma_{vol}}{r^4} \tag{3.7}$$

$$\sigma_{vol} = \sum_{k}^{N_{vol}} \sigma_k = Volume \cdot \sum_{i}^{N(m^3)} \sigma_i = Volume \cdot \eta \tag{3.8}$$

Where, *Volume* represents the radar resolution volume $[m^3]$, σ_{vol} represents the radar cross-section of volume $[m^2]$ and η represents the reflectivity $[m^{-1}]$, which is a summation over unit volume $[m^3]$.

Thereby, if we assume that the radar beam position is fixed for N_D number of scans, and these scans are coherently integrated, then the total power reflectivity represents the total received power from the radar volume at a specific range from radar. Received power in this case is direct proportional with rain rate (mm/h), that is characterised by different diameter values $[mm]$ of the drop size and the total number of drops in unit of volume. Thereby, the higher the rain rate, the higher the value of total power.

3.1.2. MEAN DOPPLER VELOCITY

As a general statement, wind velocity can be estimated using radar systems by integration of phase information provided from the signals reflected by the particles present at a specific time range and in a specific radar volume resolution, when we assume that particles move in space as a consequence of blowing wind. Each radar volume is characterized by a drop size distribution, i.e. Doppler spectrum is characterized by various points with different power and different radial velocity, which creates the so-called Doppler spectrum distribution. The mean of this distribution represents *Mean Doppler velocity*, and we consider this value as being the mean of all radial velocities present at a specific range, azimuth, elevation and time in a radar volume resolution. These moments can be computed as follows:

$$\mu_v = \frac{1}{P_T} \int_{-v_{max}}^{v_{max}} v|\hat{A}(v)|^2 dv \tag{3.9}$$

3.1.3. SPECTRAL WIDTH

The spectral width is computed as the standard deviation of Doppler spectrum distribution and is related to the width of the drop size distribution. When Doppler spectra contain weather objects, this value is empirically around 2 m/s and can be computed using the following formula:

$$\sigma_v = \sqrt{\frac{1}{P_T} \int_{-v_{max}}^{v_{max}} (v-\mu_v)^2 |\hat{A}(v)|^2 dv} \tag{3.10}$$

3.2. ALGORITHM AND MATHEMATICAL DERIVATION

Unlike point target based applications, where the performance of beamforming technique is measured in time domain, in the case of weather applications, the performance analysis of beamforming technique is done based on the estimation accuracy of Doppler moments spectrum distribution. For this reason, a ground truth of the moments values is necessary.

This simulator follows a procedure described by Zrnic, entitled *Weatherlike Doppler Spectra and Signals*, [2] and it is suggested in [3]. The implementation is proposed by us.

This simulator permits the generation of any desired shape for the signal power spectrum. Assuming that Doppler spectrum distribution follows a Gaussian shape distribution, we can use this simulator to reach our objective. Briefly speaking, we generate the first desired Doppler spectra and then the time-series signal is obtained using an Inverse Discrete Fourier Transformation (IDFT).

Based on the simulator's feature to generate any desired spectra, mentioned above, first, a Doppler spectrum is generated. Each frequency value is characterised by power

and phase, where power values are transformed to be exponentially distributed using transformation equation from [2], and phase information if uniformly distributed. To obtain a signal in I and Q components, baseband signal, an inverse discrete Fourier transform of complex Doppler spectrum values are required.

In order to prove that the operations described above are possible from a mathematical point of view, we use the following methodology and formulae, described by Fourier series.

Signal received by an antenna system, is a real signal, where the baseband complex signal, $s(t)$ is modulated on the modulation frequency, f_c:

$$u(t) = \mathbf{Re}\{s(t)e^{jw_c t}\} \tag{3.11}$$

Based on Discrete Fourier Series theory, a signal can be described as a sum of exponential signals, where each of them is characterized by specific frequency and power, as follows:

$$u(t) = \sum_{n=1}^{\Gamma} P_n^{\frac{1}{2}} e^{j\Phi_n} \tag{3.12}$$

where Γ represents the number of complex signals summed together to obtain $u(t)$, P_n represents power of each exponential signal and $\Phi_k = 2\pi f_n t$ is phase information, with f_k being the frequency.

Based on Fourier series derivation, amplitude spectrum coefficients, c_k, which characterise the amplitude of each frequency component in Fourier domain, can be written in terms of I and Q components:

$$c_k = I(k) + jQ(k) = P_k^{\frac{1}{2}} e^{j\Theta_k} \tag{3.13}$$

where P_k represent the power of each sample and is considered exponentially distributed, $\Theta_k = \arctan(Q(k)/I(k))$ is phase information of each sample and is considered uniformly distributed within the interval $[-\pi, \pi]$. I and Q components can be described as follows:

$$I(k) = a(k)\cos(\phi(k)) + n(k)\cos(\psi(k))$$
$$Q(k) = a(k)\sin(\phi(k)) + n(k)\sin(\psi(k))$$

Where, $a(k)$ is a Rayleigh distributed signal envelope and $\phi(k)$ is a uniformly distributed phase. Analog, for $n(k)$ and $\psi(k)$, radar noise. Fourier series equations for discrete signal $u(n)$ is:

$$c_k = \frac{1}{N}\sum_{n=0}^{N-1} u(n)e^{-jn\frac{2\pi}{N}k} \tag{3.14}$$

where N is the number of samples for discrete signal $u(n)$. Based on Eq.3.12 and Eq.3.13, we can rewrite Eq.3.14 as follows:

$$I(k) + jQ(k) = \frac{1}{N}\sum_{n=0}^{N-1} P_n^{\frac{1}{2}} e^{j\Phi_n} e^{-jn\frac{2\pi}{N}k} \tag{3.15}$$

Finally, we notice that the time series signal that corresponds to any Doppler spectra shape can be obtained based on the equation derived in Eq. 3.15, where the shape can be

controlled by the values of P_n. In this case, P_n is exponentially distributed instantaneous power of frequency-dependent signal power density, S_n plus σ_n^2, which is the white noise power per discrete frequency

$$P_n = S_n + \sigma_n^2 \tag{3.16}$$

P_n and Φ_n are statistically independent.

In the following lines I introduce the equations to obtain a complex valued Doppler spectra distribution from a real valued Gaussian one. Doppler spectra implies exponentially distributed power and uniformly distributed phase information.

3.2.1. SIGNAL POWER DENSITY

Doppler spectrum distribution for weather objects is considered to respect the Gaussian shape distribution and can be restored based on the moments values: M_0 (total power reflectivity), M_1 (mean Doppler velocity) and M_2 (first standard deviation). Based on Gaussian formula for normal distribution and moments values we generate each signal power density value, S_n:

$$S_n = \frac{M_0}{\sqrt{2\pi}M_2} e^{-\frac{(v_D(n)-M_1)^2}{2\cdot M_2^2}} \tag{3.17}$$

Where, $n = [1, N]$, N is the number of Doppler bins, and $v_D(k)$ represents the velocity bin within the interval given by the maximum unambiguous velocity, $|v_{max}|$ and velocity resolution, d_v, Eq. 3.3, $v_D(k) = (k-1)d_v - |v_{max}|$.

3.2.2. DOPPLER SPECTRUM DISTRIBUTION

Complex values Doppler spectrum distribution are generated by adding the corresponding noise power, σ_n^2 value to the signal power density, $S(k)$, followed by a transformation of P_n in exponentially distributed random variable. Finally, power signal frequency-dependent values are multiplied by an exponential term for the phase information. For the transformation we use the expression provided in [2]:

$$P_n = -(S_n + \sigma_n^2) \cdot \ln(X_N) \tag{3.18}$$

where X_N is a uniformly distributed random variable within the range 0 to 1. The final equation for Doppler spectrum distribution is:

$$P_n = -(S_n + \sigma_n^2) \cdot \ln(X_n) \cdot e^{j\Theta_n} \tag{3.19}$$

where Θ_n is a uniformly distributed random variable within $[-\pi, \pi]$ interval.

3.2.3. NOISE CHARACTERISTICS

For our simulator, we consider that the noise is White Gaussian Noise (WGN) with zero mean and variance, σ_n^2. Hence, the autocovariance function, c_n and the noise power spectrum density $P(e^{jw})$, respect the following equations:

$$c_n(k) = \sigma_n^2 \delta(k) \tag{3.20}$$

$$P(e^{jw}) = \sum_{k=-\infty}^{k=\infty} r_n(k) e^{-jkw} = \sigma_n^2 \tag{3.21}$$

where r_n represents the autocorrelation function, $c_n(k) = 0$ for $k \neq 0$ and the power spectrum of zero-mean white noise is constant and equal with noise power, σ_n^2.

Since the goal of this simulator is to provide ground truth for all three moments values for data after beamforming, we have to consider that noise variance value, after beamforming operations is reduced by the number of antenna elements, denoted here by M

$$\sigma_{n_{in}}^2 = \frac{\sigma_n^2}{M}. \tag{3.22}$$

Hence, for our simulator Eq. 3.19 is first used with noise included, where noise respects Eq. 3.22, stated above. This result is used only to generate moments ground truth. Second time, Eq. 3.19 is used without noise factor, in order to generate noise-free time series signals, that are later on plugged in the data model for phased array antenna. However, noise power is added in data model as additive noise, where the variance is σ_n^2. The reason why noise variance is excluded for time series signal is that data model requires noise free signals and noise is additive only.

Expected ground truth noise floor, obtained after computing total power moment values, follows the next equation:

$$N\frac{\sigma_n^2}{M} \cdot dv \tag{3.23}$$

where N is the number of Doppler bins, M is the number of antenna elements and dv represent velocity resolution. This formula is derived based on the formula for total power, Eq. 3.6.

3.3. RESULTS

This section introduces the algorithm used to generate weatherlike Doppler spectra and time signals, where moments: M_0, M_1, M_2 and noise variance σ_n^2, represent the input parameters and correspondent time series represent the output. Note that for beamforming performance analysis we are interested in elevation × Doppler velocity matrices. Thus, each moment is a function of elevation. The algorithm to generate times series signals is the following:

1. Generate $\boldsymbol{M_0}$ as superimposed Gaussian shapes, as function of number of targets, maximum power for each target, θ value that correspond with the maximum power of the target and width of each target. The result is shown in Figure 3.1, Panel(a), *M0* subplot. This results is obtained for:

   - Maximum power for each target: [40; 60] dB;
   - Elevation value that correspond with the maximum power: [10°; 25°];
   - Standard deviation: $\sigma = 1.5 m/s$ for both targets.

2. Generate $\boldsymbol{M_1}$ and $\boldsymbol{M_2}$ that corresponds with target mean Doppler velocity and spectral width at each position in space, in terms of elevation. In Figure 3.1, Panel(a), subplot entitled *M1*, respectively *M2*, is presented and example, where *M1* is monotonically increasing along elevation and *M2* is only constant and is 1 m/s.

3. Generate a Gaussian shape for each pair (M_0, M_1, M_2) of input parameters, Figure 3.1, Panel(b), left hand side subplot, entitled *Gaussian Distribution*.

4. Generate a Doppler distribution as function of noise variance, σ_n^2 / M, where power values respects an exponential distribution, Figure 3.1, Panel(b), right hand side subplot, entitled *Doppler Distribution*.

5. Process IDFT for all the rows in the matrix: [elevation] × [Doppler frequency] of Doppler spectra and generate time series signals.

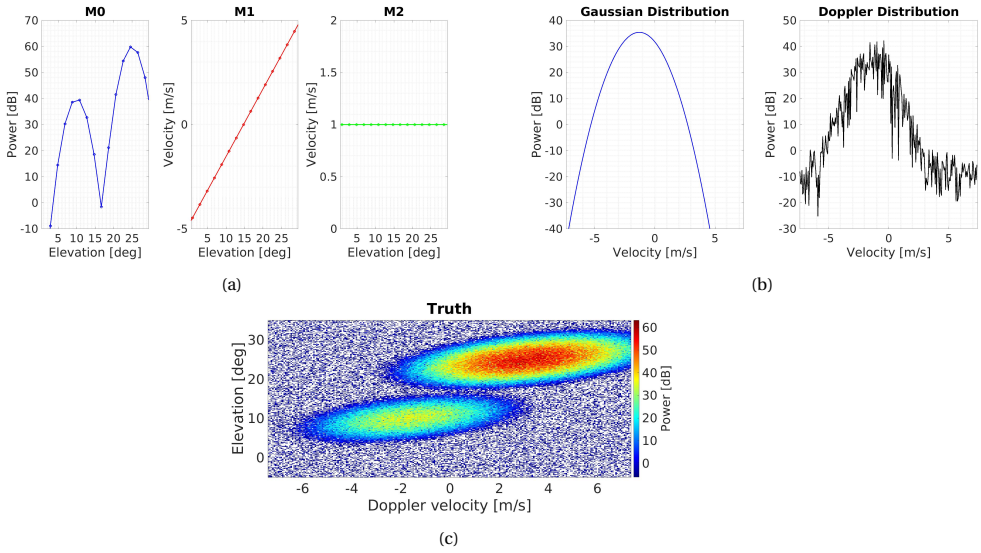

Figure 3.1: Examples of intermediary results obtained for the first part of the simulator.

In Figure 3.1, Panel(c) is shown the 2D image plot of the weather Doppler spectra, generated according with the input values.

3.4. DATA MODEL

In this section *data model* for a uniform linear array (ULA) is introduced. In order to explain this model, some preliminary concepts should be introduced, like complex envelope signal, denoted here as $s(t)$, how this signal is obtained in an I/Q receiver and later, the narrow band assumption. This assumption implies that time delay difference that occurs for the signal to be received by each antenna element is short enough to be neglected, when signal's bandwidth is much smaller than the inverse of this delay, τ.

3.4.1. PRELIMINARY THEORY

I/Q RECEIVER

Signal type used for signal processing operations is the baseband signal, thereby is signal used for our simulator. Henceforth, this signal is denoted by $s(t)$, also known as *complex*

envelope signal. Term *envelope* here refers to the fact that $s(t)$ is an *analytic signal* and magnitude of it is called *envelope of real component*. Analytic signal means that $s(t)$ is an analytic representation of a real-valued function, $x(t)$, containing original signal $x(t)$ and its Hilbert transformation $\mathscr{H}\{x(t)\} = y(t)$,

$$s(t) = x(t) + jy(t), \tag{3.24}$$

where $x(t)$ and $y(t)$ are also known as I(t): in-phase and respectively Q(t): quadrature components [4].

The advantage of this kind of *two-channel* receiver is that it gives us the possibility to compute amplitude, A(t) and phase, $\phi(t)$ of the echo signal reflected by the target, based on separate measurement of I/Q components. Moreover, the sign of the phase shift, $\phi(t)$ can be revealed by the quadrature component. This information gives us the possibility to determine whether the target is approaching or receding to the radar. The processing chain within a radar's receiver is introduced in the following lines.

To begin with, we consider a single received sinusoidal signal at the radar's carrier frequency, f_c. The antenna receives a real-valued bandpass signal with centre frequency. Therefore, the following equation represents the echo signal received by radar, modulated on carrier frequency:

$$u(t) = \boldsymbol{Re}\{s(t)e^{jw_c t}\}. \tag{3.25}$$

Based on Eq.3.24 and Eq.3.25, we obtain the following equation:

$$u(t) = I(t)\cos(w_c t) - Q(t)\sin(w_c t), \tag{3.26}$$

where the equations for I/Q are the following:

$$I(t) = A(t)\cos(\phi(t)),$$
$$Q(t) = A(t)\sin(\phi(t)).$$

In order to extract $s(t)$ out of the received signal $u(t)$, i.e. to obtain I/Q components, two steps are necessary: demodulation and filtration.

1. Multiply $u(t)$ with $2\cos(w_c t)$, respectively with $2\sin(w_c t)$;
2. Apply a LPF (Low Pass Filter) to each resulted component on each channel.

NARROW BAND ASSUMPTION

As stated in the introduction of this section, delay differences, denoted by τ, that occur for the signal to reach out each of the antenna elements are considered small. Here we prove that under this assumption, delayed complex signal, $s(t-\tau)$ is approximately equal with $s(t)$.

We can represent delayed received signal, $u_\tau(t)$, as follows [5]:

$$u_\tau(t) := u(t-\tau) = \mathbf{Re}\{s(t-\tau)e^{-j2\pi f_c \tau}e^{-j2\pi f_c t}\} \tag{3.27}$$

The complex envelope of the delayed signal is:

$$s_\tau(t) = s(t-\tau)e^{-j2\pi f_c \tau} \tag{3.28}$$

Let W be the bandwidth of $s(t)$. If $e(j2\pi f_c \tau) \approx 1$ for all frequencies $|f_c| \leq \frac{W}{2}$, then:

$$s(t-\tau) = \int_{-W/2}^{W/2} S(f) e^{2\pi f(t-\tau)} df \approx \int_{-W/2}^{W/2} S(f) e^{2\pi f(t)} df = s(t) \tag{3.29}$$

Based on Eq. 3.29, we conclude that $s_\tau(t) \approx s(t) e^{-j2\pi f_c \tau}$ for $W * \tau << 1$. In other words, for narrowband signals, small delays can be omitted. This does not mean we can omit phase information provided by that delay.

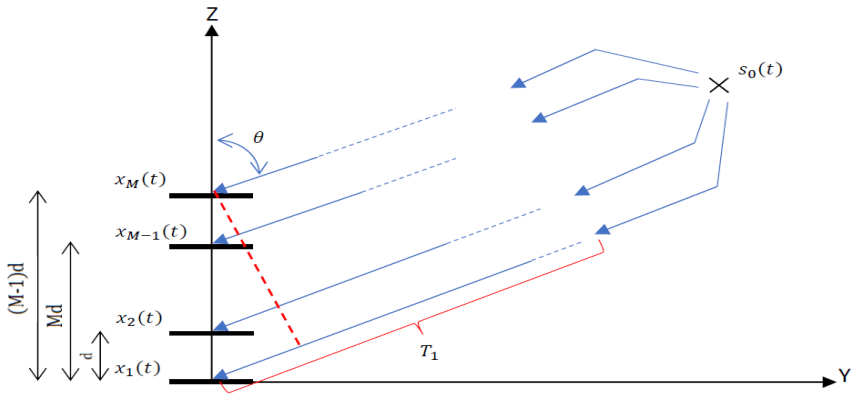

Figure 3.2: Reflected uniform plane wave toward a uniform linear array system of M antenna elements. Signal $s_0(t)$ represent signal with phase delay zero. T_1 represent distance to first element within array, and is the biggest distance when $\theta < 90°$. Dashed red line represent the position in space where signal has the same phase for any points and d represent distance between antenna elements and is constant for uniform linear array (ULA).

3.4.2. DATA MODEL: MATHEMATICAL DERIVATION

Based on Fig. 3.2, we consider the model:

$$x_i(t) = a(\theta) A s_0(t - T_i) e^{-j2\pi f_c T_i}, \tag{3.30}$$

where $a(\theta)$ represents the antenna pattern coefficient as function of θ value, θ angle here is defined as the angle between the target direction and vertical axis, A represent space attenuation, T_i represents the target time delay relative to each antenna element, thus $s_0(t - T_i)$ represents delayed baseband signal, and f_c represent the central frequency, where $s_0(t - T_i) e^{-j2\pi f_c T_i}$ represents reflected modulated signal after receiver. We introduce the following definitions:

$$s(t) = s_0(t - T_1), \tag{3.31}$$

$$\tau_i = T_i - T_1, \tag{3.32}$$

$$\beta = A e^{-j2\pi f_c T_1}, \tag{3.33}$$

where $T_i \leq T_1$, $T_i - T_1 \leq 0$, $\tau_i \leq 0$, i from 1 to M, and τ_i represent a small time delay difference between different antenna elements, and it has a negative value here. Based on this definitions we can rewrite Eq. 3.30 as follows:

$$x_i(t) = a(\theta)\beta s(t-\tau_i)e^{-j2\pi f_c \tau_i} \tag{3.34}$$

Redefining $s_0(t-T_i)$ in this way we can take advantage of the narrowband assumption. Next, τ_i can be expressed as a function of θ and $\Delta = \frac{d_i}{\lambda}$, as follows:

$$2\pi f_c \tau_i = -2\pi f_c \frac{d_i cos(\theta)}{c} = -2\pi \frac{(i-1)d}{\lambda} cos(\theta) = -2\pi(i-1)\Delta cos(\theta) \tag{3.35}$$

where, d represent distance between each two antenna element, which is constant for ULA, Fig. 3.2, c is the speed of light and λ is the signal's wavelength. Minus sign comes from the fact that $\tau_i \leq 0$.

For small τ_i we assume that

$$s_{\tau_i} = s(t-\tau_i)e^{-j\pi f_c \tau_i} \approx s(t)e^{-j\pi f_c \tau_i} = s(t)e^{j2\pi(i-1)\Delta \cos(\theta)}. \tag{3.36}$$

We define $\cos(\theta) = \sin(90° - \theta) = \sin(\theta_h)$, where θ_h represents elevation angle between signal's direction and horizon. Moreover, due to the symmetry of the antenna pattern radiation, we can consider that $a(\theta) = a(\theta_h)$.

After collecting received signals into a vector $\mathbf{x}(t)$, we obtain that

$$\mathbf{x}(t) = \begin{bmatrix} x_1(t) \\ x_2(t) \\ . \\ . \\ . \\ x_M(t) \end{bmatrix} = \begin{bmatrix} 1 \\ e^{j2\pi\Delta sin(\theta_h)} \\ . \\ . \\ . \\ e^{j2\pi(M-1)\Delta \sin(\theta_h)} \end{bmatrix} a(\theta_h)\beta s(t) := \mathbf{a}(\theta_h)\beta s(t). \tag{3.37}$$

Therefore, for our simulator we apply the following steps procedure:

1. Simulate signal $s(t) = s_0(t - T_1)$, where T_1 represent time delay between 1^{st} element in the array and target position in 3D space;
2. Simulate phase information with respect to time delay T_1, contained by β term: $\beta = e^{-j2\pi f_c T_1}$;
3. Simulate phase information with respect to time delay between reflected signal and each antenna element, contained by array response vector $\mathbf{a}(\theta)$. Here we consider that antenna pattern coefficients are 1 for any θ_h angle.

It is important to mention, that for a radar signal, we take into consideration round-trip time. Therefore, T_1 in final model has to be doubled. For multiple, K sources, we can extend the model equation to a matrix form, as follows:

$$\mathbf{X} = \mathbf{ABS} + \mathbf{N}, \tag{3.38}$$

where each component is described as follows:

- matrix **A**, of dimension $M \times K$, where M is the total number of antenna elements and K is the number of sources, contains all the array response vectors $\mathbf{a}(\theta_k)$, $k = 1:K$;
- matrix **B** of dimension $K \times K$, contains β_k, values on diagonal and in rest zero, and contains phase information of the target position with respect to 1^{st} antenna element and also attenuation factor that correspond with for each source's signal;
- matrix **S**, by dimension of $M \times N$, where N is the total number of samples within each signal, contains each $s_{T_k}(t) = s_0(t - T_k)$ signal samples;
- noise matrix **N**, of dimension M by N. We assume noise is spatially white, that means covariance noise matrix $\mathbf{R}_n = \sigma_n^2 \mathbf{I}$.

3.5. SIMULATOR WORKFLOW

This sections shows the simulator workflow, Figure 3.3.

This flowchart has to be read from the left top corner to the right and stops at the bottom center position. Simulator is initiated by plugging in input moments values, $\boldsymbol{M}_0$, $\boldsymbol{M}_1$ and $\boldsymbol{M}_2$. After time-series signals are generated, this is matrix $\boldsymbol{S}$, we use a data model to generate received ULA signals, stored in matrix $\boldsymbol{X}$. After applying the beamforming operation $\hat{\boldsymbol{s}}$ is estimated for each elevation. After Doppler processing and estimation of Doppler weather spectrum moments, the algorithm stops at the bottom center position, where ground truth and estimated moments are compared to determine estimation accuracy.

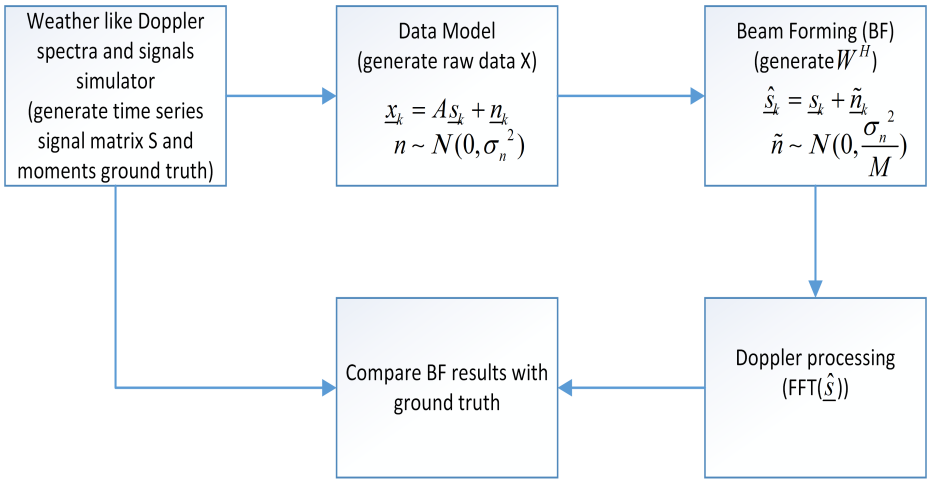

Figure 3.3: Weather Radar Signal Simulator flowchart

3.6. CONCLUSIONS

In this chapter *Weather Radar Signal Simulator* was developed. Mathematical equations for Doppler spectrum moments have been introduced and also the relation be-

tween Doppler weather spectrum and moments. Additionally, an explanation was included about the meaning of each moment for the physics of atmospheric particles.

The simulator has two components: a component that generates Doppler weather spectra and time series signals and another that generates weather data received by a phased antenna array, *data model*. Algorithm and mathematical derivation for the first components were introduced and exact details were provided for the simulation of additive noise for this simulation technique. Physical meaning and the mathematical formulation were discussed for the data model. In the end, a simulator flowchart was introduced and explained.

This simulator is important because it is versatile and allows for the simulation of any desired spectrum shape, in our case, Gaussian shape. Moreover, it allows simulating either extended target or point targets. It provides a realistic behaviour of precipitation profiles for a phased array radar weather. It also offers correct levels for ground truth both for moments and noise level.

REFERENCES

[1] R. J. Doviak and D. S. Zrnić, *Doppler Radar and Weather Observations*, second edition ed. (Elsevier Inc., 1993) pp. 312, ch.9.

[2] D. S. Zrnic, *Simulation of Weatherlike Doppler Spectra and Signals,* J.Appl.Meteorol. **14, no.4**, 619 (June 1975).

[3] E. Yoshikawa, T. Ushio, Z. Kawasaki, S. Yoshida, T. Morimoto, F. Mizutani, and M. Wada, *Mmse beam forming on fast-scanning phased array weather radar,* IEEE Transactions on Geoscience and Remote Sensing **51**, 3077 (2013).

[4] M. Richards, J. Scheer, J. Scheer, and W. Holm, *Principles of Modern Radar: Basic Principles, Volume 1*, Electromagnetics and Radar (Institution of Engineering and Technology, 2010) pp. 287–289.

[5] P. dr ir Geert Leus, *Course: Signal Processing for Communication* (TU Delft, CAS Department, Lecture1: Introduction and wireless channel, pp. 12-15, 2020).

4

BEAMFORMING TECHNIQUE

The beamforming (BF) technique is a signal processing technique used for sensor arrays to steer the beam to a specific direction at transmission and to estimate the direction of arrival at reception. In the weather realm, a phased array antenna improves time and space resolution for 3D information retrieval of the weather situation, which can help prevent consequences due to fast forming atmospheric phenomenon or to improve the understanding of the internal structure of weather. The study of beamforming methods for weather applications implies a more meticulous methodology, that includes the implementation of a weather radar signal simulator. Besides point targets, for weather objects beamforming algorithm has to provide an accurate estimation of precipitation profiles based on the performance criteria 1) sidelobes suppression, 2) accurate estimation of true amplitude and phase information, and 3) robustness to a limited number of Doppler bins, for high time-resolution. One special aspect of our study is to determine the efficiency of the beamforming method when for high power level due to the receiver's saturation. Based on these requirements and aspects, an adaptive beamforming technique is employed, called reiterative Minimum Mean Square Error(rMMSE), and compared with two other beamforming methods; Fourier and Capon.

4.1. MATHEMATICAL DERIVATIONS

FOR this chapter we use data model described in Eq. 3.37. We consider that source power is contained in signal sample, $s(t)$.

4.1.1. SIGNAL MODEL

We assume a 1D uniform linear array (ULA), characterised by M equally-spaced identical elements, with l^{th} time sample of complex signal $\mathbf{x}_l$, $M \times 1$ vector received from the antenna array. This vector can be mathematically described as a linear equation, Eq. 4.1. Matrix $\mathbf{A}$ ($M \times K$) consists of spatial steering vectors $\mathbf{a}(\theta)$, $\mathbf{s}_l$ ($K \times 1$) is the associated received complex vector at arbitrary range bin, and additional White Gaussian Noise (WGN) vector $\mathbf{n}_l$ [$M \times 1$]. K represent the number of angular positions of independent

precipitation profiles.

$$\mathbf{x}_l = \mathbf{A}\mathbf{s}_l + \mathbf{n}_l \tag{4.1}$$

where,

$$\begin{aligned}
\mathbf{x}_l &= \left[x_{l,0} x_{l,1} \cdots x_{l,M-1}\right]^T \\
\mathbf{s}_l &= \left[s_{l,0} s_{l,1} \cdots s_{l,K-1}\right]^T \\
\mathbf{A} &= \left[\mathbf{a}(\theta_0)\, \mathbf{a}(\theta_1) \cdots \mathbf{a}(\theta_{K-1})\right] \\
\mathbf{a}(\theta) &= \left[1 \;\; e^{(-j2\pi\Delta sin(\theta))} \cdots e^{(-j2\pi(M-1)\Delta sin(\theta))}\right]
\end{aligned}$$

and

$$\Delta = \frac{d}{\lambda}$$

$[\bullet]^T$ is transpose operation, d is the spacing of the neighbouring antenna elements, λ is the wavelength. For our system, θ represent elevation angle with respect to antenna broadside.

The objective of the beamforming technique is to optimally construct the weights of a filter, $\mathbf{w}_k$, called beamformer, such that to estimate the precipitation profiles as:

$$\hat{\mathbf{s}}_l = \left[\hat{s}_{l,0}\, \hat{s}_{l,1} \cdots \hat{s}_{l,K-1}\right] \tag{4.2}$$

$$\hat{s}_{l,k} = \mathbf{w}_k^H \mathbf{x}_l \tag{4.3}$$

where $\mathbf{w}_k$ is $[M \times 1]$ weighting vector, computed for a specific elevation angle, θ_k. $[\bullet]^H$ is a complex conjugate transpose. The way how the beamformer is computed depends on the optimality criterion, which is specific to each beamforming technique.

4.1.2. GENERAL MATHEMATICAL BACKGROUND FOR BEAMFORMING

Beamforming technique is a generalization of the linear algebra problem: $\mathbf{X} = \mathbf{AS} + \mathbf{N}$, where either $\mathbf{A}$ or $\mathbf{S}$ is unknown and we have to estimate it. Thereby, we only consider that the array response is known as a function of the direction parameter θ and we are looking to determine $\hat{\mathbf{S}}$, estimation of precipitation profiles. Before introducing beamforming techniques of interest: Fourier, Capon and reiterative MMSE, a summary presentation of the elementary receiver schemes: matched filter and Wiener filter, is necessary to understand the assumptions that we are working with and the mathematical derivation of beamforming techniques under analysis.

According to the model, Eq.4.1, $\mathbf{x}_l$ is a linear combination of K narrowband source signals $s_{l,k}$ and noise $\mathbf{n}_k$, where we assume that the noise covariance matrix

$$\mathbf{R}_n = E[\mathbf{n}_l \mathbf{n}_l^H] \tag{4.4}$$

is known, up to a scalar that represents the noise power. In case of spatially white noise covariance matrix is:

$$\mathbf{R}_n = \sigma^2 \mathbf{I} \tag{4.5}$$

Starting from Eq.4.1, we can assume that we collect L number of sample vectors, $\mathbf{x}_l$, that stored in an $[M \times L]$ matrix $\mathbf{X} = [\mathbf{x}_0, \cdots \mathbf{x}_{L-1}]$, we obtain the following decomposition of $\mathbf{X}$:

$$\mathbf{X} = \mathbf{AS} + \mathbf{N} \tag{4.6}$$

where the rows of $\mathbf{S}$ contain the complex samples of source signals. Here we will assume that signal powers, β_k, are absorbed in $\mathbf{A} = [\mathbf{a}(\theta_0) \cdots \mathbf{a}(\theta_{K-1})] diag[\beta_0 \cdots \beta_{K-1}]$, and that sources have unit powers. We consider sources are stochastic, with zero mean, independent and hence uncorrelated,

$$E[\mathbf{s}_l \mathbf{s}_l^H] = \mathbf{I} \tag{4.7}$$

The approach to solve and understand this problem is the following. First start with the purely deterministic case,

$$\mathbf{X} = \mathbf{AS}, \tag{4.8}$$

where the object is to construct a linear beamforming matrix $\mathbf{W}$ such that

$$\mathbf{W^H X} = \mathbf{S}. \tag{4.9}$$

We will focus only for the case when we know A, sources directions and the complex gains of the sources. For this we set

$$\mathbf{W^H} = \mathbf{A}^\dagger, \quad \mathbf{S} = \mathbf{W^H X} \tag{4.10}$$

In order for $\mathbf{A}^\dagger \mathbf{A} = \mathbf{I}$ to hold we have to respect the following conditions: 1) number of antennas is larger than number of targets, this is $M \geq K$ and columns of A to be linearly independent, this is A to be full rank. If $M < K$ then we cannot recover the sources exactly, because $\mathbf{A}^H \mathbf{A}$ is not invertable. Thereby, if these conditions are met, then $\mathbf{W^H A} = \mathbf{I}$, which guarantees us a beamformer which cancels all interference, because we can estimate $\boldsymbol{S}$ exactly, without errors.

In the presence of additive noise we have: $\mathbf{X} = \mathbf{AS} + \mathbf{N}$. Two types of linear least-square (LS) minimization problems can now be considered: *model fitting error* and *output error minimization*. For the former we take into account only the case when $\mathbf{A}$ is known, and for the latter we consider the case when matrix $\boldsymbol{S}$ is known and based on that we derive receiver expression for known $\boldsymbol{A}$.

$$\min_A ||\mathbf{X} - \mathbf{AS}||_F^2 \tag{4.11}$$

$$\min_W ||\mathbf{W}^H \mathbf{X} - \mathbf{S}||_F^2 \tag{4.12}$$

DETERMINISTIC MODEL FITTING ERROR

For Eq.4.11, with A known we obtain

$$\hat{\mathbf{S}} = \underset{S}{\operatorname{argmin}} ||\mathbf{X} - \mathbf{AS}||_F^2 \Rightarrow \hat{\mathbf{S}} = \mathbf{A}^\dagger \mathbf{X} \tag{4.13}$$

This is known as the *Zero-Forcing solution*, because all interference sources are canceled, i.e. $\mathbf{W^H A} = \mathbf{I}$. ZF maximizes the *Signal-to-Interference power Ratio* (SIR) at the output.

DETERMINISTIC OUTPUT ERROR MINIMIZATION

This optimization problem minimizes the difference between output signals and **S**. The results for known **S** is

$$\mathbf{W}^H = \underset{W}{\operatorname{argmin}} ||\mathbf{W}^H\mathbf{X} - \mathbf{S}||_F^2 = \mathbf{S}\mathbf{X}^\dagger \tag{4.14}$$

Since $\mathbf{X}^\dagger = \mathbf{X}^H(\mathbf{X}\mathbf{X}^H)^{-1}$, we can rewrite Eq.4.14 as

$$\mathbf{W}^H = \frac{1}{L}\mathbf{S}\mathbf{X}^H(\frac{1}{L}\mathbf{X}\mathbf{X}^H)^{-1} = \hat{\mathbf{R}}_{xs}^H\hat{\mathbf{R}}_x^{-1}, \quad \mathbf{W} = \hat{\mathbf{R}}_x^{-1}\hat{\mathbf{R}}_{xs} \tag{4.15}$$

$\hat{\mathbf{R}}_x = \frac{1}{L}\mathbf{X}\mathbf{X}^H$ is the sample covariance matrix (SCM), and $\hat{\mathbf{R}}_{xs} = \frac{1}{L}\mathbf{X}\mathbf{S}^H$ is the sample cross-corelation matrix between sources and received data.

Now, for the beam former derivation when A is known, we have to put certain assumptions on **S** and **N**, because otherwise we cannot solve the minimization problem, since we can fit any **S**. This is that rows of **S** and **N** are statistically independent from each other and hence for large L, we can put together all the assumptions presented so far:

$$\frac{1}{L}\mathbf{S}\mathbf{N}^H \to 0 \quad \frac{1}{L}\mathbf{S}\mathbf{S}^H \to \mathbf{I} \quad \frac{1}{L}\mathbf{N}\mathbf{N}^H \to \sigma^2\mathbf{I}$$

We assumed that the source powers are incorporated in **A**, thus asymptotically we can write **W** as follows

$$\mathbf{W} = \mathbf{R}_x^{-1}\mathbf{R}_{xs} = (\mathbf{A}\mathbf{A}^H + \sigma^2\mathbf{I})^{-1}\mathbf{A} \tag{4.16}$$

This is known as Linear Minimum Mean Square Error (LMMSE) or Wiener receiver. This beam former maximixes the Signal-to-Interference-plus-Noise (SINR) ratio at the output. One observation here is that it does not cancel all interference, $\mathbf{W^H A} \neq \mathbf{I}$. For the *stochastic approach* both matched and wiener filters give the same final formulae when noise is WGN.

For the previous derivations, we took into account some assumptions, that will be valid for all next derivations:

1. White temporally and spatially noise, i.e.

$$\mathbf{R}_n = \sigma^2\mathbf{I}; \tag{4.17}$$

2. Signals are stochastic, zero mean, independent and hence uncorrelated, for unitary signals, this means

$$\frac{1}{L}\mathbf{S}\mathbf{S}^H = \mathbf{I}; \tag{4.18}$$

3. Number of antennas has to be larger or equal than number of sources: $M \geq K$, in order to recover the sources exactly;

4. This is not an assumption, but an important matter: in order to compute SCM, $\hat{\mathbf{R}}_x$, we have to take into account that each instance of a random variable $x_{m,l}$ of matrix **X**, has to belong to the same random process. This means that for our case, the beamforming technique that uses SCM has to be applied for data collected over slow time from the same target, that is fixed range and slow time axis.

4.2. METHODS UNDER ANALYSIS

In this section I present three beamforming techniques: *Fourier*, *Capon* and *re-iterative MMSE*. The presented formulas follow the same concepts derived for ZF and Wiener, except that we introduce $a(\theta)$, where θ represent the elevation angle value, employed for space scanning and retrieval of precipitation profiles for the elevation interval of interest.

4.2.1. FOURIER - MF

Fourier beamforming, known also as *Matched Filter* (MF) beamformer can be derived based on the receivers obtained in previous subsections: ZF and Wiener if we assume only the case of one single target in noise

$$\mathbf{x}_l = \mathbf{a}(\theta)\, s_l + \mathbf{n}_l \tag{4.19}$$

By recomputing formulas for both, ZF and Wiener receivers, where matrix $\mathbf{A}$ is replaced by simply vector $\mathbf{a}(\theta)$ we notice that the difference between ZF and Wiener receiver is only a scalar multiplication: $\gamma\mathbf{a}(\theta)$, which does not change the output SNR. Hence the optimal beamformer, when noise is spatially white is:

$$\mathbf{w}_{FR_k} = \frac{\mathbf{a}(\theta_\mathbf{k})}{M} \tag{4.20}$$

This algorithm is known as *Fourier* (FR), because a precipitation profile estimated by using the FR weights is equivalent to the result of a Fourier transformation of $\mathbf{x}_l$.

4.2.2. LCMV - MVDR - CAPON

Another technique for beamforming, is called *Linearly constrained Minimum Variance* (LCMV), also known as *Minimum Variance Distortionless Response* (MVDR) and *Capon* beamforming. As for MF we assume the case of one single signal in noise. For known $\mathbf{a}(\theta_k)$, received power is minimized subject to a constraint, as follows:

$$\min_w \mathbf{w}^H \mathbf{R}_x \mathbf{w} \tag{4.21}$$

$$s.t.\ \mathbf{w}\mathbf{a}(\theta_\mathbf{k}) = 1, \tag{4.22}$$

which implies having a fixed response towards a source coming from that specific direction. The solution can be found in closed form using Lagrange multipliers and is given by

$$\mathbf{w}_{CP_k} = \frac{\mathbf{R}_x^{-1}\mathbf{a}(\theta_k)}{\mathbf{a}^H(\theta_k)\mathbf{R}_x^{-1}\mathbf{a}(\theta_k)} \tag{4.23}$$

where for large L

$$\mathbf{R}_x = \frac{1}{L}\mathbf{X}\mathbf{X}^H \tag{4.24}$$

Since we work with small amount of samples, L small, then we consider that SCM is only an approximation, denoted: $\hat{\mathbf{R}}_x$.

4.2.3. REITERATIVE MMSE

MMSE beamforming for adaptive phase array was proposed in [1], where its performances were computed for point target, and thereafter it was proposed in [2], where the algorithm is tested for precipitation profiles. In the latter, the authors upgraded the algorithm with a gain constrain, similar with one applied for Capon beamformer. Hence the MMSE beamformer is

$$\mathbf{w}_{MMSE_k} = \frac{\mathbf{R}^{-1}\mathbf{a}(\theta_k)}{\mathbf{a}^H(\theta_k)\mathbf{R}^{-1}\mathbf{a}(\theta_k)} \tag{4.25}$$

where

$$\mathbf{R} = \mathbf{A}\mathbf{R}_s\mathbf{A}^H + \mathbf{R}_n \tag{4.26}$$

As we can already notice, the main difference between Capon and MMSE is that we descompose SCM, denoted here with $\mathbf{R}$. In this way we have a structure that allows us to control the noise covariance matrix, $\mathbf{R}_n$. Moreover, this opens the possibility to make this algorithm reiterative, abbreviated from now as *rMMSE*, where for each iteration SCM is upgraded. It is initialized using Fourier beamformer. For this algorithm we assume that signals powers, β_k are absorbed in $\mathbf{s}_k$, i.e. $\mathbf{R}_s = diag[\beta_0 \cdots \beta_{K-1}]\mathbf{I}_{K\times K}$, called spatial covariance matrix.

The rMMSE weight and solution are calculated iteratively with the use of prior information as follows.

1. *Prior Information:* Fourier beamformer is used to obtain an estimate of precipitation profiles as prior information.

$$\hat{\mathbf{R}}_s^0 = \frac{1}{L}\hat{\mathbf{S}}_{FR}\hat{\mathbf{S}}_{FR}^H \odot \mathbf{I}_{K\times K} \tag{4.27}$$

where

$$\hat{\mathbf{S}}_{FR} = [\hat{\mathbf{s}}_0 \cdots \hat{\mathbf{s}}_{L-1}]$$
$$\hat{\mathbf{S}}_{FR} = \mathbf{W}_{FR}^H\mathbf{X}$$
$$\mathbf{W}_{FR} = [\mathbf{a}(\theta_0) \cdots \mathbf{a}(\theta_{K-1})]$$

L is the number of time samples, and K is the number of different angles value that are used to scan θ along elevation interval.

2. *Computation of weight vectors:* For each i-iteration a new weight vector, $\mathbf{w}_{MMSE_k}^{(i)}$ is computed, based on the previous updated space covariance matrix, $\hat{\mathbf{R}}_s^{(i)}$.

$$\mathbf{w}_{MMSE_k}^{(i)} = \frac{\mathbf{R}^{(i)^{-1}}\mathbf{a}(\theta_k)}{\mathbf{a}^H(\theta_k)\mathbf{R}^{(i)^{-1}}\mathbf{a}(\theta_k)} \tag{4.28}$$

where

$$\mathbf{R}^{(i)} = \mathbf{A}\mathbf{R}_s^{(i)}\mathbf{A}^H + \mathbf{R}_n \tag{4.29}$$

3. *Determination of rMMSE solutions:* K new solutions are computed for each new set of weight vectors in order to update space covariance matrix, $\mathbf{R}_s^{(i)}$.

$$\hat{\mathbf{S}}_{rMMSE}^{(i)} = \mathbf{W}_{rMMSE}^{(i)^H}\mathbf{X} \tag{4.30}$$
$$\mathbf{W}_{rMMSE}^{(i)} = [\mathbf{w}_{MMSE_0}^{(i)} \cdots \mathbf{w}_{MMSE_{K-1}}^{(i)}] \tag{4.31}$$

4. *Reiteration:* i+1 iterative space covariance matrix, $\hat{\mathbf{R}}_s$, calculated using i-iterative rMMSE solutions.

$$\hat{\mathbf{R}}_s^{i+1} = \frac{1}{L}\hat{\mathbf{S}}_{rMMSE}^{(i)}\hat{\mathbf{S}}_{rMMSE}^{(i)H} \odot \mathbf{I}_{K\times K} \tag{4.32}$$

After this point algorithm continue from point number *2*, with computation of new weight vectors.

In order for the algorithm to stop, the iteration is terminated with a threshold of normalized mean square errors (NMSEs) between i-iterative and i-1 iterative MMSE solutions

$$\delta_i = \frac{1}{N}\sum_{n=1}^{N}\left(\frac{\sum_{l=1}^{L}||\hat{\mathbf{s}}_{MMSE_{l,k}}^{(i)} - \hat{\mathbf{s}}_{MMSE_{l,k}}^{(i-1)}||^2}{\sum_{l=1}^{L}||\hat{\mathbf{s}}_{MMSE_{l,k}}^{(i-1)}||^2}\right) \tag{4.33}$$

where the NMSEs in each range bin are averaged. Hereafter, output result for rMMSE that satisfies, Eq.4.33, it is called converged MMSE, with i number of iterations, denoted henceforth cMMSEi. For avoiding any confusion, when we remember about algorithm itself we call it rMMSE, but when we discuss about a specific results, where we have available a number of iterations we will use cMMSE(i), and specific number of iterations for that case.

4.3. NUMERICAL SIMULATION

This section evaluates the simulated performances of rMMSE beamforming method, taking into account imposed requirements, mentioned in the abstract: 1) sidelobes suppression, 2) accurate estimation of true amplitude and phase information and 3) robustness to a limited number of Doppler bins. For this simulation we consider that antenna elements are perfectly calibrated, this means same phase difference value for any two successive antenna elements.

This beamforming method is proposed by Eiichi Yoshikawa and et al., where its performances are demonstrated, for simulated data, in [2]. In [3] an upgrade for rMMSE method is provided, in order to overcome phase and amplitude issues, which is likely to happen for a phased array antenna. The role of this section is to test if our algorithm is correctly implemented, which means that we try to reproduce the performances obtained in [2]. For this we compare rMMSE results to Fourier(FR), not-adaptive method, and to Capon(CP), adaptive method, for both point and extended (weather) targets. One additional study result that we provide, compared with [2], is about the algorithm performances for the case of underestimation or overestimation of noise variance, parameter used to compute noise covariance matrix, $\boldsymbol{R}_n$.

Therefore, this section is split in *three* parts. In *first* part, we introduce the qualitative differences between point target and extended target, with respect to total power, that is M_0 moment, and antenna spatial response results, where quantitative results are provided for the point target results with respect to the total power error estimation. The objective is to prove the following performances for rMMSE: 1) sidelobes suppression, 2) small errors for power estimation, 3) adaptive performances of the algorithm and to understand the differences for an extended target compared with a point one when beamforming is applied. In the *second* part, a study is carried out for two extended

targets, where qualitative and quantitative results are provided with respect to all three moments, for both 256 and 16 Doppler bins. The objective is to prove the performances of rMMSE for 1) accurate estimation of precipitation profiles and 2) robustness to the small number of Doppler bins. In the end, 2D image plots of the Doppler spectra are provided, for visualization analysis of the performance of rMMSE with respect to ground truth and other two employed beamforming methods. In the *last* part we provide the results for rMMSE when noise variance is either overestimated or underestimated.

4.3.1. POINT AND EXTENDED TARGETS

In this subsection are introduced qualitative differences between point target and extended target, Figure 4.1 and quantitative results, Table 4.2 for point target only with respect to power estimation error. For this, in Figure 4.1 are shown simulation results for two-point target, LHS column of plots and one extended target, RHS column of plots. The blue, green and red solid lines are FR, CP and cMMSE, respectively. Both total power estimate and antenna spatial response are shown in this figure. For this simulation results we use *Weather Radar Signals Simulator*, thus input parameters values are depicted in Table 4.1. Point targets are simulated with different power values, in order to observe beamforming performances at different SNR's. Ground truth noise floor computed for M_0, denoted $\sigma^2_{n_{M_0}}$ is computed based on Eq. 3.23. Antenna spatial response provides a spatial characterization of performances of the weight coefficients computed for each beamforming method. This gives us an impression of the adaptive nature of CP and rMMSE, compared with the non-adaptive FR method. For these simulation results, noise variance, σ^2_n is computed based on input SNR value, where SNR here is described by the power ratio of the highest power in the spectra and noise power.

	Point Targets		
	LHS target	**RHS target**	**Extended Target**
Parameter	*Value*	*Value*	*Value*
θ_{steer}	$[-5°;35°]$		
θ_{tg}	15°	25°	20°
$\Delta\theta$	0.1°		0.97°
P	20 dB	40 dB	40 dB
SNR	30 dB		
σ^2_n	10 dB		
$\sigma^2_{n_{M_0}}$	5.7 dB		
Doppler bins	256		256

Table 4.1: Input parameter values for point and extended targets comparison results

Some parameters shown in Table 4.1, require some additional explanations. Thus, θ_{steer} represents the interval of steering elevation angles used for beamforming algorithm, where $\Delta\theta$ represents elevation resolution used for steering angles, the higher is the resolution the more smoother are the results. This high resolution of $\Delta\theta = 0.1°$ is helpful to determine sidelobes level, especially for point targets results, and for antenna spatial response. However, for extended target results, Panel(b), we used $\Delta\theta = 0.97°$. For

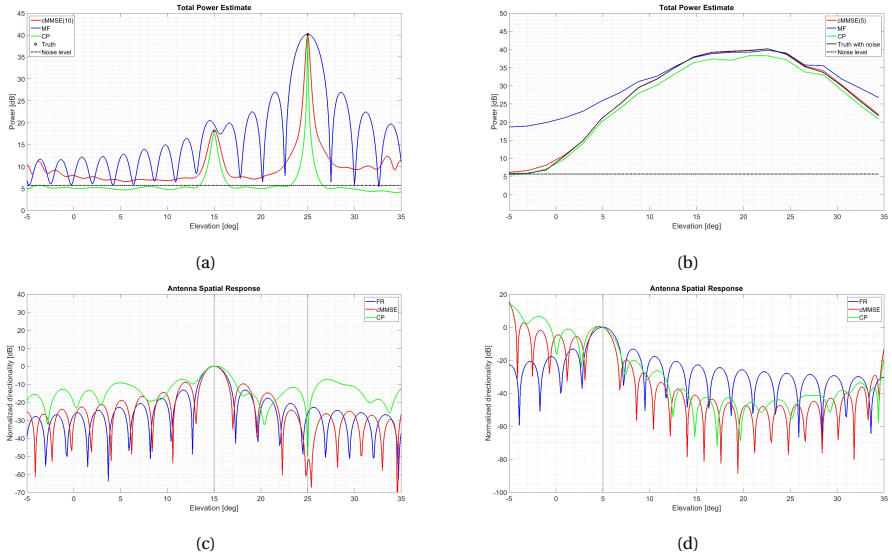

Figure 4.1: Example of total power and antenna spatial response for two point targets, Panel(a), respectively Panel(c) and one extended target Panel (b), respectively (d). Panel(a) shows the total power estimates for two point targets placed at 15° and 25°, respectively, where blue solid, green solid and red solid lines indicate the results for FR, CP and cMMSE, respectively. Black circles and horizontal dashed line indicate true (θ,power) and ground truth noise level, respectively. In Panel(c), antenna spatial response is computed at an grazing angle of 15°. Panel(b) shows the total power estimate for one distributed target, black lines represent ground truth for total power. In Panel (d), antenna spatial response is computed for a grazing angle of 5°.

the Doppler bins we used 256, because in this simulation we are not interested to test if algorithm is robust to small number of Doppler bins. For SNR = 30 dB and maximum power in the spectra 40 dB, we obtain a noise variance value of $\sigma_n^2 = 10dB$, and a ground truth noise level for M_0 of $\sigma^2_{n_{M_0}}$ = 5.7 dB. Error estimation values of total power for the two point targets case are depicted in Table 4.2.

Observations about results are provided in the following lines. Firstly we start with results regarding point targets. For these observations we relate power error estimation results from Table 4.2 with qualitative results from Figure 4.1, Panel(a) and (c). Hence, FR estimates correctly the total power for the target on the RHS, but has the poorest resolution and the highest level of sidelobes, compared with CP or cMMSE(10). LHS target is hidden under the sidelobes, and power estimation is overestimated by about 1.33 dB. Even if CP algorithm correctly detects both targets with high resolution and low sidelobes level, both received power are underestimated about -0.48 dB and -0.76, for the left and right target, respectively. The reason for underestimation is the correlation between signals originated from targets and signals and noise. cMMSE(10) shows high resolution with low sidelobes level and provide the best estimation for both targets. Based on Panel(c) we notice that both cMMSE(10) and CP forms a null at elevation angle 25°. Nevertheless, cMMSE(10) has the same beamwidth as FR, which means that rMMSE technique does not sharpen main lobes, but only suppress sidelobes in an adaptive way.

	LHS target	**RHS target**
Beamforming Method	*Value[dB]*	*Value[dB]*
FR	-1.33	0.001
CP	0.48	0.76
cMMSE	-0.18	-0.02

Table 4.2: Total Power Error Estimation For The Two Point Targets

Regarding weather target, results for total power and antenna spatial response are shown in Figure 4.1, Panel(b) and (d), respectively. Solid black line represent the ground truth for the total power and dashed horizontal line represent $\sigma^2_{n_{M_0}}$. Hence, FR shows sidelobes under 12° and above 26° elevation. Although CP does not present sidelobes, it underestimates total power, because of the correlation between signals coming from all elevations. In this case, cMMSE(5) correctly estimates total power, solving the problem of underestimation and sidelobes. In Panel(c), the antenna spatial response for an arbitrary elevation angle, 5° is shown. We notice that the beamforming weights for both CP and cMMSE(5) are computed according with the total power for each elevation, Panel(d).

4.3.2. ESTIMATION ACCURACY FOR DISTRIBUTED TARGETS

In this subsection we study rMMSE performances for extended targets only. Thus, performance analysis of rMMSE compared with FR and CP is carried out with respect to all three moments and for different Doppler bins, 16 and 256. Qualitative and quantitative results are provided, Figure 4.2 and Table 4.4, respectively. Figure 4.2 structure contains three rows: 1) total power reflectivity, 2) Mean Doppler velocity and 3) spectral width and two columns: 1) analysis for 16 Doppler bins, and 2) for 256 Doppler bins. Blue, green and red solid lines correspond with results for FR, CP and rMMSE, respectively.

Table 4.4 contains *mean bias* and *standard deviation* values, parameters derived in Eq.4.34, that are computed per each beamforming method, per each Doppler bins, denoted here by L, L = 16 and L = 256, and per each area of interest, highlighted in Figure 4.2 with light yellow and blue light. Light yellow area represents the *main lobes*, with respect to FR method, and light blue area represent the *sidelobes*, with respect to FR method. Note that light blue area does not contain elevation angles where only noise is present.

$$\mu_{bias} = \frac{\sum_{n=1}^{K} \boldsymbol{M}_i(n) - \hat{\boldsymbol{M}}_i(n)}{K} \tag{4.34}$$

$$\sigma_{dev} = \sqrt{\frac{\sum_{n=1}^{K} (\boldsymbol{M}_i(n) - \hat{\boldsymbol{M}}_i(n) - \mu_{bias})^2}{K}} \tag{4.35}$$

For this study we simulate two extended target, whose input parameters are shown in Table 4.3. SNR is described here by the power ratio of the highest power in the spectra and noise power. SNR = 50 dB, gives us a noise variance value of $\sigma_n^2 = 10dB$, and a ground truth noise level of 5.7 dB. θ_{tg} represents the location of the maximum power of each target, $\Delta\theta$ represent beamforming resolution, σ_D represent each target width, and Doppler bins are different in order to analyse the robustness to low number of bins.

	Extended Targets	
	LHS target	**RHS target**
Parameter	*Value*	*Value*
θ_{steer}	$[-0.5°;35°]$	
θ_{tg}	10°	25°
$\Delta\theta$	0.97°	
P	40 dB	60 dB
SNR	50 dB	
σ_n^2	10 dB	
$\sigma^2_{n_{M_0}}$	5.7 dB	
Doppler bins	16 and 256	
σ_D	1.5 m/s	

Table 4.3: Input parameters values for extended targets

		beyond noise level between 2.8 and 32.4 deg (blue colored area)				beyond noise level between intervals [8.7,10.7] deg and [22.6,26.5] deg (yellow colored areas)			
		L = 16		L = 256		L = 16		L = 256	
		mean bias	standard deviation	mean bias	standard deviation	mean bias	standard deviation	mean bias	standard deviation
FR	total power [dB]	-13.93	13.51	-13.65	13.09	-0.19	1.32	0.11	0.82
	mean Doppler velocity [m/s]	1.98	1.59	1.95	1.51	0.72	0.91	0.55	0.74
	spectral width [m/s]	0.98	0.90	1	1.06	0.79	0.94	0.59	0.77
CP	total power [dB]	224.8	9.58	0.83	2.29	224.77	8.47	2.15	0.30
	mean Doppler velocity [m/s]	1.84	1.69	0.31	0.20	1.05	1.59	0.32	0.09
	spectral width [m/s]	3.29	1.19	0.81	0.30	3.55	0.88	1.09	0.13
cMMSE	total power [dB]	-0.74	1.94	-0.77	2.12	0.005	0.04	0.003	0.015
	mean Doppler velocity [m/s]	0.26	0.50	0.11	0.19	0.004	0.003	0.0006	0.0004
	spectral width [m/s]	0.17	0.28	0.14	0.26	0.005	0.006	0.001	0.0008

Table 4.4: Estimation of the accuracy for distributed targets

Observations about results are provided in the following lines. FR results are characterized by sidelobes and errors in terms of power estimation. FR provides the less amount of errors for elevation ranges: [8.7°,10.7°] and [22.6°,26.5°], which corresponds with the main lobes for LHS and RHS target, respectively. Mean Doppler velocity and spectral width results, for FR, are closer to the truth values only within intervals where total power is correctly estimated. Similar results are shown for both cases, L = 16 and L = 256, which means FR is independent on the number of Doppler bins. On the other hand, CP shows dependency regarding Doppler bins, where for L = 16, total power estimation for CP is not visible in captured interval, Panel(a). Next we can notice that cMMSE(6) performances are more superior compared with FR and CP.

A qualitative evaluation of estimation accuracies is provided in Table 4.4. As we can see, based on the results presented in this table, CP cannot provide valid results when L = 16. FR and cMMSE provide similar mean bias and standard deviation for both values of Doppler bins (L), when we analyse data for yellow area. cMMSE errors for all moments are under 1 dB, in terms of M_0 and 1 m/s, for M_1 and M_2 for both regions of analysis.

To understand the reason for biased results in case of FR or CP, Fig.4.3 shows the spec-

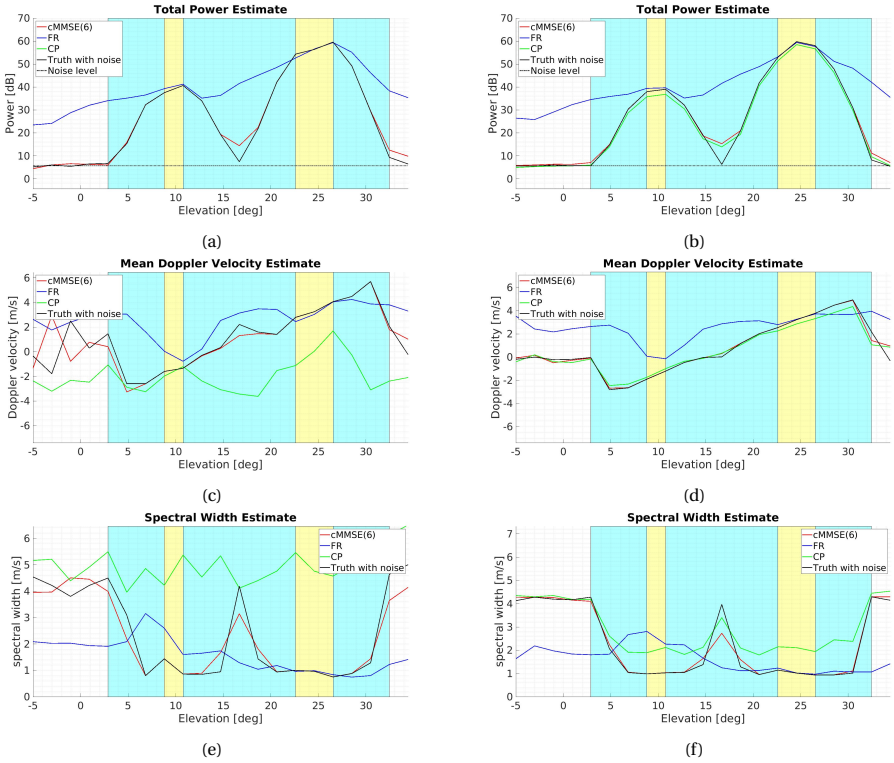

Figure 4.2: Example of estimation performances for three beamforming techniques, cMMSE, FR and CP, red line, blue line and green line respectively. Figure is split in three rows and two columns. First column results corresponds with 16 Doppler bins and second column results with 256 Doppler bins. First, second and third row shows M_0, M_1 and M_2, respectively. Light yellow area represent the main lobe area and blue light sidelobes for FR, where the difference is that power error estimation for yellow area is much smaller, compared with the blue area. Ground truth for $\boldsymbol{M_0}$,$\boldsymbol{M_1}$ and $\boldsymbol{M_2}$ are the same as those presented in Figure 3.1.

trographs, this is the elevation-Doppler 2D image plots, for all three methods and truth. To emphasize the difference between algorithms, a threshold is applied, equal with the theoretical noise power after beamforming: $\frac{\sigma^2}{M}$. Additionally, spectrographs were computed for both $L = 16$ and $L = 256$, left and right column, respectively. For $L = 16$ CP results were meaningless, so image plot is dropped. Based on Panel(d), FR methods creates sidelobes that interfere with other elevation angles, which creates overestimation errors. However, these sidelobes are cancelled for cMMSE(6) case. Even if CP creates sidelobes along Doppler spectrum, i.e. multiples harmonics, this effect is only visible for spectral width estimation case, Fig.4.4, Panel(f), where CP we notice CP suffers of overestimation. Comparing cMMSE results, Panel(f) and (g) with ground truth results, Panel(a) and (b) we can remark close similarities.

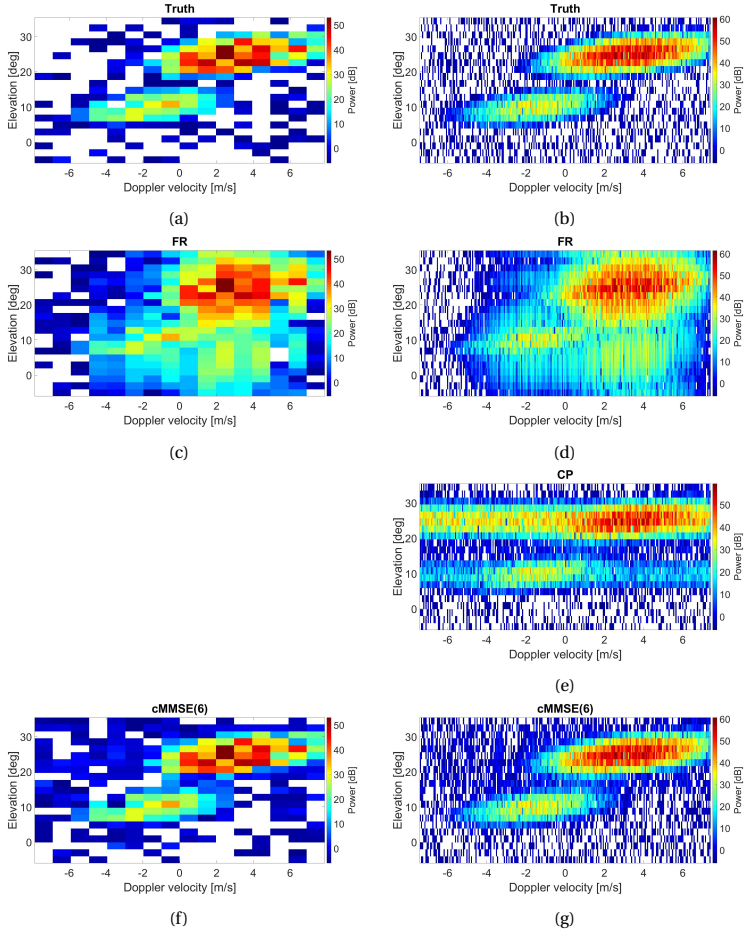

Figure 4.3: Examples of spectrographs for all three methods: FR, CP and cMMSE compared with result for true values. Two different sets of results:left for L=16 and right for L=256. CP's results for L=16 are meaningless, so they are not shown. A threshold is applied, which corresponds with theretical noise level for noise power after beamforming: σ_n^2/M, where σ_n^2 is additive noise power and M are the number of antenna elements. Based on these results we can understand the characteristics of each method and explain the estimated accuracies results, from both Fig.4.2 and Tabel 4.4.

4.3.3. REITERATIVE MMSE ESTIMATION ACCURACY WHEN NOISE VARIANCE IS NOT CORRECTLY ESTIMATED

In this subsection we study the rMMSE estimation accuracy when noise variance varies from true value, with -10 dB and +10 dB,respectively. For this, we are using *Weather radar signals simulator* and input parameter values shown in Table 4.3. For this, we repeat same simulation with two different values for noise variance: 1) $\sigma_n^2 = 0dB$, 2) $\sigma_n^2 = 20dB$ and we compute mean bias and standard deviation of the rMMSE method results within blue area only, Figure 4.2, in the same fashion as we did in Table 4.4, for both deviated noise variance values and true noise variance results. Moreover, we focus also on the

number of iterations necessary for each simulation type. Results are shown in Table 4.5.

	$\sigma_n^2 = 0$ **dB**		$\sigma_n^2 = 10$ **dB (true value)**		$\sigma_n^2 = 20$ **dB**	
Parameters	*mean bias*	*standard deviation*	*mean bias*	*standard deviation*	*mean bias*	*standard deviation*
total power [dB]	-1.8	3.5	-0.85	2.3	-0.99	2.75
mean Doppler velocity [m/s]	0.24	0.54	0.16	0.38	0.17	0.32
spectral width [m/s]	0.32	0.48	0.13	0.27	0.20	0.49
Number of iterations (i)	8		6		5	

Table 4.5: Estimation accuracies for rMMSE when noise variance deviates from true value

Based on the quantitative results shown in Table 4.5, we notice first that the number of iterations varies, where there are necessary two more iterations when noise is underestimated, 8 in this case, and 1 fewer iteration when noise is overestimated, 5 in this case. However, we notice that for underestimated case total power varies from the true value in average with one more dB than in the case of true noise variance. Nevertheless, for M_1 and M_2, accuracy errors are around 0.15 m/s only. On the other hand, for overestimated case, we notice much fewer errors than in other cases, where mean bias and standard deviation are very close to the true noise variance case.

To conclude, this result helps us to understand to what degree an incorrect estimation of noise variance, and therefore of the noise covariance matrix can decrease rMMSE performances in terms of estimation accuracy. Based on the results shown in this subsection, we can conclude that rMMSE provides more accuracy errors for the underestimation case than for the overestimation case. Therefore, a solution to be sure that we are not underestimating this value is to add 10 dB extra to the actual estimated value of noise variance.

4.4. MAX3D DATA SIMULATION

In this section, we introduce the rMMSE beamforming performances for radar data received with MAX3D using data received by *Main Array* only. This data is called in this report *real data*. Based on [3], rMMSE results converge to FR ones if the variance of amplitude and phase difference errors between successive antenna elements are more than a specific threshold. Hence, for our real data, we expect that rMMSE results can converge to FR, thus we use FR results for comparison. Moreover, CP results are also used as a reference, since we use 256 Doppler bins data, the value that for simulated results CP showed similar performances as rMMSE, up to a scalar error.

In this section we focus on the requirements set for the choice of beamforming algorithm and for two other aspects, listed as follows:

1. *Sidelobes suppression.* For this, we select a specific azimuth and range position where we find a ground target and we process Elevation-Doppler map for that fixed range, for data provided from all three beamforming techniques. Then we compare all three moments for all three beamforming methods.

2. *Accurate estimation of true amplitude and phase information.* For true amplitude, we compare main lobes results for total power between rMMSE and FR. For phase information, we already saw for simulated data that rMMSE provides better accuracy estimation than FR, thus for M_1 and M_2 we are just analyzing the differences between rMMSE and FR, respectively CP.

3. *Robustness for a small number of Doppler bins.* This was already proved for simulated data, hence we do not have to prove it for real data.

4. *Saturation sidelobes suppression.* This is not a requirement, but only an important aspect that we consider in this project, thus we compare rMMSE results with FR, respectively cMMSE for this matter.

5. Finally, we analyze Elevation-Doppler and Range-Doppler map results for all three methods, to determine the differences, when there is a weather target present in scanned space.

Values for input parameters used in this simulation are shown in Table 4.6.

Real data parameters	
Parameter	*Value*
RX	Main Array
θ	[0°;30°]
$\Delta\theta$	2.5°
DBF beams	13
Rotation velocity	1 RPM
Doppler bins	256

Table 4.6: Real data parameters of interest

An important aspect, before simulation results, is to mention that for noise covariance matrix, used for rMMSE we consider that noise is independent, but not identical, thus noise variance is different for each element on diagonal. In order to compute $\boldsymbol{R}_n$ we use the results obtained in Chapter 3, Figure 2.6, for raw data. Thus, diagonal values for $\boldsymbol{R}_n$ varies along channels, and $\boldsymbol{R}_n$ is recomputed for each correspondent range bin since noise variance is varying along the range. In order to stop reiterative process of rMMSE, we use the same threshold value as used for simulated data, an proposed in [2], $th = 0.001$.

4.4.1. SIDELOBES SUPPRESSION

In this subsection, we analyse rMMSE performances for sidelobe suppression of ground clutter targets. For this, we consider the same azimuth direction used in Figure 2.5, Panel(a) $\phi = 35°$. In Panel(b) of the same figure, we remark there is a strong ground target around 3.5 km. Thereby, we analyse here Elevation-Doppler map for that range position and azimuth direction. In Figure 4.4 are shown four rows and two columns of

results, wherefrom along rows SNR value is varying from low to high, and column one corresponds with 2D elevation-Doppler image plot for each beamforming method: FR, CP and rMMSE, respectively, and columns two corresponds with all three moments: M_0, M_2 and M_3, respectively.

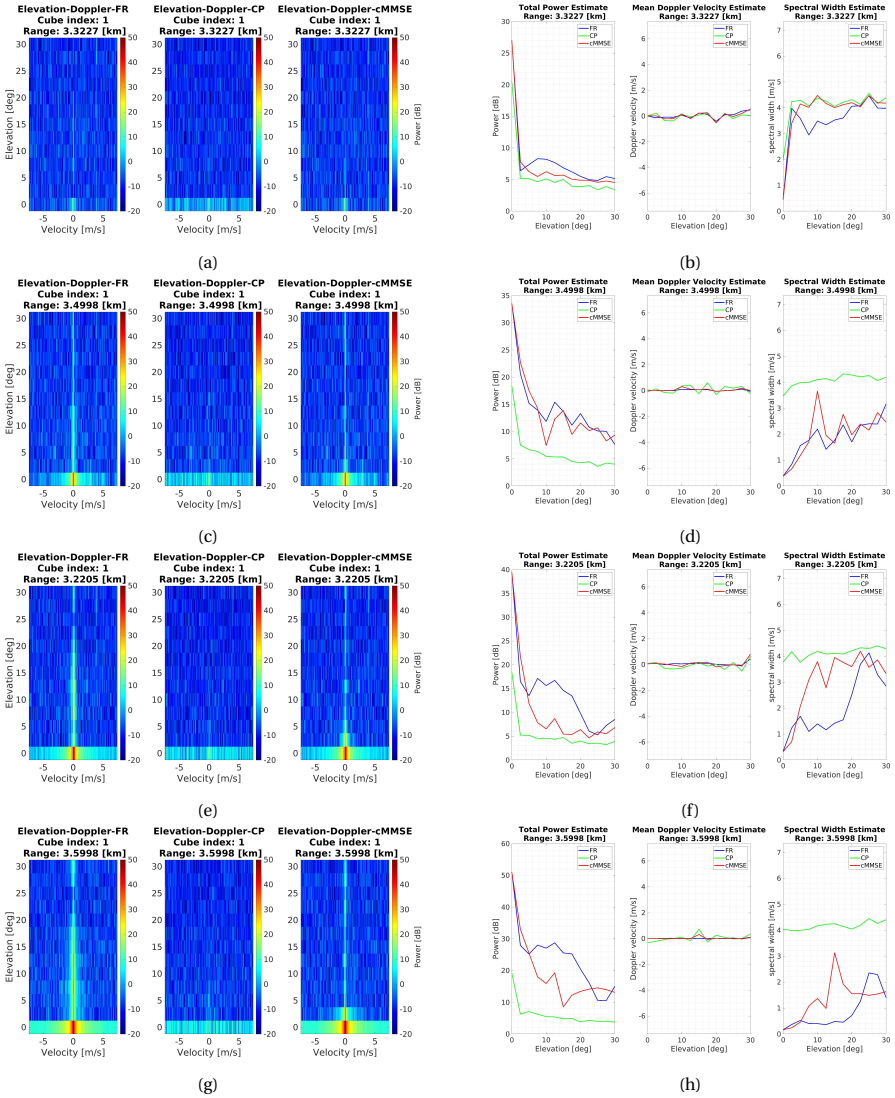

Figure 4.4: Examples of data results for sidelobes suppression performance analysis.

Based on results shown in Figure 4.4, we first remark that the CP method underestimates the total power for 0° elevation, but sidelobes are strongly suppressed. Based on Figure 2.6, Panel(b), we can estimate noise power value ($\frac{\sigma_n^2}{M}$) at 3.5 km, which is around -8

dB, thus we can compute expected noise floor level for total power using Eq. 3.23, and we obtain that $\sigma^2_{n_{in}} = 2.34dB$, for $N = 256$ and $dv = 0.0578$ m/s. We see that for total power, CP method obtains almost this value at higher elevation angles. Thus we can consider CP results as a benchmark in terms of sidelobe suppression. For cMMSE algorithm, we notice that the total power of the ground clutter is estimated without errors, with respect to total power estimated by FR, and that cMMSE is suppressing sidelobes to the higher elevation angles, converging to the CP result, but not in all situations. However, we notice that there are some unexpected results, in the second row, where we notice that cMMSE does not suppress sidelobes and provides close performance as FR. For M_1 estimation we notice that for this examples is constant: around zero. For M_2, on the other hand, we notice that is sidelobes are well suppressed, it has to converge to 4, which in the case of cMMSE, it happens only for the first and third row. Another unexpected result is for the fourth row, high elevations, range 13° to 30°, where cMMSE gives worse results than FR in terms of sidelobes suppression.

Based on the results for this subsection we can conclude that rMMSE perform suppressing the sidelobes for ground clutter, for the first row and third-row case, but seems to present unexpected results, as is the case for the third and fourth row.

4.4.2. SATURATION SUPPRESSION

In this subsection, we analyse the possibility to suppress saturation using adaptive beamforming algorithms. For this, we consider that saturation is coming from a ground object and that artefacts present at higher elevation angles are only sidelobes effect. For this we use data from the azimuth direction used in Figure 2.5, Panel(b) $\phi = 45°$, for the same range interval used for the previous study, 3 to 4 km, and we select only a representative result for our objective. We plot the elevation-Doppler map for all three beamforming methods and compare moments results in Figure 4.5.

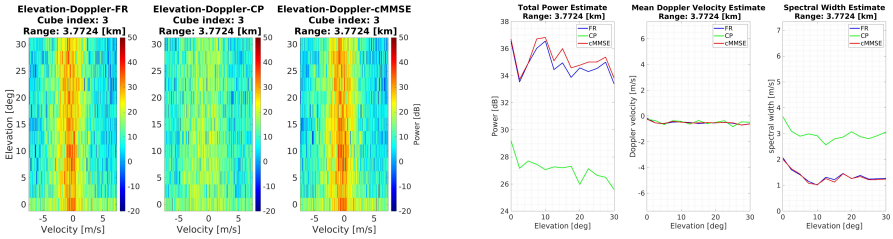

(a) (b)

Figure 4.5: Example of case when saturation is present in spectrum and adaptive beamforming is applied, CP and rMMSE.

Based on results from Figure 4.5, we notice that neither of the adaptive algorithms suppresses sidelobes from higher elevation angles. Even if in the case of CP total power is lower, it does not decrease under 25 dB, and the difference between CP and rMMSE/FR, is about 8 dB only. However, for CP saturation effect is much more spread in Doppler spectra, results that can be observed in Figure 4.5, Panel(b), for M_2, where CP is approaching the value of 4 for spectral width, which corresponds with noise. In this case,

cMMSE, does not provide higher improvement, compared with FR.

To conclude, based on the results obtained for saturated data, we understand that whenever is a weather target present in the spectrum, precipitation profiles are biased by the presence of this effect for all elevations, since its effect is present with almost the same power in all spectra, and adaptive beamforming methods is not a solution to filter this effect out. One more important result is that we notice that for this specific elevation-Doppler map, this saturation effect compresses around 0 m/s Doppler velocity with constant width of about 1.2 m/s, which represents a useful information if we decide to filter this out.

4.4.3. ELEVATION-DOPPLER RESULTS

Based on other subsections, *Sidelobes suppression* and *Saturation suppression*, we noticed that rMMSE works to suppress sidelobes of flutter echo, but we indeed proved, using an example, that when saturation happens, this affect all the antenna element receivers, thus is present for all elevations. However, we noticed that for the Doppler domain, this saturation is considered as being 0 m/s, which means is concentrated mostly at the centre of spectra. In this subsection, we analyse a situation that implies weather target presence in Doppler spectra. For this study, we focus on the performances of rMMSE to suppress clutter echo and on the differences between rMMSE and the other two methods: FR and CP, in terms of estimation accuracy of all three moments.

Thereby, Figure 4.6 shows results of elevation-Doppler map and moments estimation, for azimuth direction, $\phi = 35°$, with range within interval 10 to 11 km. For this, we pick up the most relevant result.

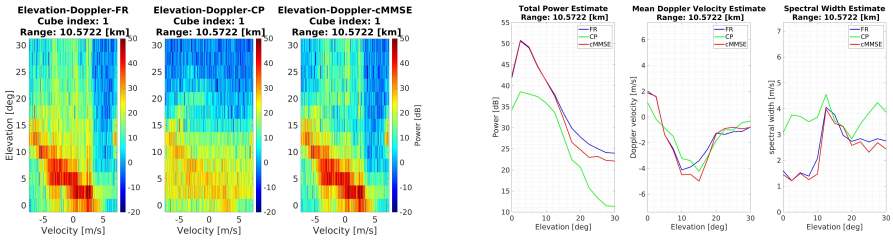

(a) (b)

Figure 4.6: Example of elevation-Doppler 2D image plot when weather target is present.

Based on the quantitative analysis, Figure 4.6, Panel(a) we do not remark much difference between cMMSE and FR. However, for cMMSE method, we observe that sidelobes are suppressed around the target, but performances of cMMSE converges to FR to the higher elevation angles. This result can also be checked based on the qualitative results, Panel(b), for total power, where sidelobes are suppressed by cMMSE, red line, by almost 3 dB, compared with FR, blue line. Due to this performance, we remark a more accurate estimation of M_1, if we compare cMMSE with CP, green line, within interval 14° to 20°. In terms of spectral width, we do not notice too much difference between cMMSE and FR, but we remark that within elevation interval 11° to 20°, cMMSE follows CP results with fewer errors, where FR is jumping around CP results.

To conclude with, this study shows us that indeed rMMSE algorithm improves the accuracy of precipitation profiles estimation if we compare it with both FR and CP, but also if we correlate that with qualitative results. Thus, due to the sidelobe suppression of about 3 dB, measured at 20° elevation for total power estimation result, Panel(b), we gain higher accuracy of estimation of about 2 m/s, within elevation interval 14° to 20°, measured for mean Doppler velocity estimation result in Panel(b). However, sidelobes effect for higher elevation angles, after 21°, rMMSE converges to FR, instead of following a decay pattern, as we notice in the case of CP. Nevertheless, high elevation sidelobes will not be an issue anymore when we filter out the area around the target, the operation described in Chapter 5.

4.4.4. RANGE-DOPPLER RESULTS

In this final subsection of the fourth section, we study the range-Doppler domain, which represents our domain of interest for the following processes, like noise clipping and errors correction. Thereby, we are interested to understand to what degree performances remarked in the elevation-Doppler domain are affecting the results in the range-Doppler domain.

For this study, we opt for the same azimuth angle, $\phi = 35°$, and for elevation angle of 12.5° and 17.5°. We chose only the most relevant results. By opting for same azimuth angle as for elevation-Doppler map study, Figure 4.6, we can correlate the results between that figure and Figure 4.7, shown in this subsection for range-Doppler map. This figure shows two sets of results, two rows and two columns, where the first row corresponds with 12.5° elevation and high SNR, and the second row with 17.5° and low SNR. For these results, we set dynamic power range to fix interval of $[-20 to 50]$ dB, for a more appropriate comparison. The first column shows range-Doppler map, and the second column shows all three moments computed over the range axis: [0.229; 14.971] km. Input parameters value are the same depicted in Table 4.6.

For this study, we focus on both the qualitative, first column and quantitative, second column results. Qualitative differences between rMMSE and FR method can be explained based on previous results. For instance, in Figure 4.7, Panel(c), around 10 km range, we can notice some important differences, which are expressed, from a quantitative point of view, in Panel(d), where total power estimation for cMMSE, red line, is about 5 dB lower than FR estimation, blue line. This phenomenon can be explained based on Figure 4.6, Panel(b), which is obtained for the same approximate range value of 10 km. In Panel(b) within interval 17° to 18° elevation we notice that sidelobes are suppressed by about 2 dB. Even if this is a small improvement in elevation-Doppler domain, for range-Doppler domain represent 5 dB.

Another advantage of sidelobes suppression using rMMSE, can be noticed for the first row of Figure 4.7, Panel(a), within range interval 11 to 14 [km], from 0 to 5 [m/s], where we can notice two different clusters for FR, but only one for cMMSE, as result of sidelobes suppression. From a quantitative point of view, this result can be noticed in Panel(b), for both M_1 and M_2, where in the mentioned interval for range [km], we notice that M_1 for FR is closer to zero than estimated one by cMMSE. In terms of M_2, the result for cMMSE is narrower in that range interval, than is for FR, with a difference of about 0.4 [m/s].

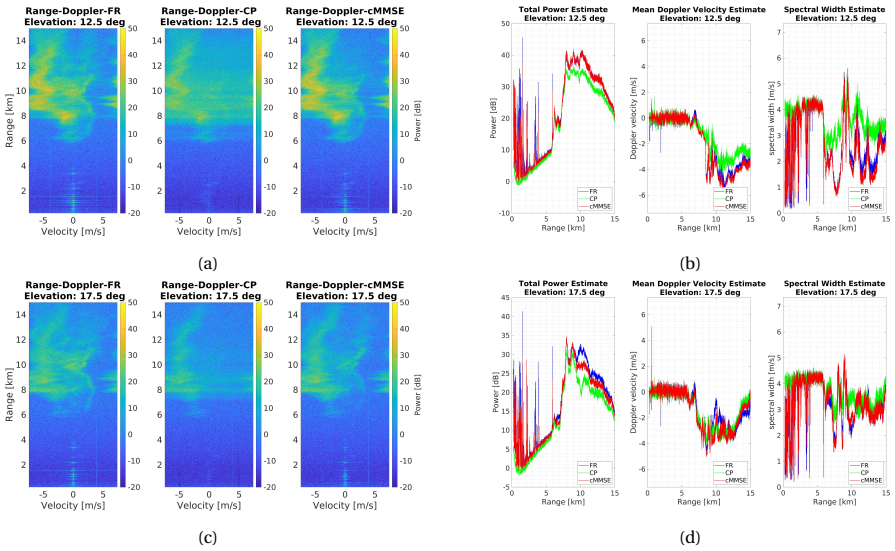

Figure 4.7: Example of range-Doppler 2D image plot when weather target is present. $\phi = 35°$

To conclude, in this subsection we analyzed the magnitude of differences between cMMSE and FR, when studied in range-Doppler map. We noticed that small estimation accuracy differences observed in the elevation-Doppler map, provides much larger differences in the range-Doppler map, where the most significant one is to avoid bimodality, this is the presence of two separated Doppler spectra distributions, with different mean Doppler velocities, which has as effect broader spectral width and biased mean Doppler velocity, which is estimated somewhere between distributions. For the observation we tried to relate both domains, elevation-Doppler and range-Doppler, which provides a stronger basis to our explanations.

4.5. CONCLUSIONS

In this chapter rMMSE beamforming algorithm performances for estimation accuracy of precipitation, profiles were studied. Analytical expressions were derived for the signal model, conditions that beamforming works, and for the most well-known receivers ZF, Wiener, and MF. Three different beamforming methods were studied: Fourier, Capon, and rMMSE, and their mathematical expressions were derived, too. rMMSE technique was explained based on Wiener receiver and Capon beamforming. An algorithm workflow for rMMSE was introduced. A numerical simulation was performed for all three studied methods. Based on qualitative and quantitative results rMMSE showed the best performances among other beamforming methods concerning performance criteria set for high estimation accuracy of precipitation profiles, 1) sidelobes suppression, 2) accurate estimation of amplitude and phase information, and 3) robustness to a limited number of Doppler pulses. Conclusions about the stability of rMMSE when noise variance is underestimated, respectively overestimated are drawn, when the range interval

of errors for noise variance estimation is from $-10[dB]$ to $10[dB]$.

Real data simulations were studied for the performances of each criterion mentioned above. Moreover, a study for the possibility to suppress high power reflectivity as an effect of receiver's saturation was carried out, assuming that for high elevations are present only sidelobes level of this effect. This study proved that this is not true and that this effect occurs for all elevation angles with about the same power level. However, for the suppression of sidelobes level due to the ground targets, rMMSE was compared with FR and showed higher performances, especially for Doppler weather spectra, where we concluded that using rMMSE, the presence of false weather targets due to the effect of sidelobes level can be avoided. This result brings high improvements for the estimation accuracy of precipitation profiles.

REFERENCES

[1] S. D. Blunt and S. Member, *Robust DOA Estimation : The Reiterative Superresolution (RISR) Algorithm,* IEEE Transactions on Aerospace and Electronic Systems **47**, 332 (2011).

[2] E. Yoshikawa, T. Ushio, Z. Kawasaki, S. Yoshida, T. Morimoto, F. Mizutani, and M. Wada, *Mmse beam forming on fast-scanning phased array weather radar,* IEEE Transactions on Geoscience and Remote Sensing **51**, 3077 (2013).

[3] H. Kikuchi, E. Yoshikawa, and T. Ushio, *Application of Adaptive Digital Beamforming to Osaka University Phased Array Weather Radar,* IEEE Transactions on Geoscience and Remote Sensing **55**, 3875 (2017).

5

TARGET MASK FOR ESTIMATION ACCURACY GAIN OF PRECIPITATION PROFILES

An adaptive approach to compute target mask is developed in this chapter based upon morphological filtering techniques, to improve the estimation accuracy for precipitation profiles (total power reflectivity, mean Doppler velocity, and Doppler spectral width). A target mask is a 2D binary image where ones and zeros represent if the target is present or absent at (x, y) coordinates of the pixel. For this, a detection test is employed where test statistics and a threshold are necessary. In our case, we propose a simple solution where the power of spectral components is compared with a priori estimated noise power profile, while the trade-off between false alarms and sensitivity, triggered by the threshold value, is solved using morphological filtering operations. This family of filters uses set theory and provides two mechanisms known as erosion and dilation that work based on a small set, called structural element (SE). Employing these mechanism image objects can shrink or extend up to area values dependent on the SE dimension. If we consider that weather targets and false alarms are set of pixels in an image, which can create image objects, then we assume that weather objects are larger than false alarm objects, for white noise. Hence, the latter objects can be eliminated with the right choice for the SE dimension. Thereby, in this chapter, we propose an adaptive algorithm for the SE dimension, tuned to the criteria of the minimum false alarm error and the highest estimation accuracy for precipitation profiles. Herein we call this Adaptive Morphological Filtering (AMF) algorithm. Benefits of this algorithm include robustness to elevated noise-floor level up to 10 dB from the threshold value, as can occur for saturation phenomenon, control of details for weather target edges while maintaining high estimation accuracy of precipitation profiles, and the possibility to suppress the effects of sidelobes when their level is comparable with threshold level. From an implementation perspective, AMF is an iterative algorithm that compares the squared difference of each two successive RMSE values with an experimentally verified threshold. This method proves stability in terms of estimation accuracy, for a large range

of SNR values from 10 to 40 dB and for a large range of false alarm rates for about 100% *to* 0%.

5.1. INTRODUCTION

GENERATING a 2D target mask means detecting for each pixel whether a target is present or not. For weather applications a correct detection of target objects determines a higher estimation accuracy of Doppler spectrum moments: total power reflectivity, mean Doppler velocity, and spectral width. This implies that processed results are more reliable and easier to explain the weather phenomenon that is going on while radar is scanning the sky. Because of the similar statistics between noise and weather targets, the decision process becomes more complicated. Thus, in this project, we consider that any value above the noise floor is a target, either point or extended target. This is

$$H_0 : (S_k + N) < N \cdot Th \tag{5.1}$$

$$H_1 : (S_k + N) >= N \cdot Th, \tag{5.2}$$

where S_k is frequency-dependent signal power density, N is white noise power per discrete frequency, and Th is threshold value. H_1 represent *alternative hypothesis*, that target is present and H_0 is *null hypothesis* that target is absent. Henceforth, the binary image obtained after detection is called *raw binary image*.

For the estimation of floor noise level, we propose to use noise data, this is data recorded with the transmitter off and to estimate averaged noise power profiles out of it. In Chapter 3 we verified that this noise power profile is an accurate estimate of noise floor level. However, this simple method raises a trade-off between false alarms and the sensitivity of weather targets. The smaller the threshold the higher the sensitivity but also false-alarms-errors, and vice versa. In this chapter, an adaptive algorithm based on morphological operations is proposed. This algorithm is supposed to compensate for the dynamic values of false alarm rate in order to clean the Doppler map image out of false alarm errors and to estimate, with high accuracy, precipitation profiles (weather object). This family of filters uses mathematical set theory, where image objects are considered a set of points in Z^2 for binary image characterized by (x, y) coordinates. With a small set, called structural element (SE) and two main operations, objects from the image can shrink or extend. SE can be defined in terms of shape and dimension, and morphological operations are erosion and dilation. For instance, an object smaller than SE can be eliminated by employing an erosion operation. Assuming that atmospheric objects are much larger than false alarm objects, we can use this technique for the detection of weather objects with a low false alarm error. Because false alarm objects dimension is varying we estimate it by trying a range of SE dimensions. When the right dimension has been found, the iterative algorithm stops. This is an adaptive algorithm and we call it here *Adaptive Morphological Filtering* (AMF).

Thereby, in this chapter, we develop an iterative adaptive algorithm to find the dimension of SE that for opening and dilation morphological operations can the false alarm errors, while weather target is prevented from filtering and the pixels at the edges are restored. For this, we develop a hypothesis test and find an experimental threshold

value. Hence, the hypothesis test is the square of the difference between successive Root Mean Square Error (RMSE) parameters values, where RMSE is computed between an estimated probability density function and a *U-quadratic function*, which is a general well known probability distribution function. The former is estimated based on *pixels densities* computed in a fixed-size sliding window, this is the total number of pixels of one divided by the area of the window, where values are between 0 and 1. Hypothesis testing function:

$$H_1 : (RMSE(i) - RMSE(i-1))^2 <= th_{AMF} \tag{5.3}$$
$$H_0 : (RMSE(i) - RMSE(i-1))^2 > th_{AMF}, \tag{5.4}$$

where i is the i^{th} iteration, and th_{AMF}, represent experimentally found threshold value. H_1 represent *alternative hypothesis*, when the rate of false alarm converges to zero, and H_0 is *null hypothesis* when there are false alarm points present in the image. U-quadratic density function is defined by $f(x)$:

$$f(x) = \alpha(x-\beta),$$
$$\alpha = \frac{12}{(b-a)^3},$$
$$\beta = \frac{b+a}{2},$$

where interval $[a, b]$ is the same as interval for pixels densities, $[0, 1]$.

This chapter is organized as follows. **Section 2** contains four subsections wherein first introduces the theory for operations used in morphological filtering, erosion, dilation but also *opening and closing*, followed by the second subsection that introduces the literature review to motivate the novelty and sources of inspiration. The third one continues with a brief explanation of the mathematical framework meant to describe morphological operations used in our algorithm, based on the same approach described in [1]. The last subsection includes explanations of the choice for hypothesis test function, supported by simulated results. Moreover, we propose a threshold value and some algorithm settings based on experimental results. **Section 3** is made of two subsections and introduces simulator parameters and estimation errors for precipitation profiles due to the presence of noise. **Section 4** introduces the performances of the proposed algorithm in terms of estimation accuracy, wherein first subsection performances are tested for the ideal case when moments' ground truth values are known, while in the second subsection performances are analyzed for the AMF algorithm. **Section 5** introduces results of AMF performances for MAX3D radar data, wherein two cases are analyzed when the threshold is 0 dB, 10 dB respectively. Moreover, an iterative algorithm to solve the Doppler aliasing phenomenon is proposed and tested based on real data simulation. This chapter ends up with a **Conclusions** section.

5.2. METHODOLOGY

5.2.1. MORPHOLOGICAL IMAGE PROCESSING

The name for this family of filters denotes a branch of biology that deals with the form and structure of animals and plants, [2]. The same word is used here for *mathematical morphology* as a tool for extracting specific objects from the image that we are interested in, for instance, whether target. This filter uses set theory and provides two mechanisms, known as *erosion* and *dilation*, that are used to shrink and expand respectively, the objects within an image. Image objects represent a set in mathematical morphology. In binary images, a set belongs to 2D integer space, Z^2, where each element of the set represents (x, y) coordinates of a pixel in the image. Before introducing erosion and dilation operations, we explain first the concept of set *reflection* and *translation*. The reflection of a set $\hat{B}$, is defined as, [2]:

$$\hat{B} = \{w | w = -b, for b \in B\}, \tag{5.5}$$

which means that if B is the set of pixels representing an object in an image, whose coordinates are (x, y), then $\hat{B}$ is the set of pixels with coordinates $(-x, -y)$.

Translation of a set B, by point $z = (z_1, z_2)$, denoted $(B)_z$, is defined as, [2]:

$$(B)_z = \{c | c = b + z, for b \in B\}, \tag{5.6}$$

which means that if B is the set of pixels representing an object in an image, whose coordinates are (x, y), then for $(B)_z$ they are replaced by $(x + z_1, y + z_2)$.

Set reflection and translation are used to describe the erosion and dilation operation that uses structural elements (SEs): small set used to probe the image of interest, that can have different shapes: square, line, diamond, circle, random, etc., and different dimension. One rule for SE is that it requires to be rectangular arrays, this means to add a minimum number of background elements, i.e. zero pixels. Let us consider $\boldsymbol{A}$, the raw binary image.

EROSION

With A and B as sets in Z^2, the erosion of A by B, denoted $A \ominus B$, is defined as

$$A \ominus B = \{z | (B)_z \subseteq A\}, \tag{5.7}$$

where set A represents a binary image as a result of the detection process and B the SE. This equation means that the set of all points z is the result of set B contained by set A at positions z. In other words, if B is larger than an object present in image A, then that object is cleaned out, otherwise, if B is smaller, then only the contour of that object is affected, and as results object shrinks. If holes are present in object A, then they are enlarged after erosion.

DILATION

With A and B sets in Z^2, the dilation of A by B denoted $A \oplus B$, is defined as

$$A \oplus B = \{z | (\hat{B})_z \cap A \neq \emptyset\} \tag{5.8}$$

Hence, the dilation of A by B is the set of all points z such that B reflected about its origin and translated over A by z, intersect with A in at least one single point. This means that the object's contour is extended and object holes are filled if the SE dimension is larger than the hole.

OPENING AND CLOSING

Opening and closing are two other morphological operations, where both consist in a combination of erosion and dilation, but in a different sequence. *Opening* is a combination of erosion followed by dilation which in general smoothens the contour of objects, breaks narrow holes, and fills thin ones. *Closing* also smoothes the contour of objects, but different than the opening, it tends to fill small holes and gaps in contour, [2].

5.2.2. LITERATURE REVIEW AND NOVELTY

Morphological filtering method proves to provide promising results for different approaches enumerated here as, adaptive scenario for weather applications, [3], optimal scenario for medical imaging applications, [4], and iterative detection scenario, [1]. The last article provides a comprehensive derivation for the mathematical framework for error correction using morphological filtering. Here, the set of false alarms and missed detection are separated sets that have to be estimated individually, such that the set of the true image can be estimated by using morphological operation. Based on this, the choice of operations (opening followed by dilation) and the dimension of SE are strongly motivated.

On the one hand, in [4], authors use CNR (Contrast to Noise Ratio) to find the optimal size of the SE, while in [1] this is done using a priori knowledge regarding the statistics of the target and noise, which is more convenient for the radar data type. Regarding, [3] they use a sliding fixed-size window to estimate the density of pixels of one at each position of this window and based on the value of density they apply either dilation, for target, or erosion for noise, which provides an adaptive algorithm kind, while their choice for SE's size is fixed. Our method combines the mathematical framework provided in [1] and adaptive mechanism for the choice of the best dimension of SE, wherein in their case they can find the optimal dimension since they have a priori knowledge about probability density function of noise and target. Because in our case non-parametric density and U-quadratic density are not perfectly matching we use as metric squared of the difference between each successive RMSE value, computed between these two density functions. When the number of false alarms converges to zero, this difference converges to zero as well. Thus, we use a small threshold value, that in the last subsection of this section we experimentally demonstrated that 0.001 ($\Delta RMSE$) is a good approximation of this threshold. The choice for space of density of pixels of one per fixed-size window to compute parametric density function and the choice of U-quadratic density function as parametric function represents the novelty for our method.

5.2.3. MATHEMATICAL FRAMEWORK FOR MORPHOLOGICAL OPERATIONS

Raw binary image is the result after detection process: $\{0;1\}$, performed for each instantaneous power of the signal plus noise: $P_k^{(i)} = (S_k^{(i)} + N^{(i)})$, in which the signal, $S_k^{(i)}$ is frequency dependent and noise is white. Notations for k and i represent k^{th} Doppler frequency and i^{th} range bin. For noise we consider that noise power is range depen-

dent, but constant over frequency spectra. Thus, detection process can be formulated as:

$$H_0 : (S_k^{(i)} + N^{(i)}) < N^{(i)} \cdot Th, \tag{5.9}$$

$$H_1 : (S_k^{(i)} + N^{(i)}) >= N^{(i)} \cdot Th, \tag{5.10}$$

where H_1 represents *alternative hypothesis*, that target is present and H_0 is *null hypothesis* that target is absent.

If the process to obtain raw binary image has been defined, next the mathematical morphology can be introduced. For this binary image is considered as a set of points, characterized by (x, y) coordinates. Thereby, range binary image is denoted henceforth with $\boldsymbol{B}^C$ and *target mask* by $\hat{\boldsymbol{B}}$. Binary image which contains the set of points that corresponds with weather target only is denoted with **B** and sets that contain false alarm points and miss detection ones are denoted by, $\boldsymbol{B}_{FA}$ and $\boldsymbol{B}_{MD}$, respectively. This can be mathematically expressed as follows,[1]:

$$\boldsymbol{B}^C = \boldsymbol{B} + \boldsymbol{B}_{FA} - \boldsymbol{B}_{MD} \tag{5.11}$$

In order to estimate $\boldsymbol{B}$, we are using the morphological erosion and dilation operations $\boldsymbol{B} \ominus E$ and $\boldsymbol{B} \oplus E$, respectively, where E in this case is the SE. In order to eliminate $\boldsymbol{B}_{FA}$ an opening operation is performed, this is defined as: $(\boldsymbol{B} \ominus E) \oplus E$, erosion followed by dilation. In order to add $\boldsymbol{B}_{MD}$ a dilation is employed. The reason for choice of an opening operation is that erosion operation eliminates false alarm objects, and dilation fills back gaps created by erosion and smoothes target's contour. Mathematical expression for this is the following:

$$\hat{\boldsymbol{B}} = \boldsymbol{B}^C - \hat{\boldsymbol{B}}_{FA} + \hat{\boldsymbol{B}}_{MD}. \tag{5.12}$$

We denote by E_{FA} the SE that eliminates false alarms and by E_{MD}, the SE used to correct missed detection errors. Operations used for each SE are expressed in next equations,[1]:

$$\boldsymbol{B}^C \circ E_{FA} = (\boldsymbol{B}^C \ominus E_{FA}) \oplus E_{FA} \tag{5.13}$$

$$\approx \boldsymbol{B}^C - \boldsymbol{B}_{FA} \tag{5.14}$$

$$(\boldsymbol{B}^C - \boldsymbol{B}_{FA}) \oplus E_{MD} \approx \boldsymbol{B} = \hat{\boldsymbol{B}} \tag{5.15}$$

For the sake of using morphology and to describe the characteristics of SE dimension, the set of false alarms points, $\boldsymbol{B}_{FA}$ and the set of target objects, $\boldsymbol{B}$ can be described as sum of image objects:

$$\boldsymbol{B}_{FA} = \sum_{i=1}^{N} O_{FA}^i \tag{5.16}$$

$$\boldsymbol{B} = \sum_{i=1}^{N} O_W^i \tag{5.17}$$

Thus, the number of false alarms points gathered in the same close area make an object image. Same for the case of weather objects. Using this insight and Eq. 5.13, and Eq. 5.16 the rule for the SE dimension when erosion operation is employed, can be determined. The effect for this rule has to clean all the false alarms object, but prevent filtering of weather object. Hence, based on properties of erosion, SE dimension has to be larger than the largest false alarm object, and smaller than the smallest weather object. Using this result, our assumption that morphological operations can be employed for the detection of weather targets is mathematically proven, based on the set theory and characteristics of erosion operation. In [1] dimension of E_{MD} is considered fixed and is 1. The authors considered that is sufficient to encompass the target pixels located at the edges of the object. However, in our case, we observed that one single pixel is not enough to accurately estimate the correct values of the edges of the target object. Therefore, in the second subsection of Section 4, a discussion is carried out for the choice of the best solution. Based on that result, for our algorithm we propose that E_{MD} to be adaptive and $E_{MD} = E_{FA}$.

5.2.4. ITERATIVE ALGORITHM SETUP

The iterative algorithm for AMF has been initialized for SE dimension equal to one and the raw binary image, obtained after target detection operation. For every new iteration, the SE dimension is incremented by one and the target mask is computed using the new incremented value of SE. The iterative algorithm stops when the alternative hypothesis, H_1 is true. Hypothesis testing function is:

$$H_1 : (RMSE(i) - RMSE(i-1))^2 <= th_{AMF} \tag{5.18}$$

$$H_0 : (RMSE(i) - RMSE(i-1))^2 > th_{AMF}, \tag{5.19}$$

where i is the i^{th} iteration, and th_{AMF}, represent experimentally found threshold value. H_1 represent *alternative hypothesis*, when SE dimension is larger or equal with the largest false alarm object and H_0 is *null hypothesis* when SE dimension is smaller than the largest false alarm object.

As already mentioned in introduction, RMSE is computed between estimated density function using pixels density values and *U-quadratic* density function, Figure 5.1, Panel(b) and (d), blue line colour for the former and orange line colour for the latter. Panel(b) shows an example after the second iteration and Panel(d) after the fifth iteration when false alarm error starts to converges to zero. For the estimate of the probability density function, we use a *Kernel estimator*, with Gaussian kernel and adaptive width.

Based on results shown in Panel(b) and (d) we notice that when false alarms objects are cleaned values at the center of the estimated probability density function approaches zero. If the SE dimension increases more than the value necessary to reduce false alarm error to zero, this interval of (0.4, 0.6) stays constant, and only the amplitude of the edges changes slowly which provides a small difference between successive RMSE values. This result is shown in Figure 5.1 Panel(e), depicted for dimension of SE larger than four.

Pseudo-code for the iterative algorithm is introduced in the following lines:

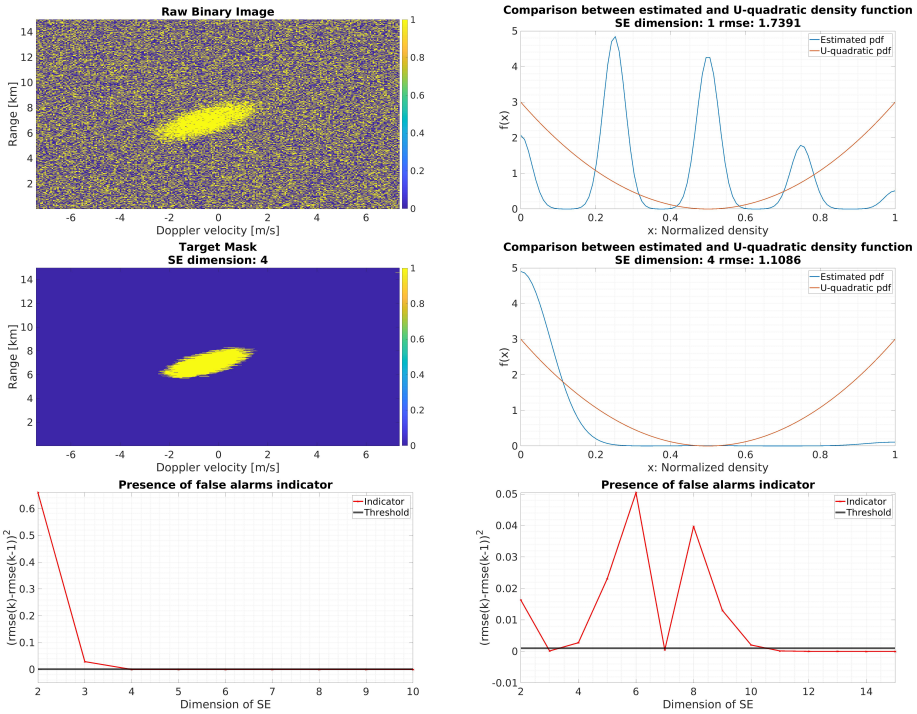

Figure 5.1: Examples of raw binary image and target mask, Panel(a) and (c), respectively and estimated distribution function for pixels density that correspond with each image, Panel(b) and (d). This density is depicted with blue line color, and probability density function with orange line color is U-quadratic function. Panel(e) shows squared difference between $RMSE^{(i)}$ and $RMSE^{(i-1)}$ values: $\Delta RMSE^{(i)} = (RMSE^{(i)} - RMSE^{(i-1)})^2$ where $RMSE^{(i)}$ is computed between estimated density function and U-quadratic function at each value of $dim_{SE}^{(i)}$. Panel(e) shows $\Delta RMSE^{(i)}$, where $i = [1,10]$. Results computed for SNR = 20 dB and threshold = 0 dB, where for Panel (f), theshold = -10 dB. Panel (f) shows overshooting event.

INITIALIZATION

1. Threshold variable for minimum false alarm error initiated by $t_{AMF} = 0.001$
2. Overshooting variable initiated by zero, $u(0) = 0$;
3. Admitted overshooting times variable initiated by three, $counter = 3$;
4. *Raw Binary Image* (RWB) is computed based on detection process described in Eq.5.9;
5. Algorithm is initialized for SE dimension equal one, $dim_{SE}^{0} = 1$;
   WHILE LOOP
6. Opening and dilation operations are applied over RWB using $dim_{SE}^{(i)}$;

7. Pixels density, $\delta^{(i)}$ is computed for the minimum possible window, in our case $win_{size} = 2 \times 2$;
8. $RMSE^{(i)} = \sqrt{\frac{1}{n}\sum_x (f_e(x)^{(i)} - f_U(x))^2}$ is computed
9. if i > 1, then $\Delta RMSE^{(i)} = (RMSE(i) - RMSE(i-1))^2$
   (a) if $H_1^{(i)}$ true and $H_1^{(i-1)}$ true as well
      i. $u(i) = u(i-1) + 1$;
      ii. if $u(i) > counter$,
         A. Return $dim_{SE}^{(out)} = dim_{SE}^{(i)} - (counter - 1)$;
         BREAK
      iii. else
      iv. $u(i) = 0$
10. $i = i + 1$
11. $dim_{SE}^{(i)} = dim_{SE}^{(i-1)} + 1$

Figure 5.1, Panel(f) shows an overshooting example, where the event happens two times before converging to zero. This result is obtained for a false alarm rate of about 100%. Thus, this overshooting condition, shown in the pseudo-code algorithm is meant to avoid this special event. In our case, we use $counter = 3$, which means that the algorithm breaks only in the case when more than three consecutive values are smaller than th_{AMF}.

Parameters settings for simulation results provided in Figure 5.1 are provided in Table 5.1. For simplicity, henceforth false alarm rate is quantified by threshold value used for detection of target, denoted Th. Hence, $Th = -10dB$ means false alarm rate of about 100% and $Th = +10dB$ means false alarm rate of about 0%. $Th = -10dB$ represent the event when noise floor has higher power than a priori noise power profile, as can occur for saturation phenomenon.

Parameter	Value
SNR	20 dB
th_{AMF}	0.001
Th	0 dB and -10 dB
counter	3

Table 5.1: Parameters settings for simulation results shown in Figure 5.1. Description of SNR formula is provided in Eq. 5.20, th_{AMF} represent threshold value to stop the iterative process and is compared with a square difference of two successive RMSE values, $\Delta RMSE^{(i)}$, Th represent threshold value for target detection, and apart Panel(f), where Th = 10 dB, rest of the results are obtained for Th = 0 dB. Th = -10 dB is used to characterize false alarm rate of about 100%.

In order to demonstrate performances for the choice of initialization variable $th_{AMF} =$ 0.001 and $counter = 3$, Table 5.2 shows ground truth values of SE dimension for each

moment compared with estimated ones, when false alarm rate varies within interval (100%, 0%), that is $Th = -10, 0, +10$ dB. Moreover, this experiment is performed for seven discrete values of SNR, within interval [10, 40] dB with a step of 5 dB.

	Th = - 10 dB				**Th = 0 dB**				**Th = 10 dB**			
SNR [dB]	$SE_{dim}(M0)$	$SE_{dim}(M1)$	$SE_{dim}(M2)$	$\hat{SE}_{dim}$	$SE_{dim}(M0)$	$SE_{dim}(M1)$	$SE_{dim}(M2)$	$\hat{SE}_{dim}$	$SE_{dim}(M0)$	$SE_{dim}(M1)$	$SE_{dim}(M2)$	$\hat{SE}_{dim}$
10	11	11	11	9	3	3	4	4	1	1	1	2
15	12	11	12	9	3	3	4	4	1	1	1	2
20	12	11	12	10	4	3	4	4	1	1	1	2
25	12	11	11	10	4	3	4	4	1	1	1	2
30	11	10	13	10	4	3	4	4	1	1	1	2
35	11	11	12	9	4	3	4	4	1	1	1	2
40	12	12	12	8	4	3	4	4	1	1	1	2

Table 5.2: AMF performances as comparison between estimated dimension of SE, $\hat{SE}_{dim}$ and ground truth one computed for each Doppler moment: $SE_{dim}(M0)$, $SE_{dim}(M1)$ and $SE_{dim}(M2)$. Performance analysis is carried out for different SNR values, SNR = [10, 40] dB, with a step of 5 dB, and different threshold values, $Th = -10, 0, 10$ dB.

Ground truth values for SE dimension are obtained here employing RMSE for the values of each moment, when $dim_{SE} = [1, 15]$, with step one. Index position of minimum RMSE value indicates ground truth for SE dimension. Here is important to mention that for 2D areas where an object is missing, moments values are initialized by zero. This rule applies only to this simulation, otherwise for the rest of the chapter values are initialized with a number in Matlab wich is NaN (Not a Number).

Based on the results shown in Table 5.2, we notice that AMF performance for estimation of SE dimension is independent of SNR, but is dependent on the threshold value. The highest error of estimation for SE dimension is of 4, for $Th = -10dB$ and SNR = 40 dB. Note that for our algorithm, estimation criteria for dim_SE estimation is computed as a function of the error of false alarm within the image, which provides one scalar value of dim_{SE} for all three moments.

5.3. NUMERICAL SIMULATION

This section introduces background information about simulator and developed metrics, *estimation error* and *estimation accuracy* used to characterize following results.

5.3.1. SIMULATOR PARAMETERS

For numerical simulation we use *Weather Radar Signal Simulator* developed in chapter 3. For this four input vector variable are of interest: $\boldsymbol{M}_0$, $\boldsymbol{M}_1$, $\boldsymbol{M}_2$ and noise variance profile.

First, $\boldsymbol{M}_0$ array is generated as a Gaussian shape, for what we have to specify SNR, the position of maximum power, this is with respect to range axis, and width of the weather target along the range axis. The SNR in this case provides the maximum power, this is $max(\boldsymbol{M_0})$, and has the following definition:

$$SNR = \frac{max(\boldsymbol{M_0})}{\boldsymbol{\sigma_n^2}(k_{max})} \tag{5.20}$$

where $\boldsymbol{\sigma_n^2}(k_{max})$ represents noise variance at the k^{th} range bin that corresponds with $max(\boldsymbol{M_0})$. Hence, for a given SNR value and a priori averaged noise power profile, we

first obtain $max(\boldsymbol{M_0})$. Output result for $\boldsymbol{M_0}$ is shown in Fig. 5.2(b). Input parameter values used to generate $max(\boldsymbol{M_0})$ are shown in Table 5.3. For SNR = 30 dB results that $max(\boldsymbol{M_0})$ = 28.23 dB.

Parameter	Value
μ_{range}	7 km
σ_{M_0}	0.5 km
SNR	30 dB
$\sigma_n^2(k_{max})$	-1.768 dB

Table 5.3: Input values used to simulate vector $\boldsymbol{M_0}$

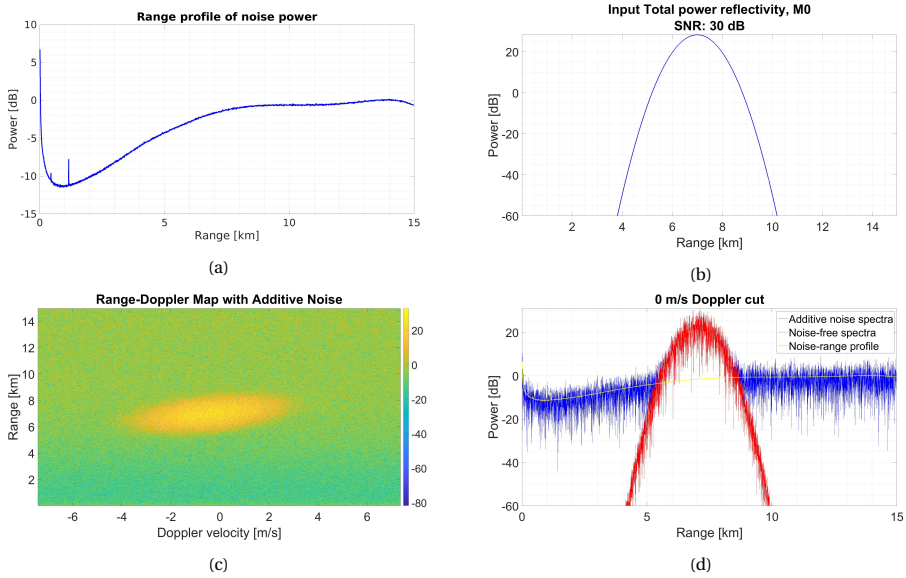

Figure 5.2: Example of simulator components, used to analyse performances of target mask method. Range-Doppler map, Panel(c) is generated based on input $\boldsymbol{M_0}$ array, Panel(b), $\boldsymbol{M_1}$ and $\boldsymbol{M_2}$, where similar trends are shown in Fig. 3.1, but for different values, and range profile of noise power, Panel(a). In Panel(d) is shown a range profile for 0 m/s Doppler cut, for both additive noise and noise-free Doppler spectra, with blue line colour and red line colour respectively.

Second , $\boldsymbol{M_1}$ and $\boldsymbol{M_2}$ are necessary in order to generate 2D range-Doppler map. Hence, for $\boldsymbol{M_1}$ we consider that maximum unambiguous velocity, $v_{max} = 7.39 m/s$, has the same value as the one derived from parameters of the radar. In this simulation $\boldsymbol{M_1}$ follows a monotonically increasing trend with respect to range axis, within interval $[-6.89, 6.89]$ m/s. For $\boldsymbol{M_2}$ we consider it fixed for all range bins, $M_2 = 1 m/s$. Number of range bins used for this simulation is 6592.

Thus, Figure 5.2(c) shows the 2D range-Doppler map with additive noise. Note that the power of noise is increasing proportionally with range value, as it is shown in Fig.5.2(a). Figure 5.2(d) shows the range profile for Doppler cut 0 [m/s], where both noise and

noise-free profiles are included, with a blue color line and the red color line, respectively. Moreover, a priori noise power profile is included with a yellow color line.

Ground truth for this chapter is computed for noise-free Doppler spectra. However, for this, we have to compute the target mask as well. In this case threshold value is zero and morphological operations imply a simple dilation with $dim_S E = 2 \times 2$ square shape, to solve missed detection errors. The reason why the threshold value is zero, in this case, is because we are interested in all targets above the noise floor level. Range Doppler map for ground truth is shown in Figure 5.3.

5.3.2. ESTIMATION ERRORS AS EFFECT OF ADDITIVE NOISE

To calculate the importance of the target mask we have to introduce two metrics. The first one is *estimation errors* and is directly related to the errors between estimated moments and ground truth moments values, and the second one is *estimation accuracy* and represents averaged difference between estimation errors. The latter is used to determine, for instance, improvement of moments estimation accuracy before and after target mask. Mathematical formulation and interpretation of these metrics are introduced in the following lines.

A. ESTIMATION ERRORS

Estimation errors represent the error between estimated moments and ground truth moments. This is computed as follows:

$$\boldsymbol{e}_i = log_{10}\sqrt{(\boldsymbol{M}_{\boldsymbol{i_{gt}}} - \hat{\boldsymbol{M}}_{\boldsymbol{i}})^2} \tag{5.21}$$

where vector $\boldsymbol{e}_i$ represent the error for each moment, $i = 0, 1, 2$. Vector $\boldsymbol{M}_{\boldsymbol{i_{gt}}}$ represent ground truth moment values and vector $\hat{\boldsymbol{M}}_{\boldsymbol{i}}$ represents estimated moment values.

This unit is represented on a logarithmic scale. Hence, if the error is zero this value converges to $-\infty$. Some references are provided in order to understand these results shown on a logarithmic scale:

1. Zero error means that there is a difference of one decimal between estimated and ground-truth moments values;
2. Unity error means that there is a difference of tens decimals;
3. For error below zero, any error increasing with one negative unit means tenths, hundredths, etc.;
4. For error converging to $-\infty$ means zero error at all.

B. ESTIMATION ACCURACY

Estimation accuracy represent averaged difference between relative estimation errors, $\boldsymbol{e}_i$ and estimation errors, $\tilde{\boldsymbol{e}}_i$. This is defined as follows:

$$\overline{e_{A_i}} = \frac{\boldsymbol{e}_i - \tilde{\boldsymbol{e}}_i}{N} \tag{5.22}$$

, where N is the number of elements for the range profile. In our case, $\boldsymbol{e}_i$ is defined as estimation errors between moments estimated before target mask and ground truth

moments. The reason why this difference is not represented in absolute values is that both $\boldsymbol{e}_i$ and $\tilde{\boldsymbol{e}}_i$ are in logarithmic scale.

Some references are provided as well in order to understand the meaning of this metric:

1. Zero estimation accuracy means that applied target mask does not improve estimation errors;

2. Positive infinite value means that $\tilde{\boldsymbol{e}}_i = -\inf$ which means zero estimation errors;

3. Positive unity estimation accuracy means that estimation errors were improved in average by one decimal;

4. Negative unity estimation accuracy means that estimation errors are worse after the target mask has been applied than before.

After introduction of *estimation error* metric, a study is carried out based on comparison between raw estimated moments and ground truth moments. Figure 5.3, Panel(d) shows quantitative result of estimation errors for two SNR values, that is $SNR = 20; 30$ dB. Dashed lines are for SNR = 30 dB, and pointed lines are for SNR = 20 dB, where estimation errors for M_0, M_1 and M_2 are depicted with black, blue and red color line, respectively. Figure 5.3, Panel(b) shows raw and ground truth moments results for SNR = 30 dB, blue color line and orange color line, respectively.

Hence, based on results shown in Panel(d) we first remark that estimation errors are inversely proportional with the SNR, with fewer errors for high SNR values. First, we analyze estimation errors at the edges of the target. For SNR = 30 dB results, we notice that the most relevant errors, above -1, are for intervals: [5.2;5.6] km, and [8.3;8.7] km. For this, estimation errors intervals are $[-1;-0.4][log_{10}]$ for M_1 and M_2 and $[-0.2;0][log_{10}]$ for M_0. In other words, this means that we have errors of tenths $(-1[log_{10}])$ to ones $(0[log_{10}])$ for all three moments. Using Panel(b) and Panel(c) results, the width profile of the target is getting broader at the edges for the results presented for raw data, than for ground truth data.

Second, we notice that errors for M_1 and M_2 converge to zero for the peak, but for M_0 increases up to $0.6[log_{10}]$, which means almost by ten times. Therefore, based on these results we conclude that for M_1 and M_2, the most relevant errors happen at the edges perpendicular with 0 [m/s] Doppler line, where for M_0 are increasing for the edges parallel with 0 [m/s] Doppler line and. We consider that these results motivate the necessity of a target mask algorithm.

5.4. ALGORITHM PERFORMANCES

This section includes two main subjects. First, that there is one single value for dim_{SE} that provides maximum estimation accuracy, and second, what are the maximum values of estimation accuracy for different rates of false alarm. Input parameters for simulation results are the same as those introduced in the previous section.

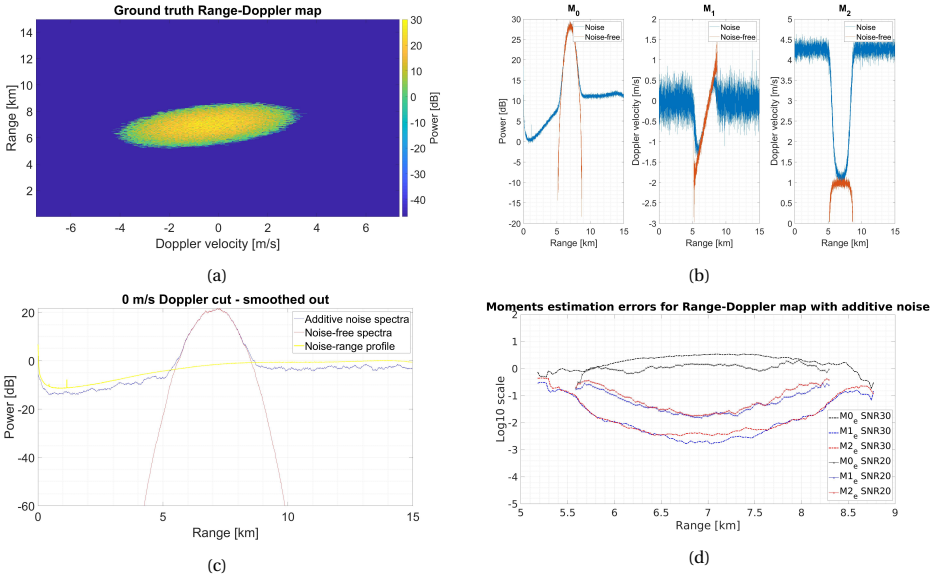

Figure 5.3: Simulation of moments estimation error for two SNR values, that is $SNR = 20;30$ dB, shown in Panel(d). Dashed lines are for SNR = 30 dB, and pointed lines are for SNR = 20 dB, where estimation errors for M_0, M_1 and M_2 are depicted with black, blue and red color line, respectively. Panel(b) shows raw moments values, blue color line and ground truth moments, orange color line. Panel(c) is the smoothed version of the range profile cut at 0 m/s Doppler velocity. Panel(a) shows the 2D range-Doppler map for ground truth after the target mask is applied.

5.4.1. NUMERICAL SIMULATION

Figure 5.4 shows simulated results when ground truth for moments values is available. For a visual understanding of the meaning of estimation accuracy, $\overline{e}_A$, Panel(b) shows an example of estimation error computed for the raw moments, called here *Before target mask*, and for the moments estimated using the proposed approach, called here *After target mask*, where the dimension of SE for this case, is selected to provide maximum accuracy. We notice that indeed estimation accuracy is about 1 for all three moments. As stated at the beginning of this section, Panel(a) shows that indeed exists a unique value of dim_{SE} that provides the maximum accuracy, and that this is different for each moment: $1.1[log_{10}]$ for M_0 and M_1 and $2[log_{10}]$ for M_2. For this result, the threshold value used for target detection operation varies from - 10 dB to 10 dB with a step of 1 dB, while dim_{SE} is fixed. Estimation accuracy, $\overline{e}_A$ is computed based on estimation error values. For the latter, we used ground truth moments values presented in the previous section. For a more general overview of the span of accuracy values, Panel(c) shows maximum accuracy values computed for different SE dimensions: $[1,10]$, with a step of one. Mean and standard deviation for $\overline{e}_A$ values depicted in Panel(c) are shown in Table 5.4. We remark that for the right value of dim_{SE} estimation accuracy stays almost constant when threshold values are varying.

In Panel(c) red numbers show the threshold value [dB], which corresponds with the SE dimension located at the maximum accuracy. Note that $(dim_{SE}(i), Th(i))$ pairs are

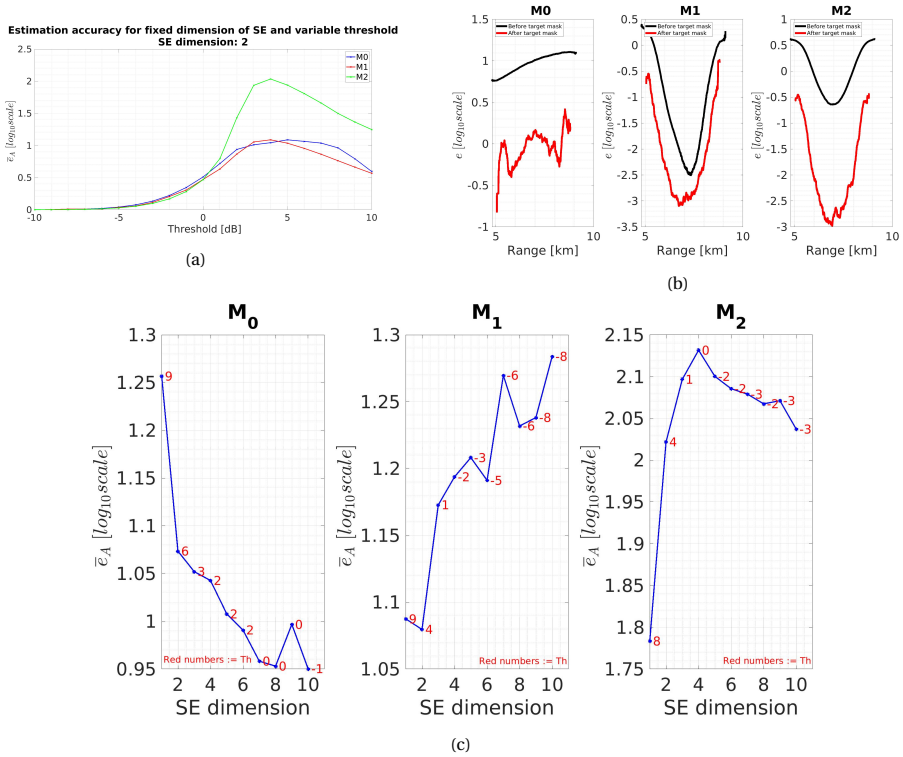

Figure 5.4: Maximum estimation accuracy results when the rate of false alarm is varying for fixed SE dimension values. In Panel(a) this experiment is carried out for one single value of dim_{SE}, while in Panel(c) for $dim_{SE} = [1, 10]$, with step of one. Panel(a) represent estimation accuracy values versus threshold for each Doppler moment: M_0, M_1 and M_2: blue line color, red line color and green line color, respectively. Red numbers represented on each subplot represent threshold value where maximum $\overline{e}_A$ value is estimated for fixed SE dimension. Panel(b) shows an example of two different estimation error results, before and after target mask, black color line, and the red color line, respectively.

	M_0	M_1	M_2
$\mu[log_{10}]$	1.02	1.18	2.04
$\sigma[log_{10}]$	0.10	0.06	0.01

Table 5.4: Mean and standard deviation for maximum estimation accuracy obtained for a range interval of threshold values from -10 dB to 10 dB.

not the same for all three moments, for this experiment, where the criteria are maximum $\overline{e}_A$. This strengthens the conclusion that the criterion for the estimation of the SE dimension has to be related to each moment. Hence, estimation accuracy has improved by about tens for M_0, and ones for M_1 and M_2. Moreover, the proposed algorithm shows constant accuracy gain for a large range of false alarm rates from about 100% to 0%.

5.4.2. PERFORMANCES USING ADAPTIVE ALGORITHM

For this subsection, we compute estimation accuracy based on dim_{SE} values estimated with the AMF algorithm. For this, we are interested in accuracy gain when one single SE is estimated for all three moments.

This study is carried out for SNR = 30 dB, when Th varies from -10 dB to 10 dB, with a step of one for two different scenarios, Figure 5.5 : SE dimension for dilation operation is 1) fixed square shape, $E_{MD} = 2 \times 2$, Panel(a) and 2) adaptive and equal with SE dimension for opening operation $E_{MD} = E_{FA}$, Panel(b). Scenario with best results is obtain based on a comparison matrix in terms of estimation accuracy, Table 5.5. In the end, a general experiment is performed for SNR varying from 10 dB to 40 dB, with a step of 5 dB, while threshold varies in the same range mentioned before, for each SNR value. Thus, mean and standard deviation that correspond with estimation accuracies for each SNR value are computed, Figure 5.5 Panel(c).

Figure 5.5, Panel (a) and (b) shows estimation accuracies versus threshold, for SNR = 30 dB, when dim_{SE} is estimated using AMF. In Table 5.5 a comparison matrix is depicted for scenarios mentioned above, in order to decide what solution is better for our case. For this, we consider estimation accuracy values in only three points of threshold value: -2, 0 and 2 dB. This range is considered large enough since a priori noise power match with a posteriori noise floor for real data. In Table 5.5 are depicted estimation accuracy values for each moment and each study case, for all three values mentioned for threshold.

	$\overline{e}_A[log_{10}]$					
Th [dB]	M_0 E^f_{MD}	M_0 E^a_{MD}	M_1 E^f_{MD}	M_1 E^a_{MD}	M_2 E^f_{MD}	M_2 E^a_{MD}
-2	0.98	0.84	1	1.22	2	1.88
0	1.02	0.96	0.92	1.1	1.95	2.15
2	1.02	1	0.7	0.9	1.8	1.88

Table 5.5: Comparison matrix for estimation accuracy between case when SE dimension for dilation operation is fixed square shape, $E_{MD} = 2 \times 2$ and adaptive and equal with SE dimension for opening operation $E_{MD} = E_{FA}$. Values are extracted from Figure and depicted for each moment and for each case where E^f_{MD} represent fixed case and E^a_{MD} adaptive case.

To select one of the cases we compare values between them for each moment. We find that the fixed SE dimension case is better with a score of four and the adaptive SE dimension with a score of five. Hence, we consider that for E_{MD} adaptive and equal with E_{FA} we obtain better results than in case when E_{MD} fixed and equal with a = 2×2 square shape.

Next, we analyze mean and standard deviation for estimation accuracy when SE dimension is adaptive and estimated using proposed algorithm, AMF. Figure 5.5, Panel(c) shows mean and standard deviation of estimation accuracy versus SNR = [0, 40] dB, blue line colour and red line colour, respectively, for each moment. Based on this we observe that mean for M_0 is almost constant and around 0.9 $[log_{10}]$, where for M_1 and M_2 is directly proportional with SNR, where the minimum value of averaged accuracy is 0.45 for M_1 and 1.25 for M_2 when SNR = 10 dB and maximum averaged accuracy is 1.1 for M_1 and 1.8 for M_2. Based on standard deviation we can infer how much accuracy is

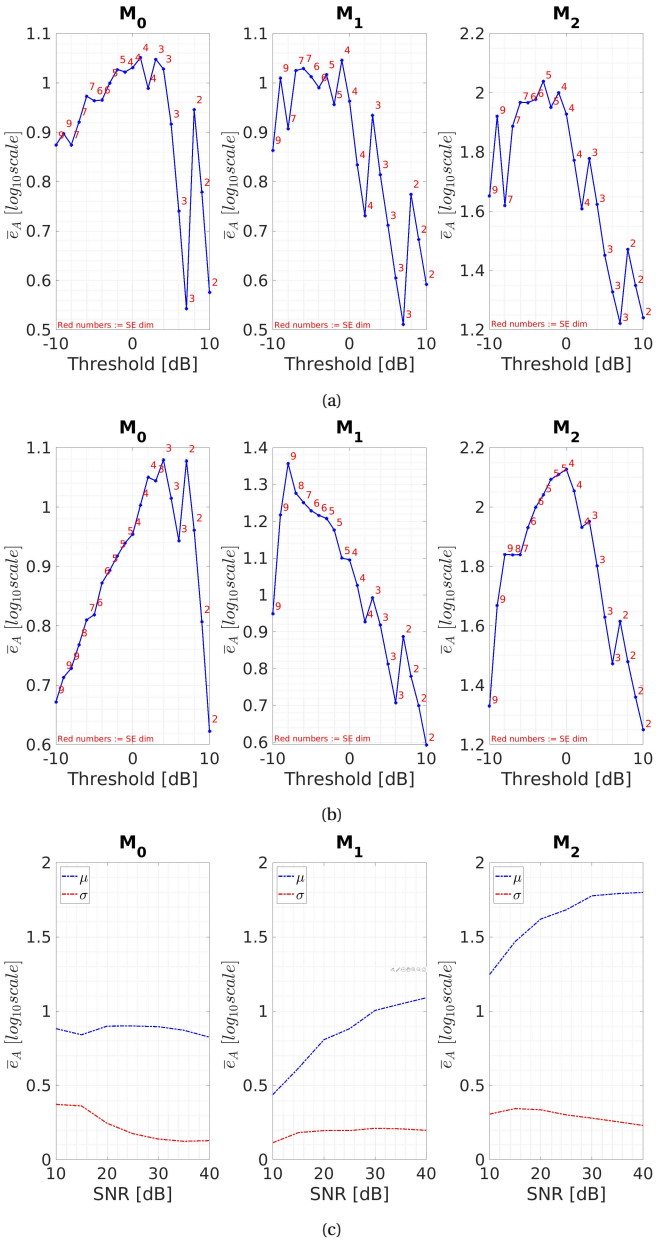

Figure 5.5: Estimation accuracy gain after target mask computed with AMF. Results are shown for Th range $[-10, 10]$ dB, with step one. Panel(a) and Panel(b) shows $\overline{e}_A$ values for a study case performed for fixed and adaptive, respectively dimension of SE in charge of dilation operation, E_{MD}, for SNR = 30 dB. Panel(c) shows an overview of the mean and standard deviation of estimation accuracies computed at different SNR values: $[10, 40]$ dB, with a step of 5 dB.

varying for different threshold values. Hence, we notice some variation for M_0 from 0.4 to 0.1, and almost constant, around 0.2 and 0.3 for M_1 and M_2, respectively. Comparison matrix of mean and standard deviation for estimation accuracy when SE dimension is computed for maximum accuracy, Table 5.4 versus when SE dimension is estimated using AMF, for SNR = 30 dB, is depicted in Table 5.6.

	SNR = 30 dB					
	M_0		M_1		M_2	
	Simulated	*Using AMF*	*Simulated*	*Using AMF*	*Simulated*	*Using AMF*
$\mu[log_{10}]$	1.02	0.9	1.18	1	2.04	1.8
$\sigma[log_{10}]$	0.10	0.2	0.06	0.2	0.01	0.3

Table 5.6: Comparison matrix of mean and standard deviation for estimation accuracy when SE dimension is computed for maximum accuracy using simulated ground truth versus when SE dimension is estimated using AMF, for SNR = 30 dB.

Based on results depicted in Table 5.6 we notice that the accuracies are comparable for all three moments, with differences of 0.12 $[log_{10}]$, 0.18 $[log_{10}]$ and 0.23 $[log_{10}]$ for M_0, M_1 and M_2, respectively. Regarding to the standard deviation values such differences are 0.1 $[log_{10}]$, 0.14 $[log_{10}]$ and 0.29 $[log_{10}]$ for M_0, M_1 and M_2, respectively.

Based on this study of the AMF performances on simulated data we can continue studying its performances for MAX3D radar data. The next chapter includes results for real data processing.

5.5. MAX3D DATA RESULTS

For this chapter we apply the proposed AMF algorithm on real data, recorded using the MAX3D radar. For this, we use the same settings of AMF algorithm as we derived from simulation: $th_{AMF} = 0.001$, $win_{size} = 2 \times 2$, $counter = 3$ and hypothesis test criteria that the first SE dimension for which $\Delta RMSE <= th_{AMF}$ is true, is selected for target mask creation. For threshold value we study two cases, 1) $Th = 0$ dB, Figure 5.6, Panel(a) to (d) and 2) $Th = 10$ dB, Figure 5.6, Panel(e) and (f). In these figures two types of results are shown: the range-Doppler map for the fixed elevation, and the elevation-Doppler map for the fixed range. For each types in figures also are included the signal processing results before target mask application, for comparison. Moreover, for $Th = 0$ dB case, we plot moments for each of two results before and after target mask application, with blue and orange line colours, respectively.

To obtain these results, the AMF is applied over one single radar cube: $[elevation] \times [range] \times [Doppler]$, and, as we mentioned in the previous chapter, a target masks are created for range-Doppler maps at each elevation. To obtain this radar cube, we first apply the rMMSE beamforming algorithm for raw data, and then we applied fast Fourier Transform (FFT) over each vector along the slow time axis. In case of range-Doppler map we opted for elevation and azimuth angles $\theta = 12.5°$ and $\phi = 35°$, respectively, and for elevation-Doppler map we opted for range = 10.5 km and the same azimuth direction $\phi = 35°$, since they belongs to the same radar cube.

These results demonstrate the performances of the proposed algorithm when applied to real data. To analyze these results we are simply making a visual investigating.

Firstly, we notice that indeed noise is clipped with a high performance of the trade-off between the sensitivity level and the amount of false alarms errors. Based on a comparison between these two cases of 1) $Th = 0$ dB and 2) $Th = 10$ dB, we notice that the trade-off mentioned before can be controlled by adjusting the threshold Th value. Thus, for $Th = 10$ dB, edges of weather target are strongly filtered out, which may cause a loss of estimation accuracy much higher than e.g. $0.5[log_{10}]$, as we obtained for SNR = 30 dB, as results of difference between accuracy when $Th = 0$ dB and $Th = 10$ dB. On the other hand, a $Th = 10$ dB may help for sidelobes suppression. For instance, for Figure 5.6 Panel(f), if we consider that targets of about 20 dB and located above 10° elevation are sidelobes, then for $Th = 10$ dB, we will clean more than 50% of them. However, to claim that those targets are sidelobes, this has to be strongly demonstrated beforehand.

Regarding the interior of the object, we notice that for both $Th = 0$ dB and 10 dB, it does not present the miss-detection errors.

For moment estimation, the biggest differences are noticed for M_1 and M_2 from 10 km to 15 km, where the spectral width of the weather target is smaller than half of the spectrum length. Hence, the effect of noise becomes more important in this case for estimation accuracy. For moments computed for the elevation-Doppler map, we notice that the most important differences are above 11° up to 20° elevation, where for the same reason as for the range-Doppler map, the noise effect is much stronger when weather spectral width is smaller than half of the spectrum.

One last observation points out the Doppler aliasing phenomenon, which is visible in the range-Doppler map from 8 km to 15 km range. Due to this effect, we notice multiple spikes in Panel (c) and (g) as well for M_2 results, if we consider that for weather targets spectral width has to be up to 2 [m/s]. The reason for this assumption is that Doppler spectrum distribution for a weather target is considered to have a Gaussian shape. Based on the theory for the probability distribution function of Gaussian distribution, 2σ contains 68.2% of the total energy. For our Doppler spectra, one standard deviation, $1\sigma = 1.08[m/s]$. Since we compute spectral width as the first standard deviation, 2 [m/s] spectral widths represent 74% of the spectra energy.

5.5.1. DOPPLER ALIASING CORRECTION ALGORITHM

For the last observation based on real data, Figure 5.6, Panel(a) and also Panel(e) show Doppler aliasing effect. This is when target's velocity exceed maximum unambiguous velocity, $|v_{max}| = 7.39[m/s]$. Because of this, same figure, Panel(c) and also Panel(g), shows strong peaks for spectral width, M_2, within range interval $[9, 15][km]$. These peaks present abnormal values, since the maximum spectral width value for the weather target has to be around 2 [m/s], and the reason for this has been described above. Therefore, a Doppler Aliasing correction (DAc) is necessary. This is not a trivial problem for the radar field, mainly because there are multiple unknown variables, like for instance if the spectrum has to be shifted to the right, or the left. Another, more difficult problem is the number of foldings that occurred. To make this decision, the proposed algorithm considers the side of the spectrum that has the greatest "weight". In other words, because the spectrum is discontinued after aliasing, the position of mean Doppler velocity is estimated on the side where the power of the spectrum is considerable. Thus, for the situation shown in Figure 5.6, Panel(a) we consider that spectrum was shifted to the left,

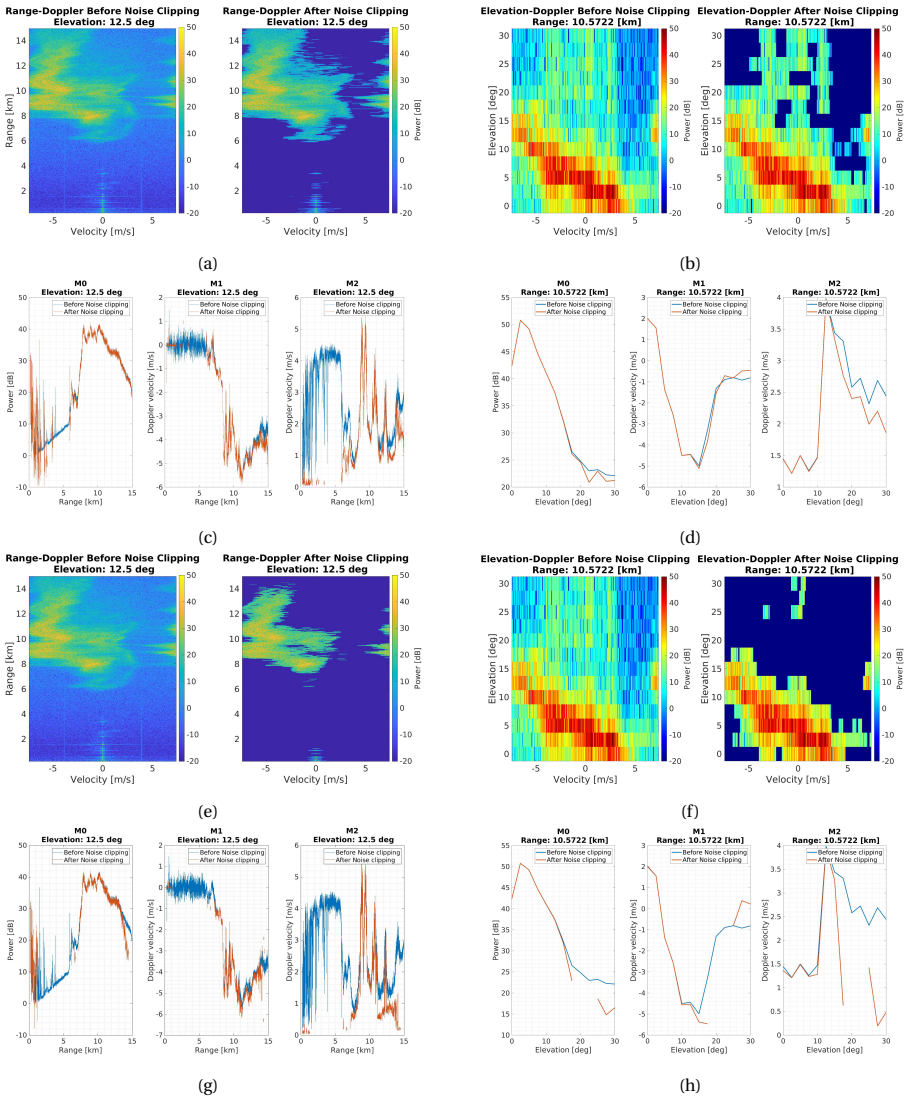

Figure 5.6: MAX3D real data results after target mask computed using AMF algorithm. For the first two rows, $th_{AMF} = 0dB$, while for the last two rows $th_{AMF} = 10dB$. The first column shows Range-Doppler map and correspondent moments estimation, where for 2D image plots, LHS image is before target mask, and RHS image is after target mask. For moment values, blue line color is before target mask and orange line color after target mask. The second column shows the Elevation-Doppler map where the same positions mentioned above are respected for results before and after the target mask. Results shown here are from the same radar cube, that corresponds with $\phi = 35°$, $\theta = 12.5°$ and range = 10.57 km.

this means that tails of the spectrum are folded, and the rest of the spectrum, located on the negative side of the spectrum is not folded. On the other hand, Panel(b) shows a case where the distribution of weather spectrum is not constant along with the range, hence

the proposed algorithm creates ambiguities.

Proposed algorithm is an iterative one which goal is to minimize the error, e_{DAc}, formulated as the difference between position of mean Doppler velocity and center of the spectra, this corresponds with 0 [m/s] Doppler velocity.

$$e_{DAc} = |ind_{M_1} - (N/2-1)| \tag{5.23}$$

$$e^i_{DAc} = (N/2-1) - ind_{M_1}, \tag{5.24}$$

where ind_{M_1} represents index of M_1 position with respect to Doppler velocity spectra, and N is the total number of Doppler bins. e^i_{DAc} is the same error in real values and recomputed for each iteration.

Thus, for each iteration, we recompute mean Doppler velocity, shift the spectrum regarding $e^{(i)}_{DAc}$. We found experimentally that the threshold value to stop the iterative algorithm has to be two. We remarked that for very narrow spectral width values, e^i_{DAc} is jumping between -1 and 1. Algorithms steps are described in the following lines.

1. Read the input Doppler power spectra, $\boldsymbol{P}^{(i)}$, for correspondent range position;
2. Compute the mean Doppler velocity, $M_1^{(i)} = \frac{1}{M_0^{(i)}} \sum_{n=1}^{N} \boldsymbol{v^{(i)}} \cdot \boldsymbol{P^{(i)}} d_v$;
3. Find index of $M_1^{(i)}$ position in Doppler spectra, $ind^{(i)}_{M_1}$;
4. Find $e^{(i)}_{DAc}$, between $ind^{(i)}_{M_1}$ and $N/2-1$; $e^{(i)}_{DAc}$ can be positive, negative or zero, $e_{DAc} = |e^{(i)}|$;
5. Using a circular shift, recompute power spectra, $\boldsymbol{P}^{(i)} \rightarrow \boldsymbol{P}^{(i)}_{temp}$, where spectrum is shifted to right if $e^{(i)}_{DAc} < 0$ or to the left if $e^{(i)}_{DAc} > 0$;
6. Recompute velocity grid, $\boldsymbol{v^{(i)}} \rightarrow \boldsymbol{v^{(i)}}_{temp}$, where $\boldsymbol{v^{(i)}}_{temp}$ has $M_1^{(i)}$ value in the center of spectra. Edges of $\boldsymbol{v^{(i)}}$ are changed with respect with $e^{(i)}_{DAc}$;
7. Recompute the total power reflectivity $M_0^{(i)} = \sum_{n=1}^{N} \boldsymbol{P}^{(i)}_{temp} d_v$;
8. Start a new iteration $i->i+1$;
9. Iterative algorithm **STOP** when $e_{DAc} < 2$.

Figure 5.7, Panel(c) shows an example of the Doppler moments estimation for data before and after DAc, when DAc algorithm performed well. This figure shows that indeed spectral width becomes significantly smaller, about 2.91 [m/s], for the range bins interval, [9,15] km, where a folding event occurs. Differences can be remarked for mean Doppler velocity as well, of about 4 [m/s] computed at a range of 9 [km]. However, in Panel(a), we notice a drawback of our algorithm, where right-hand-side (RHS) tails of the weather target are shifted to the left-hand-side (LHS) now. This phenomenon occurs when mean Doppler velocity is very close to the maximum unambiguous velocity, $|v_max| = 7.39[m/s]$. This event can be observed between 8 [km] to 12 [km]. Indeed,

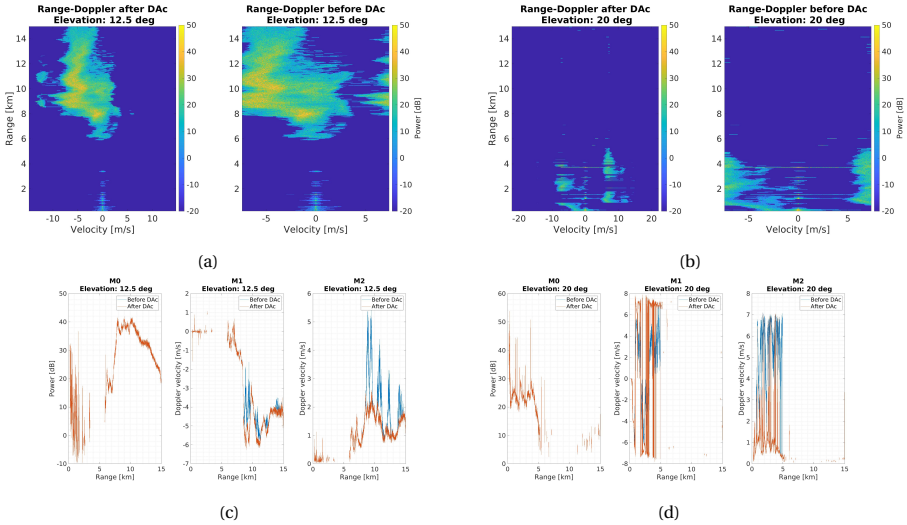

Figure 5.7: Examples of Range-Doppler map and Doppler moments, first row and second row, respectively. For first column, LHS 2D image of each panel represent Doppler spectra after DAc, and RHS of each panel before applying DAc. For second column, M_0, M_1 and M_2 is estimated, where blue line colour represents results before and orange line colour represent results after DAc.

for moment estimation values of M_1, these values reaches almost 6 [m/s]. However, the estimation error of mean Doppler velocity for values before and after DAc, are about 3 [m/s] for the exact area where DAc algorithms drawback occurs.

Figure 5.7, Panel(b) shows a more difficult example of aliasing. We notice in this case that DAc cannot retrieve the true error and spectra at some ranges are estimated to have the incorrect velocity. However, for this kind of situation and also for the number of foldings that occur, a more sophisticated algorithm is necessary.

5.6. CONCLUSIONS

In this chapter, the accuracy gain of precipitation profiles estimation was studied after the removal of additive noise from Doppler spectra. A weather targets detection method was derived, called AMF. This method uses a priori averaged range profiles of the noise power and morphological operations, opening, and dilation with an adaptive approach for the dimension of SE. The verification of this approach was done using simulated and real data.

For simulated data, the maximum accuracy for a fixed rate of the false alarm estimated by trying a range of multiple dimensions for SE. Based on this, it was proved that there is one unique SE dimension that gives maximum accuracy, different for each Doppler moment. For a more general overview, this was proved for a large range of false alarm rates, from about 100% to 0%.

Next, AMF proved to provide accuracy gain close to the previous experiment, around 88%, even if for previous we noticed that for the same false alarm rate accuracy takes maximum value at slightly different dimensions of SE for each Doppler moment, wherein

our case at fixed false alarm rate we adaptively estimate only one dimension of SE.

Stability and robustness of the AMF algorithm were proved based on a large experiment, SNR = [10, 40] dB, where mean and standard deviation was computed for accuracy gain values obtained at constant SNR and varying false alarm rate, within the same interval mentioned before.

In the end, performances of AMF and its benefits were proved for MAX3D real radar data, where was tested for two different threshold values for target detection, $Th = \{0, 10\}$ dB. We notice that the target's interior does not contain any missed detection for both threshold values and that only edges are slightly eroded for Th = 10 dB. However, we notice that the higher is Th the better sidelobes, and noise is suppressed around the weather target without jeopardizing the accuracy of precipitation profiles. Additionally, an iterative algorithm to correct for the Doppler aliasing phenomenon was introduced, and its performances were proved based on real data simulation. However, we noticed that for MAX3D there are situations more complicated of aliasing which requires a more sophisticated algorithm for correction.

REFERENCES

[1] C. Debes, J. Riedler, M. G. Amin, and A. M. Zoubir, *Iterative target detection approach for through-the-wall radar imaging, 2009 IEEE International Conference on Acoustics, Speech and Signal Processing,* , 3061 (2009).

[2] R. C. Gonzalez and R. E. Woods, *Digital image processing* (Prentice Hall, Upper Saddle River, N.J., 2008).

[3] S. S. Aung, I. Nagayama, and S. Tamaki, *An adaptive morphological operation for high-performance weather image processing,* IEIE Transactions on Smart Processing and Computing **7**, 424 (2018).

[4] R. Firoz, S. Ali, M. N. U. Khan, and K. Hossain, *Medical image enhancement using morphological transformation,* Journal of Data Analysis and Information Processing **4**, 1 (2016).

6

RECONSTRUCTION OF 3D DOPPLER MAP

This chapter's objective is the reconstruction of 3D Doppler map. 3D representation of precipitation profiles in terms of total power reflectivity, mean Doppler velocity or spectral width implies a polar to Cartesian transformation since beamforming operation is a spatial transformation that results in mapping the targets in terms of elevation and range, this is polar coordinates. Because of this, the single possible 3D representation is for constant elevation Plan Position Indicator (PPI). In general, precipitation profiles are represented for constant height PPI for the reason that wind direction and velocity's magnitude are considered to be constant at a constant height, which provide to the user a better understanding of natural phenomenon. Data can be transformed from polar to Cartesian coordinates using an interpolation operation. Thereby, this chapter introduces our proposed approach for 3D reconstruction of precipitation profiles, where polar to Cartesian transformation is applied for the components of radial mean Doppler velocity and spectral width, that are elements of the vector space, while for total power reflectivity this transformation is applied directly since these values are scalar elements. Then a study of the interpolation problem is carried out, to determine the complexity in this case. Knowing this, the study is carried on by a comparison of different interpolation methods, linear, cubic, spline and modified Akima, to determine which methods give the smallest interpolation errors. For this study, the Franke's test function is used. To the end, the proposed methodology is applied to real radar data, and a collection of results are displayed. Here are included a set of eight constant height PPI for each moment at four different heights, where for mean Doppler velocity are shown both horizontal and vertical components. Next, a set of four constant azimuth Range Height Indicator (RHI) plots are presented for all moments, where for mean Doppler velocity are displayed both components, as well.

6.1. INTRODUCTION

THIS chapter opens with a derivation for vector components of mean Doppler velocity and spectral width. Their formulation is done using integral equations stated in Chapter 3. For this case, we use discrete expressions. Vector components, as a function of elevation angle, θ, for radial mean Doppler velocity are:

$$\mu_{v_h} = \frac{1}{P_T} \sum_{i=-N_D/2}^{i=N_D/2} \boldsymbol{v_h}(i) |\hat{\boldsymbol{A}}(i)|^2 dv = \tag{6.1}$$

$$= \frac{cos(\theta)}{P_T} \sum_{i=-N_D/2}^{i=N_D/2} \boldsymbol{v}(i) |\hat{\boldsymbol{A}}(i)|^2 dv \tag{6.2}$$

$$\mu_{v_h} = cos(\theta)\mu_v \tag{6.3}$$

$$\mu_{v_t} = sin(\theta)\mu_v \tag{6.4}$$

, where μ_{v_h} and μ_{v_t} are horizontal and vertical components of radial mean Doppler velocity, μ_v.

Follower, by vector components for spectral width:

$$\sigma_{v_h} = \sqrt{\frac{1}{P_T} \sum_{i=-N_D/2}^{i=N_D/2} (\boldsymbol{v_h}(i) - \mu_{v_h})^2 |\hat{\boldsymbol{A}}(i)|^2 dv} = \tag{6.5}$$

$$= \sqrt{\frac{1}{P_T} \sum_{i=-N_D/2}^{i=N_D/2} (\boldsymbol{v}(i)cos(\theta) - \mu_v cos(\theta))^2 |\hat{\boldsymbol{A}}(i)|^2 dv} = \tag{6.6}$$

$$\sigma_{v_h} = cos(\theta)\sigma_v \tag{6.7}$$

$$\sigma_{v_t} = sin(\theta)\sigma_v \tag{6.8}$$

, where σ_{v_h} and σ_{v_t} are horizontal and vertical components of Doppler spectral width, σ_v.Total power reflectivity is a scalar and does not depend on the elevation angle, θ.

The structure of this chapter is the following. Section 1 introduces the interpolation process involved in polar to Cartesian transformation, supported by scatter plots for both systems of coordinates, followed by an analysis of the complexity of the interpolation problem. In Section 2, five different interpolation methods are introduced: *nearest neighbor, linear, cube, spline* and *modified Akima's method*, both theoretical but also with correspondent simulation performances for 1D and 2D problems. For the 2D case, the bivariate *Franke's test functions* is introduced and used to perform interpolation error estimation. Comparison results are performed based on three characteristics: *accuracy*, *visualisation aspect* and *computational time*. Results are provided for one single test function, but three different data sample points: 51, 26, and 5, out of 101, using a regular step.

6.2. INTERPOLATION PROBLEM FOR POLAR TO CARTESIAN TRANSFORMATION

The processing chain involved in the estimation of precipitation profiles for a phased antenna array starts with beamforming processing of raw data. Hence, for raw data radar cube, described by three coordinates, [channels] × [range] × [slow-time], beamforming processing implies a spatial transformation of the input signal, which result in a mapping of detected targets in terms of elevation [θ] and range [km]. The next step is Doppler processing along the slow time axis, which maps weather targets in polar coordinates, (θ,r), and radial Doppler velocity. Assuming that Doppler spectrum distribution for weather objects follows approximately a Gaussian distribution, all three moments can be estimated: total power reflectivity, mean Doppler velocity, and standard deviation (spectral width). At this stage, the only possibility for the reconstruction of the 3D Doppler map is using constant elevation PPI. This is a 2D image at constant elevation of precipitation profiles for all azimuth direction [$\phi = [0°, 360°]$]. In other words, this means a radial cross-section of the space surrounding the radar position. This situation is depicted in Figure 6.1 for representation in Cartesian coordinates of two different radial direction for elevation angles, θ_1 and θ_2 and constant azimuth direction.

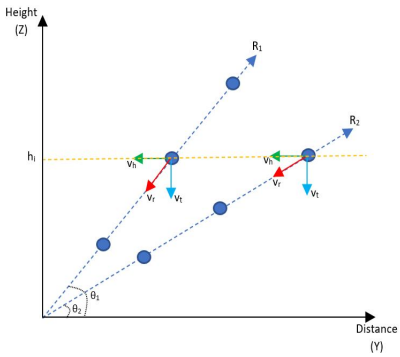

Figure 6.1: Example of points mapped in Cartesian coordinates. The vertical axis represents *height* or Z and horizontal one *distance* or Y. Blue points represent position (y, z) of a target and arrows represent radial velocity and its components, horizontal and vertical, drawn with a red color arrow, green color arrow, and blue color arrow, respectively. Radial direction, R_1 and R_2 are characterized by elevation angles, θ_1 and θ_2, respectively. Yellow color dashed line represent a constant height section, for height, h_i

A general assumption about wind field is that wind direction and velocity are constant for a fixed height. In this case, a constant height PPI representation of precipitation profiles provides a better overview of the weather situation. For the main goal of this project, this means a clearer examination of the capabilities for MAX3D radar to perform estimation of the wind field. A schematic drawing for the constant height PPI representation is depicted in Figure 6.1, represented by a yellow dashed line, at height h_i. This example is considered for the first moment only, this is radial mean Doppler velocity, drawn as a vector with a red arrow. Then, constant height representation includes horizontal components of radial Doppler velocity, drawn as a vector with a green arrow

for two different points positioned at different elevations and ranges. Now, for the RHI representation, this provides a similar aspect as the one depicted in Figure 6.1. Hence, after derivation of vector components, followed by a mapping of values to the Cartesian coordinates, possible by interpolation operation, one can represent either PPI or RHI plots.

Let us consider that targets are mapped in a 2D polar system of coordinates, called *polar grid*, characterized by $(\theta_{i,j}, r_{i,j})$ coordinates and one want to map the targets in a Cartesian system grid, characterized by $(x_{i,j}, y_{i,j})$ coordinates. If we call *transformation grid*, the grid of polar coordinates values obtained as results of Cartesian to the polar transformation of the coordinates of the Cartesian grid where one intends to map the targets, then interpolation process involved in this process is a *bilinear interpolation* and is performed between transformation grid and actual polar grid obtained as a result of spatial transformation through beamforming algorithm. Bilinear interpolation is an extension of linear interpolation and is employed for interpolation of two-variable functions, $f(x, y)$, on a rectilinear 2D grid. Figure 6.2, Panel(b) for a zoomed-in aspect, shows both polar grid and transformation grid, black color circles and multi-colors "x" points, respectively.

By comparing these two grids, polar and transformation grid we can determine the complexity of the interpolation problem. Even if the transformation grid is irregular, and the reason is due to the Cartesian to polar non-linear equations, Eq. 6.9, this is not a problem as long as the polar grid, black color circles, is regular and represent the basis grid for interpolation.

$$\theta = \tan^{-1}\frac{y}{x} \tag{6.9}$$

$$r = \sqrt{x^2 + y^2} \tag{6.10}$$

Hence, interpolation error is fixed and known for any values within data and is dependent only on the interpolation accuracy of chosen interpolation method. For instance, linear interpolation error is the biggest one and is proportional to the square of the distance between data points, where for polynomial interpolation the error is proportional to the distance between data points to the power n, where the polynomial's degree is n-1, for n data points. Thereby, the next section shows estimation errors for five different interpolation methods.

6.3. STUDY CASE FOR BILINEAR INTERPOLATION ERROR

Interpolation methods involved in our study case are: *nearest neighbor, linear, cube, spline* and *modified Akima's method*. They are briefly described in Table 6.1.

Figure 6.3 shows simulation results for 1D interpolation. Only ten points are given and are interpolated for one hundred. This result gives us an overview of the performances of each interpolation method. The theoretical background and results can be compared for each method using their independent performance within this figure

Based on Figure 6.3 we can notice that there is a big difference between *spline* and other two first-derivative continuous interpolation methods, *cube* and *makima*. In the

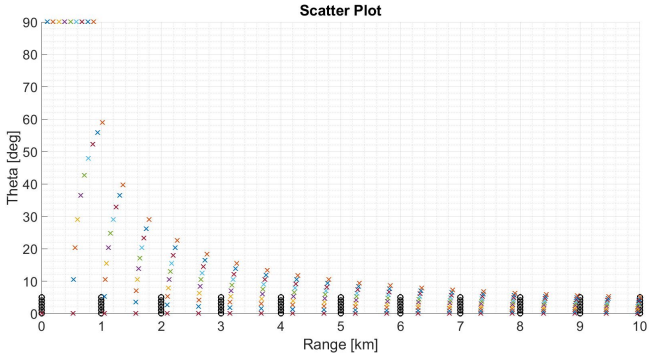

(a)

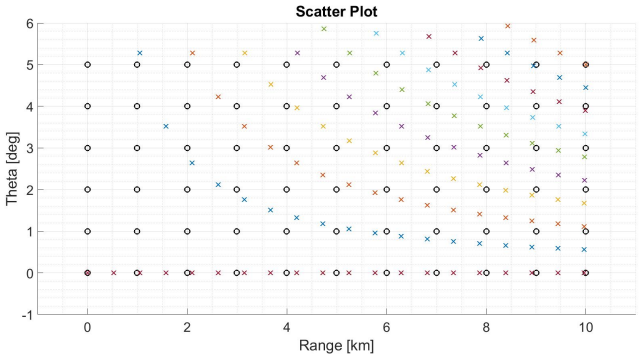

(b)

Figure 6.2: Example of polar and transformation grid, black color circles and multi-colors "x" points, respectively. Transformation grid is the polar coordinates grid obtained after transformation of Cartesian coordinates in polar coordinates. Panel(b) shows a zoomed in version of Panel(a).

case of *spine*, it tends to overestimate local maxima and minima, being out of the range of samples, but also computing a wrong position of the local maxima for the point located at (0.2,0.9). Based on this we can conclude that the *spline* method is not appropriate for abrupt changes in the function. Much more impression about these methods is discussed for the bivariate case.

For the study of interpolation operation, of any dimension, there is necessary a test function. For this study case we opted for *Franke's test function* [1], represented in Figure 6.5, Panel(a). This function has two Gaussian peaks of different heights, and a smaller dip. The function is evaluated on the square $x_i \in [0,1]$. In our case we opted that original function has 101 × 101 points. In order to test the interpolation methods, there were used three different number of points for sampling : 5 × 5 points, 26 × 26 points and 51 × 51 points, which later in the chapter are refered as *undersampling* ratios: 0.0025, 0.0676 and 0.26, respectively. The undersampling ratio formula that we used is:

$$UR = \frac{N_b}{N_a} \tag{6.11}$$

Method	Description	Continuity	Comments
Nearest Neighbor	The interpolated value at the query point is the value present at the nearest sample on the grid	Discontinuous	Requires only two points in each dimension.
Linear	The interpolated value at the query point (y,x) is computed using linear equations between the left and right points, (y_a, x_a) and (y_b, x_b) respectively, where the slope between left point and query point is the same as the one between left and right points.	C^0	Quick and easy, but not very precise - error is proportional with square the distance between two interpolation points; Requires two points for each dimension; Interpolant is not differentiable at the point x_k;
Cubic	If the values of a function f(x) and its derivatives are known at two different points x_a and x_b, then the function can be interpolated on the interval (x_a, x_b) using a third degree polynomial. Because derivatives has to be estimated, there are required 4 points, x_0, x_1, x_2 and x_3, where the interpolation performed between x_1 and x_2, but derivatives for x_1 and x_2 are estimated based on the slope values between (x_0, x_1) and (x_1, x_2) respectively.	C^1	Requires at least four points in each dimension; Uniform spacing between points in each dimension; Requires more time than 'Linear'.
Spline	Called also cubic spline, it computes a third degree polynomial with the additional constraint that the first and second derivative at the query points are continuous.	C^2	Requires four points in each dimension; Requires more memory and computational time than 'Cubic'.
Modified Akima	Performs cubic interpolation to produce piece-wise polynomials with continuous first-order derivatives. Compared with cubic or spline algorithms, in Akima's method estimated derivative of each interval point, (x_a, x_b) is computed as weighted average between slopes of three points.	C^1	Requires at least 2 points in each dimension; Computational time is smaller than 'spline'; Compared to the spline algorithm, the Akima algorithm produces fewer undulations; It is better suited to deal with quick changes between flat regions.

Table 6.1: Interpolation methods - Description and Observations

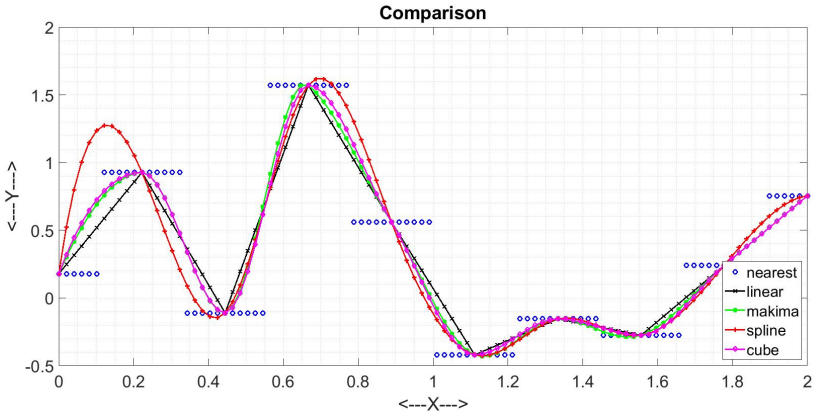

Figure 6.3: Example of interpolation results between five different methods: nearest neighbour, linear, makima, spline and cube, represented by blue dots, black dashed line, green dashed line, red dashed line and pink dashed line, respectively.

,where N_b, represent number of points before interpolation: 5^2, 26^2, 51^2, and N_a, number of points after interpolation: 101^2. Nearest neighbouring method is not considered for 2D study case because it is discontinuous.

The characteristics used for the comparison of different interpolation methods are: *interpolation error*, *visualisation aspect* and *computational time*.

Hence, in terms of interpolation error, Figure 6.4 shows three different examples for all three undersampling ratios. Figure 6.4shows that the smaller is the undersampling ratio the higher is the RMSE value. What it is important to notice here is that for a high undersampling ratio, higher than 0.0025, the spline method, yellow color line, gives the

best results. As a result Panel(a) and Panel(b) shows that RMS for the spline method has the lowest value. However, we notice that for the undersampling ratio of 0.0025, the spline method presents worse results than the linear method. This effect can be explained based on the overestimation effect that the spline method shows for 1D results as well in Figure 6.3.

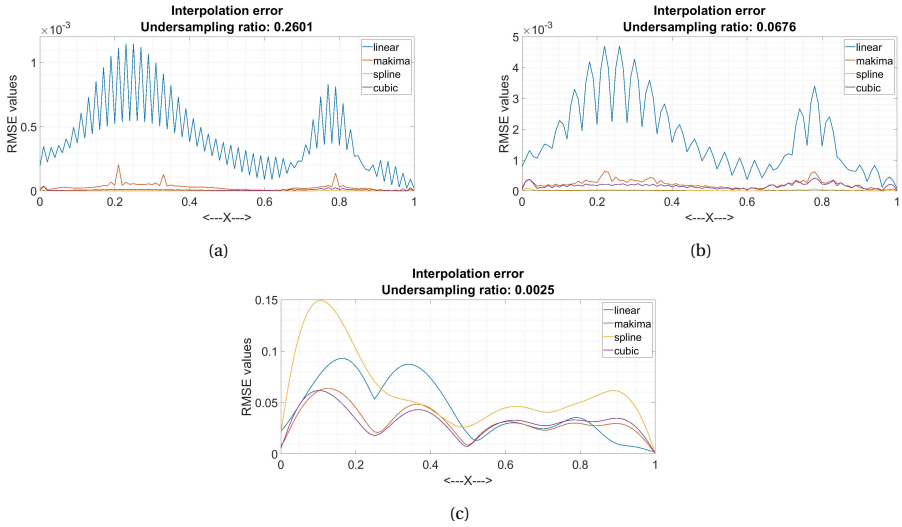

Figure 6.4

For visual inspection, Figure 6.5 shows interpolation results at undersampling ratio, 0.0025, for cubic, spline and modified Akima, Panel(b), (c) and (d), respectively, compared with original Franke's bivariate test function, Panel(a). Based on values on the Z-axis, it can be remarked the overestimation effect that occurs for the spline method. There are no visual differences between cubic and modified Akima, but there can be noticed between these two and test functions. Thus, the kurtosis of the smaller bell is smaller after interpolation, and for the same reason, the peak of the dip cannot be noticed anymore.

Regarding the computational time, Table 6.2 includes computational times for each method, at each undersampling ratio. These results are obtained for a Monte Carlo test of 500 runs. Thus we can notice that linear, cubic, and spline gives similar results for this study, compared with modified Akima which is almost two times more time-consuming than the other methods.

To conclude, based on all three results for accuracy, visual inspection, and computational time, we consider that cubic method gives the best results for the test function that we chose, Franke's test function. Since this function is complex with similar characteristics meet also for weather objects, we consider to use cubic method for the real data simulation, presented in following section.

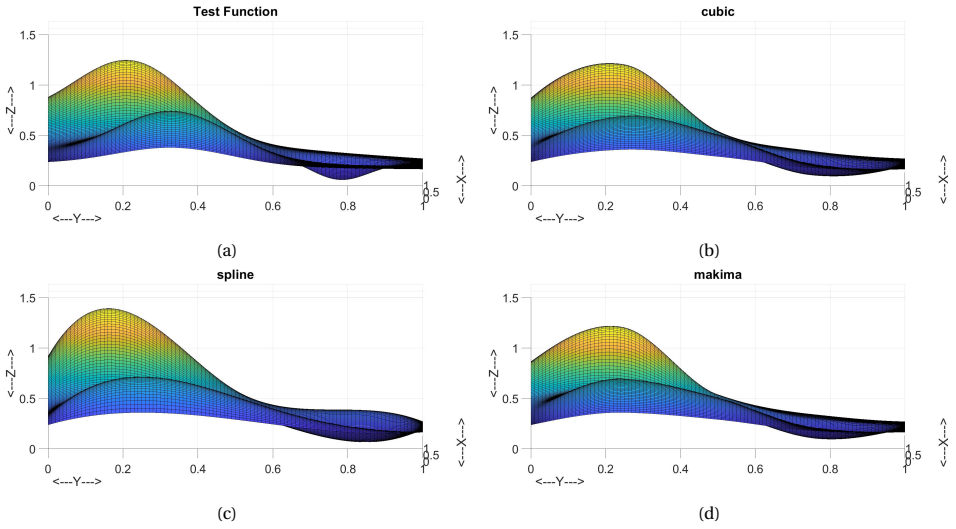

(a) (b) (c) (d)

Figure 6.5

Oversampling Ratio	Computational Time [ms]			
	Linear	Cubic	Spline	Modified Akima
0.0025	0.4180	0.5944	0.4158	0.9395
0.0676	0.4449	0.5820	0.4848	1.0398
0.26	0.4736	0.6162	0.6652	1.3914

Table 6.2: Interpolation - Computational Time comparison

6.4. MAX3D DATA RESULTS

6.4.1. DATA QUALITY MASK - PRELIMINARY FILTERING STEP

This section shows results for the reconstruction of the 3D Doppler map. For this, three different sets of results are included. Data presented here was recorded on 12^{th} of May 2021 at time 16 : 04 : 28 CEST. Rotation speed 1 RPM. The total number of sweeps is around 285. Doppler processing is used without *zero padding*, and are used only 256 sweeps out of 285 available at this rotation speed. For beamforming processing cMMSE is used, and for high estimation accuracy of precipitation profiles, AMF is employed. Correction for Doppler aliasing is not performed, due to the low performances acquired for this data set. For the interpolation process, involved for polar to Cartesian transformation of data values, are used $[Z] \times [Y] = [100] \times [100]$ points. The reason for this choice is due to the fast computation time and the sufficient level of details obtained.

The first results show the performance results for *Data Quality Mask* DQM algorithm. The DQM implies precipitation profiles thresholding based on two parameters, M_0 and M_2. This mask is a 2D binary image. This mask is initialized with value one, for all pixels, and based on the results obtained after thresholding, pixels that present the null hypoth-

esis becomes zero. After formation of the mask $\boldsymbol{DQM}$ matrix, it is applied over the matrix of moments values: $\boldsymbol{M_0}$, $\boldsymbol{M_1}$ and $\boldsymbol{M_2}$, total power reflectivity, mean Doppler velocity and spectral width. Operation used to apply $\boldsymbol{DQM}$ is Hadamard product, $[]k$.

Hypothesis test functions are:
For M_0:

$$H_0 : M_{0\,i,j} < 10[dB] \tag{6.12}$$
$$H_1 : M_{0\,i,j} > 10[dB] \tag{6.13}$$

, where H_0 is null hypothesis and means that for any value of total power reflectivity moment, that is under $10[dB]$ return zero, otherwise return 1. For M_2:

$$H_0 : M_{2\,i,j} > 2[m/s] \tag{6.14}$$
$$H_1 : M_{2\,i,j} < 2[m/s] \tag{6.15}$$

, where H_0 is null hypothesis and means that for any value of spectral width moment, that is over $2[m/s]$ return zero otherwise is 1.
These two conditions are applied over the same matrix $\boldsymbol{DQM}$. Final $\boldsymbol{DQM}$ is applied over all matrices that corresponds with each moment values:

$$\boldsymbol{DQM} \circ \boldsymbol{M_0}$$
$$\boldsymbol{DQM} \circ \boldsymbol{M_1}$$
$$\boldsymbol{DQM} \circ \boldsymbol{M_2}$$

The scope of the first condition is to filter out moments values computed for the edges of the target and the second condition is to filter out any other artifacts that are a non-weather target since we noticed that for weather targets, spectral width is up to $M_2 = 2[m/s]$. Moreover, this condition for spectral width, clean spectra out of high power level due to the receiver's saturation. Figure 6.6, Panel(a) shows the results before DQM, and Panel(b) after DQM. On one hand, the receiver's saturation effect, around $4[m/s]$ with yellow-green color, is filtered out, but on the other hand, because of velocity aliasing, an important area of the cloud is eliminated. These areas are shown with red color, around $6[m/s]$.

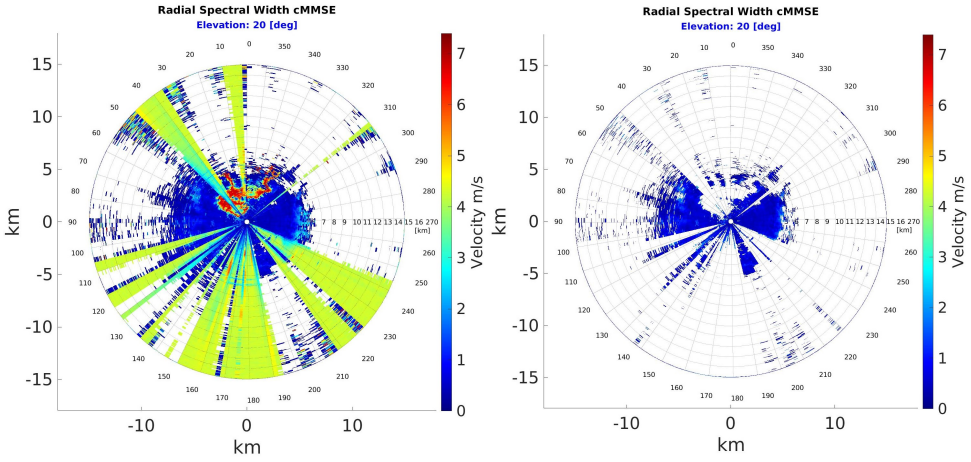

(a) (b)

Figure 6.6: Constant elevation PPI plots for spectral width before and after Data Quality Mask. Panel(a) before DQM, Panel(b) after DQM.

6

6.4.2. CONSTANT HEIGHT PPI

The second set of results shows constant height PPI plots. These results are presented for height values: $\{300[m], 370[m], 450[m], 520[m]\}$, Figure 6.7, Figure 6.8, Figure6.9 and Figure 6.10. Each figure presents results after DQM and for each moment as follows:

1. (a) total power reflectivity;

   (b) horizontal projection of radial mean Doppler velocity;

   (c) vertical projection of radial mean Doppler velocity;

   (d) and horizontal projection of spectral width.

Considering that negative velocity means approaching target and positive velocity receding target, these Panel(b) for each height show the estimation of wind velocity based on a cloud close to the radar, which is approaching from around $\phi = 50°$ azimuth direction and is receding on about $\phi = 230°$ azimuth direction. We can also see the position where wind velocity is perpendicular with the position of the radar, at $\phi = 320^{circ}$. Panel(a) shows the distribution of power in the weather target, and Panel(d) shows the spectral width, of the weather target which is below $2[dB]$. Looking over these results over different heights, we notice that with a step of 70 [m], and over a height range of 200 [m] direction of the wind is not changing. Based on this result we checked the good functionality of the weather signal toolbox developed in this project.

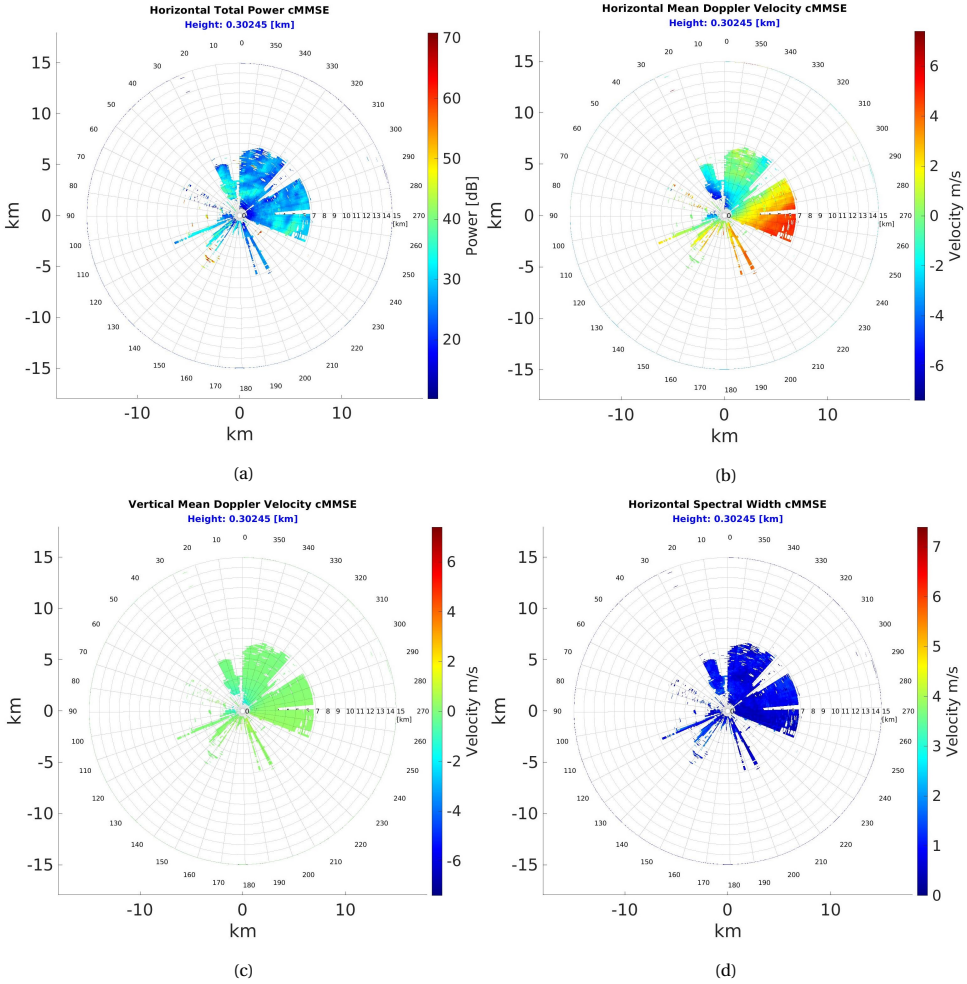

Figure 6.7:]

Constant height PPI plot for all three moments: total power reflectivity (a), horizontal projection of radial mean Doppler velocity (b), vertical projection of radial mean Doppler velocity (c) and horizontal projection of spectral width (d), for height 300[m].

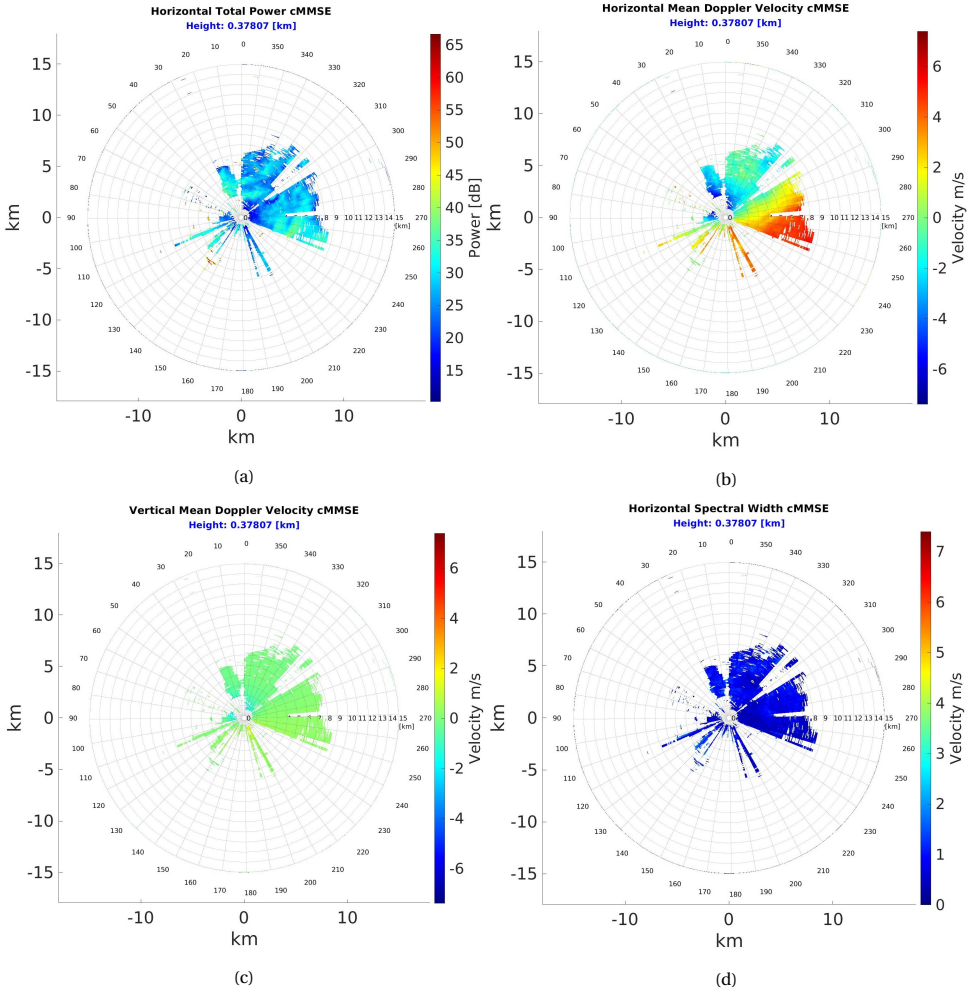

Figure 6.8:]

Constant height PPI plot for all three moments: total power reflectivity(a), horizontal projection of radial mean Doppler velocity(b), vertical projection of radial mean Doppler velocity(c) and horizontal projection of spectral width(d), for 370[m]

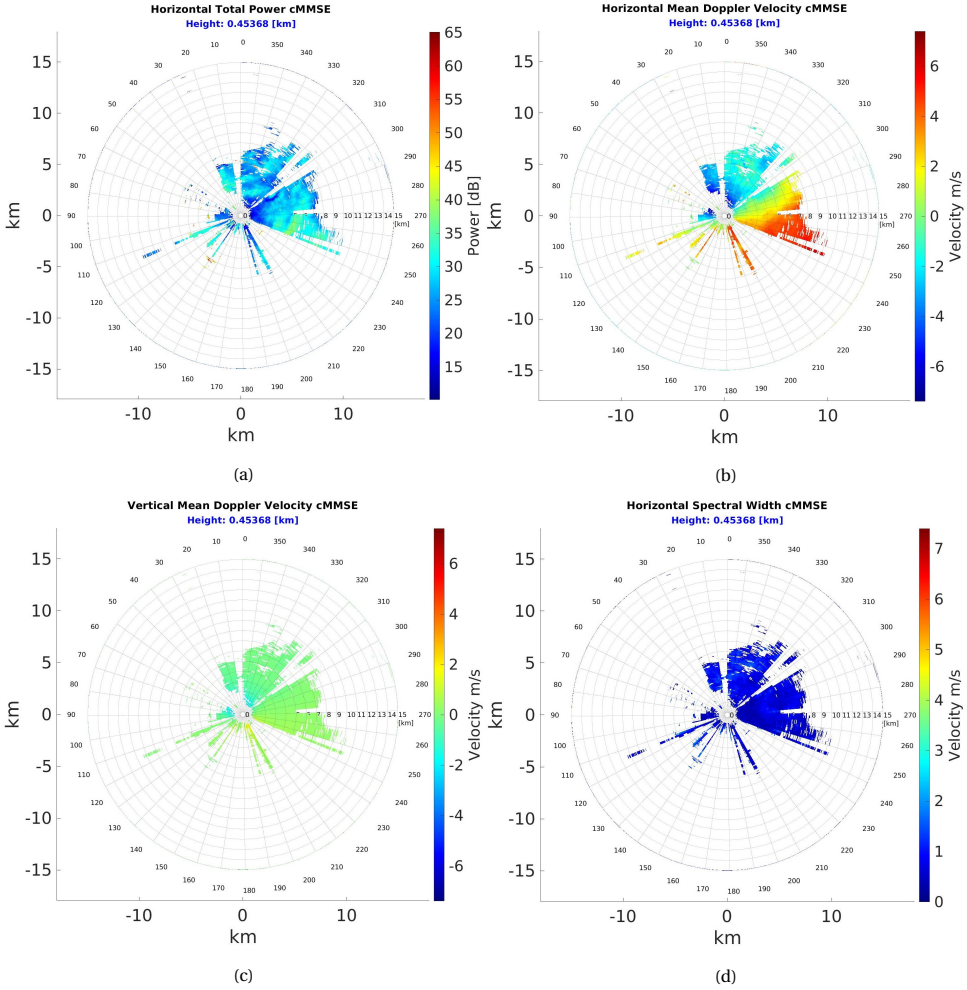

Figure 6.9:]

Constant height PPI plot for all three moments: total power reflectivity(a), horizontal projection of radial mean Doppler velocity(b), vertical projection of radial mean Doppler velocity(c) and horizontal projection of spectral width(d), for 450[m]

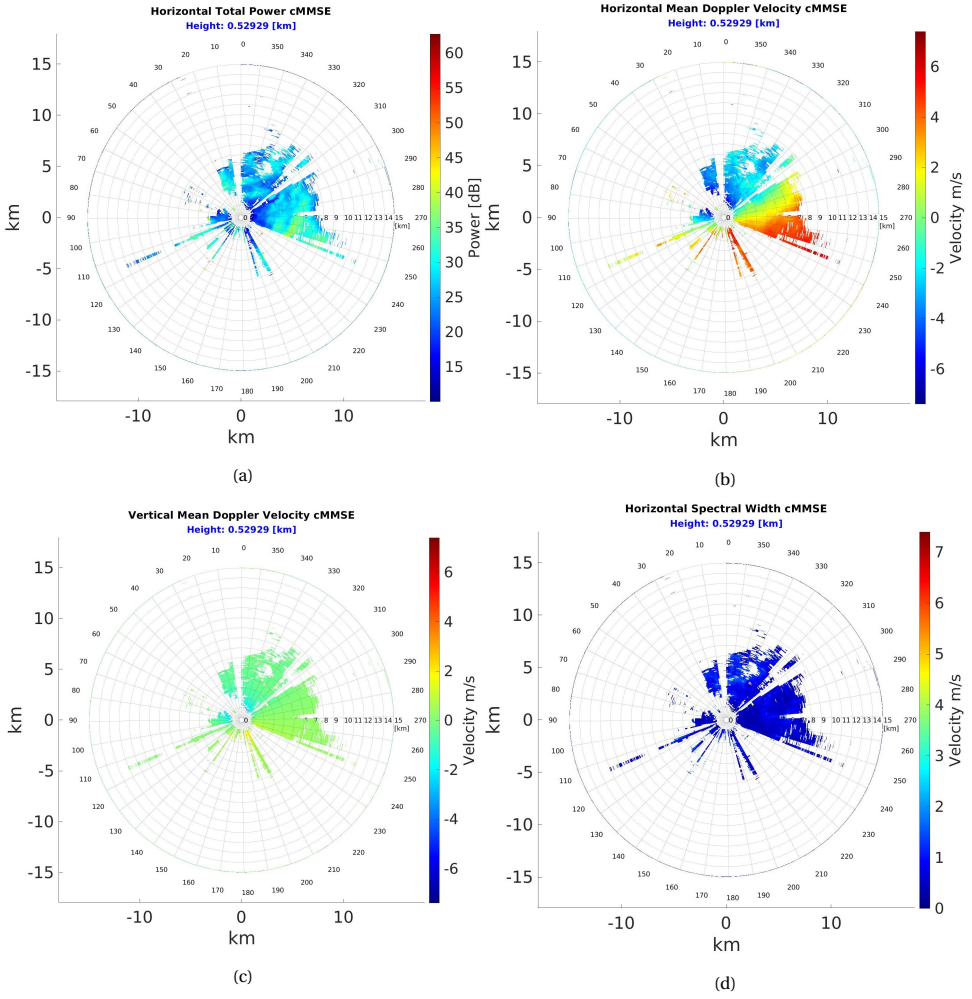

Figure 6.10:]

Constant height PPI plot for all three moments: total power reflectivity(a), horizontal projection of radial mean Doppler velocity(b), vertical projection of radial mean Doppler velocity(c) and horizontal projection of spectral width(d), for 520[m]

6.4.3. CONSTANT AZIMUTH RHI

The third set of results present constant azimuth RHI, for the same set of weather data after using DQM, at two different azimuth angles: $\phi = 264^\circ$ and $\phi = 282$, Figure 6.11, Figure 6.12, respectively. Each Panel present the results for:

1. (a) total power reflectivity;
   (b) horizontal projection of radial mean Doppler velocity;
   (c) vertical projection of radial mean Doppler velocity;

(d) and horizontal projection of spectral width.

These results show a perpendicular cross-section through the weather object, where we can notice with high resolution the distribution of the power in this cloud, Panel(a), and the radial means Doppler velocity, that corresponds with different layers obtained after radar's scanning. Thus, close to the ground, around 250$[m]$ we can notice the **melting** layer, which is the layer when the droplets start to leave the cloud.

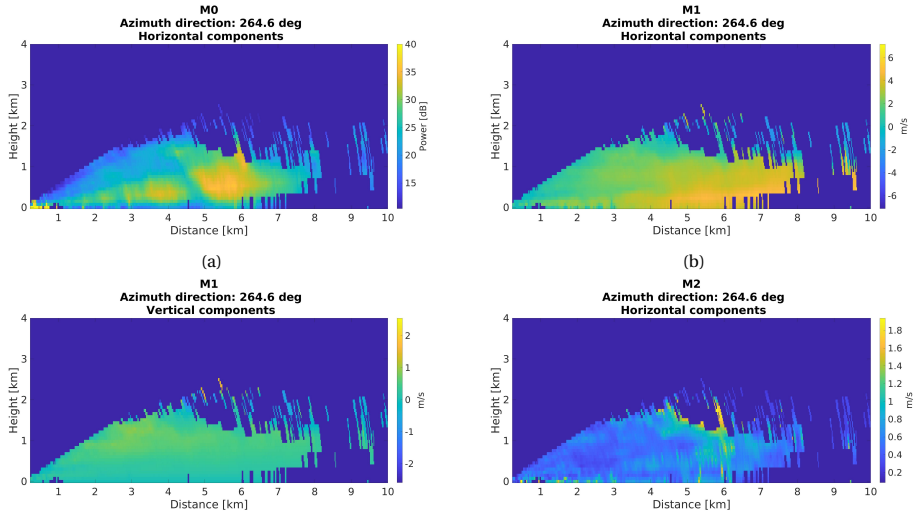

Figure 6.11: Constant azimuth RHI plots for all three moments: total power reflectivity (a), horizontal projection of radial mean Doppler velocity (b), vertical projection of radial mean Doppler velocity (c) and horizontal projection of spectral width (d), for $\phi = 264°$

6.5. CONCLUSION

In this chapter, a methodology for the reconstruction of the 3D Doppler map was introduced. For this, the bilinear interpolation process involved in the transformation from polar to Cartesian coordinates of precipitation profiles was studied. Different interpolation methods were studied: linear, cubic, spline, and modified Akima, for both 1D and 2D test functions. The study included a comparison of these methods concerning three criteria: interpolation error, visual inspection, and computational time. The best candidate was a cubic interpolation, which is chosen for following real data results.

Target mask for data quality, DQM is introduced and the result shows that precipitation profiles with high power level due to the receiver saturation effect are removed.

Real data results have been presented for constant height PPI and constant azimuth RHI plots. Constant height PPI plots are shown for total power reflectivity, the horizontal and vertical component of mean Doppler velocity, and the horizontal component of spectral width. Constant azimuth RHI plots are introduced for the same moments of Doppler weather spectra, as was introduced for PPI plot.

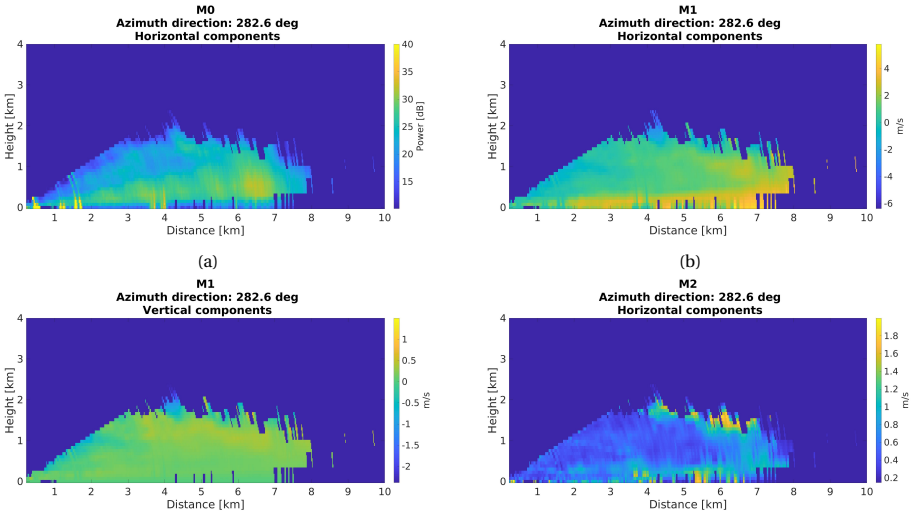

Figure 6.12: Constant azimuth RHI plots for all three moments: total power reflectivity (a), horizontal projection of radial mean Doppler velocity (b), vertical projection of radial mean Doppler velocity (c) and horizontal projection of spectral width (d), for $\phi = 282°$

REFERENCES

[1] R. Franke, *Scattered data interpolation: Tests of some method,* Mathematics of Computation **38**, 181 (1982).

7

CONCLUSIONS AND RECOMMENDATIONS

7.1. CONCLUSIONS

THIS thesis project has been formulated as a part of the EFRO project, "4D weather mapping for vortex prediction, wind fields, and precipitation now-casting" for the development of a signal processing toolbox to support the required processing adaptations of phased array antenna radar, MAX3D, for the reconstruction of 3D Doppler map at high estimation accuracy. MAX3D is a phased array radar developed and produced by Robin Radar and has been developed for bird detection. Due to the demanding requirements for a radar system for early detection and warning of fast forming weather phenomena, conventional weather radar with parabolic antenna does not have enough time-resolution and elevation resolution. Since this is possible for the phased array radar systems due to the fast electronically elevation scanning and high refresh rate and these systems are already developed and proved to provide high performances for point targets, an upgrade for a weather target detection processing channel should be implemented. Therefore, the main objective was to determine if the actual configuration of MAX3D radar is suitable for weather applications and to develop a signal processing toolbox for the high estimation of precipitation profiles and reconstruction of 3D Doppler maps.

The requirement for the signal processing toolbox, called *MAX3D-Weather-PhAA*, was to provide all the algorithms along the data processing chain, from raw data reading to the final 3D Doppler map creation and visualization. Signal processing algorithms already existing were studied and compared to determine the performances for MAX3D radar data and new algorithms were proposed for cases when the existing ones were not compatible with our project requirements. *MAX3D-Weather-PhAA* has nine main algorithms and those are:

- *Reading data algorithm*
  Based on this algorithm, the recorded multichannel signals can be read from any

position of the data file. The input value of this position is the azimuth direction or its interval.

- *RMMSE beamforming algorithm*
  This algorithm was implemented based on the approach suggested in one of the articles included in the literature review and was tested in terms of estimation accuracy for precipitation profiles.
  For the performance study of this algorithm, a simulator was developed, *Weather Radar Signal* simulator. The first part of it, the *Doppler weather spectra and time signals* was implemented based on the approach proposed in 1975 by Zrnic in one of the papers included in the literature review, and the second part, *data model* based on the lessons studied for *Signal Processing and Communication*. This simulator can be used for a large scale of applications that require the knowledge of the "ground truth" of Doppler spectrum moments. Being versatile, this simulator allows any kind of values for input spectra moments, even experimentally obtained values. For this reason, the implementation of this simulator was one of my contributions to this project.
  Regarding the RMMSE algorithm, it shows high performances for the estimation accuracy of the precipitation profiles, based on data recorded with MAX3D radar. This conclusion was drawn based on the performances for sidelobes level suppression and accurate estimation of spectra moments. When the beam-forming sidelobes are well suppressed, the algorithm avoids the creation of processing artifacts in estimated Doppler spectrum like e.g. spectrum bimodality, and provide the possibility to detect the real cases when two different layers of precipitation with different mean Doppler velocities are present at the same resolution volume and form one bimodal Doppler spectrum. To study this performance of beamforming algorithms, the RMMSE algorithm was compared with results for Fourier and Capon methods.
  The application of the RMMSE algorithm to real data raised some implementation difficulties, especially because it requires an apriori knowledge of the noise covariance matrix. The method to obtain this information is not mentioned in the literature and has been developed. For this reason, the implementation of the RMMSE algorithm to real data with much better performances than conventional Fourier or Capon algorithms is an element of my project's novelty and was one of my contributions to this project.

- *Doppler processing*
  This operation implies a fast Fourier transformation (FFT), which is already well known and is mentioned here only for the workflow of the processing chain.

- *The Target Mask algorithm, AMF*
  After beamforming and Doppler processing, the resulting range-Doppler map contains weather targets, noise, and non-weather targets. To keep only weather targets and to filter out the rest of the elements from the spectra enhances the estimation accuracy by ten times for power reflectivity and by the order of tenths times for the mean Doppler velocity and spectral width. For this reason, an iterative and adaptive algorithm was proposed, called Adaptive Morphological Filtering (AMF).

This algorithm utilizes a priori known (measured) profile of noise power for the noise signals clipping and further uses morphological operations, opening, and dilation, for further filtering out the false alarm signals. This algorithm was extensively tested during this project on simulated data, using the simulator developed in this project, and also for real data. The results show that this algorithm provides a high estimation accuracy of the range-Doppler map. This algorithm brings elements of novelty due to the proposed hypothesis testing function used for the iterative algorithm and for the entire framework, where a priori profile of noise power and morphological operations are used. This can be considered a personal contribution to this project, as well.

- *Doppler Aliasing correction algorithm*
  In this project it has been shown that discontinuities due to Doppler aliasing effect, can imply strong limitation concerning estimation accuracy of precipitation profiles. There are simple methods suggested to correct this effect, that rely on the estimation of the position of mean or maximum of Doppler spectra, followed by a circular shift of spectrum until the position of one of these reaches the center of the spectrum. However, under the conditions given by the discontinue spectra, these methods are biased. The one that proposes to use mean is biased because spectra are discontinued, and the second that consider maximum is not the best solution when sometimes there are two weather objects present in the spectra. Our proposed algorithm overcomes this problem by recalculating in an iterative way the mean value and difference between its position and center of spectra, and shift the spectrum to that difference until this difference converges to zero. This process is considered here error minimization, where error the difference that has been defined before.
  However, in Chapter 5 it was shown that this algorithm works for simple cases of aliasing, when one of the sides of the spectrum contains a considerable power spectrum and for weather data recorded with MAX3D, situations much more complex have been found. Nevertheless, this algorithm can be considered a personal contribution as well to this project, even is requires considerable upgrades to cope with the difficult task of aliasing correction. Furthermore, the idea to minimize errors defined above within an iteration algorithm is considered an element of novelty.

- *Data Quality Mask, DQM*
  At this step of the processing chain, it is considered that if there is a weather target in the Doppler spectra, the correspondent Doppler moments are estimated with high accuracy. However, the processed Doppler spectra still can contain artifacts related to the effect of signal saturation, which could not be filtered so far with standard processing steps. Based on constant elevation/height PPI plots for spectral width, we notice that this artifact's spectral width is, in general, wider than $4[m/s]$. Therefore, the DQM algorithm has been proposed that uses this information to eliminate from consideration signals at PPI locations where saturation is present, from each Doppler moment's map. For this, a threshold of $2[m/s]$ is applied, which protect weather targets and filter out non-weather targets and arti-

facts. However, if the Doppler velocity aliasing is not corrected before the Doppler spectral moments estimation, spectral width can exceed $2[m/s]$, and as result, the final precipitation map can include some discontinuities. Finding that the saturation artifacts have a spectral width of around $4[m/s]$ can be considered a novel contribution to this project.

- *Vector components derivation for the first and second Doppler spectral moments*
  This algorithm and the next two ones are part of the *reconstruction of 3D Doppler map* packet of algorithms. This algorithm applies the simple transformation to the first and second Doppler spectral moments, which are related to a specific elevation angle, for their conversion to horizontal and vertical Doppler velocity components. This transformation uses the trigonometric functions and is quite trivial, but the understanding of the meaning of these two velocity components implied an extensive discussion. These vector components are necessary for the next step, for the 3D interpolation of resulting Doppler spectral moments. Because *Main Array* footprint scanning area has a small dimension, vertical wind direction does not change much. Thus we can consider that the horizontal component of the radial mean Doppler velocity provides direct information about the real rate of change and value of horizontal wind velocity, up to a scalar. This scalar is the product between the real terminal velocity of the particles and the sinus of the elevation range. For small elevation angles, the effect of terminal velocity can be neglected. This assumption was used to generate results given in Chapter 6 and to perform a preliminary test for the MAX3D capability to perform estimation of wind direction.

- *Polar to Cartesian transformation - interpolation algorithm*
  This transformation implies a 2D interpolation algorithm between the transformation grid and the original polar grid. The former is a grid in polar coordinates obtained based on the Cartesian coordinates grid where the final targets have to be displayed. Even if interpolation can be applied straightforwardly, the understanding of the locations where to apply it in the processing chain was one of this project's contributions. However, another question that was not addressed in this thesis is the dimension of the transformation grid. In this study, we used a 100 by 100 grid to minimize the computation time. Have been doing the study of 2D interpolation errors carried out for the special case of weather targets, and also the justification of the location of this algorithm in the whole processing chain. The achieved results and optimized processing chain structure can be considered a novel contribution to this project.

- *Constant height PPI and constant azimuth RHI*
  Representation of results after reconstruction of 3D Doppler maps is performed for fixed height range-azimuth (PPI) and fixed azimuth range-height (RHI) plots. The RHI plot can be displayed using a 2D image plot, whereas, for the PPI plot, a visualization/representation algorithm was developed. This algorithm uses *(*mesh) function from Matlab and includes values of the azimuth angles, the values of the range, and a 3D grid plot to show the dimension of each resolution cell and the

exact location of the targets. However, this algorithm posed some challenges because function *mesh*, from Matlab, centers the image only if there are cells filled in each quadrant. This is not all the time the case, and the center of the plot is wrongly computed, and, as result, the image drifts. A solution to overcome this problem has been proposed - to use the interpolation of a few doom values at the edges of the PPI circle. This is considered a novel personal contribution to the project, too.

Therefore, after extensive testing and performance studies, the signal processing toolbox *MAX3D-Weather-PhAA* implements the developed and studied processing algorithms and can provide the 3D range-Doppler map images using data recorded with the MAX3D radar. This toolbox is novel by its premise of finding technical solutions and compromises to show the efficiency and capability of using the MAX3D radar for weather target detection and estimation of horizontal wind direction. In the end, based on the results obtained and the proof of the performance of the algorithms used, we can conclude that this signal processing toolbox it is an big step to the final objective to use MAX3D radar for weather applications.

7.2. RECOMMENDATIONS FOR FUTURE

- For further development of the AMF algorithm it is necessary to be mentioned that it was tested for real data when weather targets were further than the $4[km]$ range. Within the first $4[km]$, the effect of ground clutter is much stronger. In this case, if ground clutter and weather target are present in the same spectra, thus this decreases the estimation accuracy of spectral moments. In this case, it is recommended to test the estimation accuracy in the scenario mentioned above. However, an algorithm that can clean point targets when present in weather spectra, e.g. ground target, birds, is important of high importance to be implemented. In this case, for flying objects, MAX3D has already implemented a tracking system of these targets, thus information of weather targets/flying targets can be merged to increase estimation accuracy of parameters of interest for both classes. For the ground truth, a priori knowledge of the position of the buildings can be used as a solution. Using the developed simulator, *Radar Weather Signal* simulator, a simulation of the ground truth can be obtained, based on known position, and subtracted from the real image of Doppler weather spectra.

- The performance study of the AMF algorithm has been shown that maximum estimation accuracy for each spectral moment requires a different SE dimension for the same rate of false alarm. Therefore, to increase the performances of this algorithm, implementation of this adaptive algorithm using three different criteria based on each spectra moment, and estimation of three different SE dimensions can increase the accuracy. On the other hand, this can also increase computation time in this case.

- AMF algorithm requires a more robust and extensive simulation. For this, it is recommended to use real values of the spectra moments obtained from weather radar. This can be done using a weather simulator developed in this project.

- RMMSE beamforming algorithms performance is dependent on the amplitude and phase errors from the phased antenna array elements. The error that influences the performance the most is phase error. This error can be computed as the variance of the phase differences between each antenna element. In one of the papers included in the literature review [1], the authors showed that if this error is corrected up to a given threshold RMMSE performances are comparable with those for simulated data. Hence, one recommendation is to implement a more efficient calibration algorithm for MAX3D and to try to minimize phase error. This calibration can be done directly on existing data if the final calibration coefficient is computed using much more strong reflective points nearby the radar. The actual calibration coefficients are computed using only one object.

- Implemented algorithm for Doppler Aliasing correction (DAc) can correct only slight effects of velocity aliasing, when one of the sides of spectra contains the most considerable power spectrum. Hence, in Chapter 5, last subsection, is pointed out a case when aliasing situation is too difficult to be solved with DAc. Since this correction is a very critical issue, it is recommended to develop a robust algorithm.

- The signal processing toolbox developed in this thesis was tested only for data recorded at $1[RPM]$, with the Doppler processing burst of 256 pulses. Therefore, it is recommended to record weather data at different rotation velocities in a short interval of time and to compare the performances of *MAX3D-Weather-PhAA* for each 3D Doppler map, estimated at the correspondent rotation velocities.

- Related to the previous recommendations, if it is proved that *MAX3D-Weather-PhAA* works for any rotation velocities, then to be proven which is the smallest possible one, e.g. $18.75[RPM]$ for 16 pulses, that can provide a comparable level of estimation accuracy as in case proved in this project. Hence, a trade-off may be found between the rotation velocity required for bird detection and weather detection, or a time division management strategy can be developed, e.g. every five minutes radar rotates slower, e.g. $1.17[RPM]$, 256 Doppler pulses, to refresh the weather situation.

- At this point, reconstruction of 3D Doppler map was performed based on precipitation profiles derived from radial Doppler velocity. This was used, as a preliminary step, to determine the capability of this radar to perform estimation of wind direction. However, this was performed based on two assumptions. First, that wind field at constant height does not change much, thus wind direction and velocity are constant, and second, vertical wind direction motion is not changing much within the area described by the footprint of MAX3D's *Main Array*. Hence, a recommendation to rest the real capability of this radar to make wind field estimation is to plug the resulted estimated precipitation profiles in the linear wind model and to reconstruct the 3D wind model. Then, to compare these results with another weather radar from The Netherlands, for the same space where their scanning beams are overlapping.

REFERENCES

[1] H. Kikuchi, E. Yoshikawa, and T. Ushio, *Application of Adaptive Digital Beamforming to Osaka University Phased Array Weather Radar,* IEEE Transactions on Geoscience and Remote Sensing **55**, 3875 (2017).

A

COMPENSATION FOR RANGE-DEPENDENT ATTENUATION

Radar equation can be written in most general form as:

$$P_{rx} = \frac{P_t G_t G_r \lambda^2 \sigma_{vol}}{(4\pi)^3 r^4} \tag{A.1}$$

where for the case of of 3D precipitation as radar target

$$\sigma_{vol} = Volume \cdot \eta = Volume \sum_{i}^{N} \sigma_i \tag{A.2}$$

where $\eta[m^{-1}]$ represents the radar cross section of the unit volume, and the radar resolution volume *Volume* defined as

$$Volume = r^2 \Delta\phi \Delta\theta \Delta r \tag{A.3}$$

If we denote the radar constant

$$C^V = \frac{P_t G_t G_r \lambda^2 \Delta\phi \Delta\theta \Delta r}{(4pi)^3} \tag{A.4}$$

which include all constant parameters of the radar system, then we can rewrite the received power as follows

$$P_{rx} = \frac{C^V \eta}{r^2} \tag{A.5}$$

Now if we extrapolate this formula for discrete case of fixed range grid, which is specific for the FMCW radars, each i^{th} sample of the received power will be characterized by

$$P_{rx}^{(i)} = \frac{C^V \eta(i)}{r^2(i)} \tag{A.6}$$

If we assume that the radar system measures, actually, the SNR (or it is possible to convert received signal to the SNR), we can rewrite this equation as follows

$$SNR(i) = \frac{C^V \eta(i)}{N(i) r^2(i)} \tag{A.7}$$

where $N(i)$ represents the average noise power in $i^t h$ range resolution bin, and is equal to some constant value for every specific radar system, defined as

$$N = kT_{sys}BF \tag{A.8}$$

where k - the Boltzman constant, T_{sys} represent the system temperature in K, F is receiver noise factor, B is the receiver bandwidth, which for an FMCW radar equals to the PRF/SRF. If we apply the general assumptions, then is $T_{sys} = 290K$, B can be considered 1kHz in this case, and finally receiver noise figure, $F = 4dB$. Finally noise power in dB is $N = -169.98dB$. Finally we can find out reflectivity, $\eta(i)$

$$\eta(i) = \frac{SNR(i) r^2(i) N}{C^V} \tag{A.9}$$

In this case, C^V could be computed as follows

$$C^V[dB] = P_r + G_t + G_r + 10log_{10}(\frac{\lambda^2 \sigma_{vol}}{(4\pi)^3}) \tag{A.10}$$

$$C^V[dB] = 13 + 36.5 + 39.0 - 53.03 = 35.46 \tag{A.11}$$

Finally, reflectivity $\eta[dB]$ is

$$\eta(i)[dB] = SNR(i) + 20log_{10}(r(i)) + N - C^V, \tag{A.12}$$

$$\eta(i)[dB] = SNR(i) + 20log_{10}(r(i)) - 205.44. \tag{A.13}$$

Let us consider $r = 15km$ only to understand the weight of range in this equation.

$$\eta(i)[dB] = SNR(i) + 83.52 - 205.44 = SNR(i) - 121.92 \tag{A.14}$$

Due to the exponential increasing characteristic of range contribution to the function $\eta(i)$, we will consider a reference range, r_0, and then instead of $r(i)$ we will have an attenuation factor $\frac{r(i)}{r_0}$. In this way, equation stated above becomes

$$\eta(i)[dB] = SNR(i) + 20log_{10}(r(i)) - 20log_{10}(r_0) - 205.44 \tag{A.15}$$

This reference range can be minimum 1, which means that will not be accounted anymore, or maximum the maximum range value, which will vanishes the effect of compensation at all.